Alma Mater Studiorum · Università di Bologna

Scuola di Scienze
Dipartimento di Fisica e Astronomia
Corso di Laurea Magistrale in Fisica

Performance of the $H \to ZZ^* \to 4\mu$ analysis with the CMS Phase-2 muon detector upgrade

Relatore:
Prof.ssa Sylvie Braibant

Correlatore:
Dott. Simranjit Singh Chhibra

Presentata da:
Elisa Fontanesi

Anno Accademico 2017/2018

Sommario

Le prestazioni dell'analisi del canale di decadimento del bosone di Higgs del Modello Standard $H(125\text{ GeV}) \to ZZ^* \to 4\mu$ sono state studiate con il rivelatore CMS inclusivo degli interventi previsti per l'upgrade del sistema di muoni, necessario per la fase di presa dati ad alta luminosità (fino a 7.5×10^{34} cm^{-2}s^{-1}) al Large Hadron Collider (HL-LHC). L'upgrade di Fase-2 del rivelatore di muoni di CMS, che avrà luogo dal 2024 al 2026, è cruciale per poter sfruttare in modo efficiente i dati raccolti durante HL-LHC a fronte di ardue condizioni sperimentali, quali, per esempio, un numero maggiore di collisioni sovrapposte per ogni evento, fino a 200 (noto come pile-up).
Il canale di decadimento $H \to ZZ^* \to 4\mu$ fa affidamento essenzialmente sul sistema di muoni per rivelare i quattro muoni dello stato finale; per questo rappresenta un importante processo per studiare le modifiche proposte per l'upgrade del rivelatore di muoni, in particolare l'estensione in pseudorapidità da $|\eta| < 2.4$ a $|\eta| < 2.8$ dovuta all'introduzione del sottorivelatore ME0 (*Muon Endcap 0*).
I risultati presentati in questo lavoro sono ottenuti a partire da simulazioni di eventi di collisione protone-protone a $\sqrt{s} = 14$ TeV con la simulazione completa del rivelatore CMS nella configurazione successiva all'upgrade. Gli eventi di segnale e di fondo sono stati simulati con un pile-up medio di 200. L'analisi è effettuata assumendo una luminosità integrata di 3000 fb^{-1} (attesa in circa dieci anni dall'inizio di HL-LHC) e segue l'analisi utilizzata per i dati del 2016 (Run-2). Si è trovato che l'efficienza di selezione del segnale non subisce un peggioramento in presenza di un elevato pile-up ed aumenta del 17% con l'estensione dell'accettanza del sistema di muoni.

Abstract

A study of the performance of the Standard Model $H(125\ \text{GeV}) \rightarrow ZZ^* \rightarrow 4\mu$ analysis with the upgraded CMS muon detector for the high luminosity operation (up to $7.5 \times 10^{34}\ \text{cm}^{-2}\text{s}^{-1}$) at the Large Hadron Collider (HL-LHC) has been carried out. The CMS Phase-2 muon detector upgrade, which will take place from 2024 to 2026, is crucial to efficiently exploit the data that will be collected at the HL-LHC, under very challenging experimental conditions, such as large number of overlapping collisions per event, up to 200 (referred to as pile-up).

The $H \rightarrow ZZ^* \rightarrow 4\mu$ analysis essentially relies on the muon system to detect four muons in the final state; it therefore represents an important benchmark for the proposed muon detector upgrade, in particular the extension in pseudorapidity of the muon detector from $|\eta| < 2.4$ to $|\eta| < 2.8$ by introducing the ME0 (*Muon Endcap 0*) subdetector.

The results presented here are obtained using simulated proton-proton collision events at $\sqrt{s} = 14$ TeV with the full simulation of the upgraded CMS detector. The signal and background events are simulated with an average pile-up of 200. The analysis is performed assuming an integrated luminosity of 3000 fb^{-1} (expected in almost ten years of the HL-LHC operation) and follows the analysis of the 2016 data (Run-2). It is found that the signal selection efficiency remains immune to the high pile-up conditions and increases by 17% with the acceptance extension of the muon system.

Gratuitamente avete ricevuto,
gratuitamente date.

(San Matteo, 10:8)

Alla mia famiglia e a ciascuno di voi, amici cari e santi,
per avere scolpito questo mio piccolo cuore
a forma di una grande casa.

Acknowledgments

At the end - and at the beginning - of this experience, I wanted to show how grateful I am for the possibility I had to work with the CMS Bologna group.
In particular, I must thank prof. Sylvie Braibant, for her support and her kindness; Simranjit, for the incredible number of things he taught me and for his cheerfulness; Lisa, for her constant care towards me and for her great passion and curiosity for physics. I would also like to thank Paolo Giacomelli, Nicola De Filippis - from the University of Bari -, Luigi Guiducci, Francesca Romana Cavallo and Giovanni Abbiendi for the help - great or little, as well - they all offered me.
I would like to deeply thank Paolo Capiluppi, since he has indirectly encouraged me to invest my energies and studies in physics; moreover, I want to thank my special physics laboratory friends Maria Giovanna and Arianna, who shared together with me the path of these demanding but, at the same time, joyful years of study.

Contents

List of Figures

List of Tables

Introduction

The Higgs boson represents the last particle of the Standard Model (SM): in fact, according to the prediction of the SM, it was the final missing piece predicted to be verified experimentally. Soon after announcing the Higgs discovery (2012) at the Large Hadron Collider (LHC), both the ATLAS and CMS experiments begun to study its properties "*to understand this fascinating particle in more detail and study its behaviour*" (CMS spokeperson Tiziano Camporesi).
Today the SM, which seems to be only a little part of a more complex picture, can be used to make even more specific predictions about the unsolved questions of the particle physics. Thanks to the LHC's sensitivity to rare events and effects that could give indications of new physics beyond the SM, information from the CERN experiments will help to zoom into the subatomic world.

The CMS experiment at present is planning a substantial upgrade of all the subdetectors in view of the last phase of LHC operation, characterized by a very high luminosity, so-called HL-LHC. It aims to increase its luminosity by a factor 10 beyond the LHC's design value in order to make more probable potential discoveries after 2026.
For this reason, efficient ways to perform reliable detector performance studies must be found. My research is focused on estimate in a realistic way the sensitivity for the $H \rightarrow ZZ^* \rightarrow 4\mu$ analysis at 14 TeV: during my work for the master thesis I have performed a study of this channel extrapolated to the HL-LHC conditions and the Phase-2 CMS detector.

The first question could be: why muons? They represent a unique signature of most of the physics which LHC aims at exploring. Muons interact only weakly with matter, so they are the only particles able to cross the whole detector, allowing a very high detection efficiency. Moreover, they are often indicators of "interesting" physics: in fact, they are produced via electroweak interaction, so that a W, Z or Higgs boson is probably involved or, hopefully, some new, unknown particles. Finally, a four-muons final state can be completely reconstructed.
The second ingredient of this analysis is the CMS experiment: it is designed to trigger on and reconstruct muons at very high luminosities in an efficient way, as suggested by the name, *Compact Muon Solenoid*. The ability to study muons is ensured by the simplicity of the detector design, which provides a solenoidal magnetic field responsible for precise tracking measurements and for triggering on muons

through their bending in the transverse plane. In this thesis the main interest is to study the impact on the analysis due to new capabilities of the upgraded muon detector, in order to see whether CMS would cope with the high luminosities typical of the HL-LHC (of the order of 5×10^{34} cm^{-2}s^{-1}). The focus is on the detector performance with the insertion (currently under discussion) of a new gaseus subdetector in the forward region at small angles, *Muon Endcap 0* (ME0), aiming to demonstrate the advantages related to an increase in the detector's angular coverage.
In order to do that, the implementation and optimization of the latest tuning of muon identification (ID) and new muon reconstruction algorithms represent the first step, fundamental to provide high efficiency in selecting the signal together with good background mitigation. An increase of the LHC luminosity implies a larger number of overlapping events (up to 200), referred to as *pile-up* (PU), which makes the muons non isolated. Therefore, it is crucial to perform a careful study investigating an algorithm able to work efficiently in the endcap region and, at the same time, proper selection criteria to optimize the analysis in presence of very high pile-up contamination.

To perform these studies I have used Monte Carlo (MC) simulations of the signal and the backgrounds, comparing step by step two different scenarios: without pile-up and with 200 pile-up events (expected for the HL-LHC). These activities are fundamental in the interest of the CMS Muon Technical Design Report (TDR) submitted recently, aiming to motivate the CMS muon detector upgrade.

In chapter 1, I will present the SM from the perspective of the gauge theories and the Higgs boson physics, starting from the theory of the spontaneous symmetry breaking and the Brout-Englert-Higgs mechanism until the discovery of the particle in 2012. I will also give a complete review of the process under investigation in this thesis. Then I will describe the LHC and the CMS experiment in chapter 2, focusing on the goals and projects for the HL-LHC and the CMS detector upgrade.
In the second part of the thesis I will explain how my activities have been developed. Chapter 3 describes the MC samples used for the analysis, explaining the complete simulation of the events and the reconstruction of the physics objects with the CMS software, with a particular interest on muon identification and isolation. Finally the studies on the muon ID and the investigations on the isolation are presented in chapter 4, showing a comparison between the signal and the main background processes at the end of the selection for PU 0 and PU 200 scenarios. The final results of the performance of analysis with the upgraded CMS muon detector are then presented.

Chapter 1

Standard Model and the Higgs boson physics

1.1 The Standard Model and the gauge theories

The formation of the Standard Model (SM) results from a long sequence of experimentations and brilliant ideas developed both in the theoretical and experimental particle physics. In the late 1960s all the known elementary constituents of matter, the particles, and the fundamental forces (except for gravity) through which they interact were included in the SM, which could be considered as "a theory of everything". Science's path is often seen as a quest for unification in our understanding of the physical universe, attempting to provide a theoretical representation of all the experimental phenomena. The basic formal and conceptual framework of the SM is Quantum Field Theory (QFT), which is a coherent summary of quantum mechanics and special relativity. According to this mathematical model, fields associated to particles are the most fundamental entities. Indeed we interpret particles as a fluctuation in the associated field and the interactions between them as an exchange of mediator virtual particle. The following section describes the fundamental particles of the SM and introduces the concept of gauge invariance [1, 2, 3, 4, 5] in order to explain how a local gauge invariance is intimately connected to the interacting field theories and the fundamental interactions, as a consequence.

1.1.1 Introduction to the fundamental particles

We define "fundamental particle" as a point-like physical system which is a structureless unit of matter, in the sense that its substructure is impossible to be explored.
In the current view of the SM theory, the whole universe is made out of twelve fundamental particles and their corresponding antiparticles (which the same spin, mass and mean lifetime and opposite charge and magnetic momentum as of par-

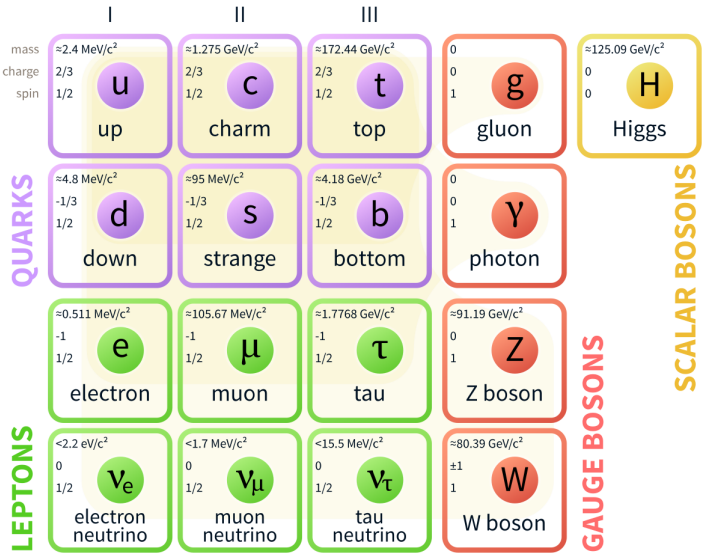

Figure 1.1: Fundamental particles of the Standard Model.

ticles). In addition, the frame of fundamental particles includes the mediators of interactions. A complete schematic description of all the particles encapsulated in the SM is shown in Figure 1.1.

"*We will not be able to give a final answer to the question of which particles are elementary until we have a final theory of force and matter.*" (S. Weinberg, 1996)

The organization of all the fundamental particles inside the SM reflects two remarkable ideas suggested during the 1950s and 1960s and developed later: the Yang-Mills theories (1954), which introduced the gauge symmetry idea, and the quark model proposed in 1964 independently by M. Gell-Mann and G. Zweig.
The fundamental particles, so-called *fermions*, have half-integer spin (s = $\frac{1}{2}$) and obey the Pauli exclusion principle; they are described by the Fermi-Dirac statistics and are classified into six leptons and six quarks. Leptons are divided into three families (given as 1.1) according to their weak interaction properties (three weak-isospin doublets). They include electron (e), muon (μ) and tau (τ), with increasing mass values, and their associated neutrinos (ν_e, ν_μ, ν_τ): the first carry a single unit of negative electric charge and interact in a weak or electromagnetic way; the second are electrically neutral and are sensitive only to the weak interaction.

$$\begin{pmatrix} e \\ \nu_e \end{pmatrix} \quad \begin{pmatrix} \mu \\ \nu_\mu \end{pmatrix} \quad \begin{pmatrix} \tau \\ \nu_\tau \end{pmatrix} \tag{1.1}$$

A lepton quantum number (L) is associated to leptons, which is additive and assumes values 1 and -1 for particles and antiparticles, respectively. Analogously a baryon quantum number (B) describes quarks, with a value equal to $\frac{1}{3}$ for quarks

and -$\frac{1}{3}$ for antiquarks. Quarks occur in six different flavours: up (u), charm (c) e top (t) carrying positive charge of $\frac{2}{3}$ units and down (d), strange (s), bottom (b) carrying a negative charge of $\frac{1}{3}$ units. They also fall into three generations (three isospin doublets):

$$\begin{pmatrix} u \\ d \end{pmatrix} \quad \begin{pmatrix} c \\ s \end{pmatrix} \quad \begin{pmatrix} t \\ b \end{pmatrix} \tag{1.2}$$

Each quark comes in three colours (red, green and blue), which represent three different states of charge for the strong interaction, named *colour force*. Contrary to leptons, quarks do not exist in free state because the colour force does not drop off with distance: they are always confined to hadrons, which are colourless combinations corresponding to bound states of quarks. Three quarks (or antiquarks) make up the baryons (or antibaryons), which have half-integer spin, while a quark-antiquark pair forms a meson, which has integer spin.
All these objects are considered as fundamental particles, but most of them are unstable: only electron, neutrinos, photon and, in same way, quarks of the first generation (constituents of ordinary matter) are stable particles. According to QFT, interactions between particles are described as an exchange of a quantum of the associated field, so-called *boson*. Bosons, responsible for interactions, have integer spin (s = 1) and follow the Bose-Einstein statistics.

If a theory involves more than one state for particles at a time, the associated fields need different states as well. Based on the gauge theories, to N states for particles there correspond (N^2–1) gauge fields: (N^2–N) charged fields and (N – 1) neutral fields (neutral means that under a specific transformation the multiplet represents the same physical state). Electromagnetism has a single internal charge, the electric charge: the carrier of this interaction is photon (γ), which is neutral because of the conservation of electric charge.
The strong interactions are characterized by three different states related to the colour charge and are mediated by eight gluons (g): they interact with each other because they carry a colour charge as well. The mediators for weak forces are three vector bosons, because weak interactions are described by two different states related to the isospin charge: $W^{\pm}$ (charged vector bosons) and Z^0 (neutral vector boson). As mentioned before, SM is not able to give a description of the gravitational force but luckily this is not a problem for particle physics: the effect of gravity is totally negligible at the scale of particles. The corresponding force-carrying particle of gravity is supposed to be so-called "graviton" (G). The photons and gluons are massless, while $W^{\pm}$ and Z^0 are massive particles. However, quantum of gauge fields propagate at the speed of light so, theoretically, they can not have mass. Therefore, it is necessary to introduce an external mechanism able to give mass to mediators: the theoretical solution was proposed in 1964 by P. Higgs, F. Englert and R. Brout [10, 11] and by G. Guralnik, C. R. Hagen and T. W. B. Kibble [12, 13]. This mechanism predicts the existence of a new scalar boson with spin zero in the SM, the Higgs boson (H). This mechanism is described in details in the next section.

1.1.2 Two basic concepts: symmetry and invariance

Our best understanding and description of the fundamental structure of matter is deeply related to symmetry principles.

"*Symmetry, as wide or as narrow as you may define its meaning, is one idea by which man through the ages has tried to comprehend and create order, beauty, and perfection.*"
(H. Weyl, 1952)

Symmetry is a concept familiar to human mind, commonly related to the idea of order, harmony and beauty. It has connected to the mathematical concept of "operation" over time: particularly, symmetry is a mathematical or physical feature of a system, which alludes to an invariant system some transformations.
The symmetries and corresponding transformations could be classified as continuous or discrete, geometrical or internal and global or local. Invariance principles play an essential role in particle physics, because they guide the construction of SM theories. Moreover, conservation laws and selection rules in Nature depend on Lagrangian symmetries. The theory behind is the Noether's theorem, which connects exact symmetries and conservation laws: continuous symmetries of the Lagrangian lead to exact conservation laws. To every continuous symmetry of the Lagrangian there corresponds a conserved quantity.

In the next section, we will underline the connection between Lagrangian symmetries and gauge field theories: the requirement of *local gauge invariance*, in fact, implies the existence of interactions and gives rise to interaction field theories.

1.1.3 Gauge invariance

The global gauge invariances are common in particle physics: a global symmetry does not depend on space-time. A global gauge invariance can be generalized to a local one, as suggested by C. N. Yang and R. Mills, by choosing the phase arbitrarily in the whole space-time: the transformation varies from place to place in space-time.

"*We wish to explore the possibility of requiring all interactions to be invariant under independent rotations of the isotopic spin at all space-time points.*"
(C. N. Yang and R. Mills, 1954)

A gauge symmetry identifies a class of physical theories based on the requirement of the invariance under a group of transformations in an abstract space, named gauge transformations.
Local gauge symmetry is a local transformation of fields,

$$\psi(x) \rightarrow e^{i\Lambda(x)}\psi(x), \tag{1.3}$$

which leaves the Lagrangian invariant.
In order to not violating the gauge invariance under the passage from a global

symmetry to a local one, we have to introduce a gauge field which couples to matter fields: the requirement of this gauge field explains the nature of interactions. This inner relation between local gauge invariance and the form of interactions accounts for a possible unification of fundamental interactions.

1.1.4 Fundamental interactions

The SM theory is based on a gauge principle of local phase invariance: the mathematical description of symmetries uses the group theory. SM contains the known interactions and is based on a combination of three different symmetry groups,

$$\mathrm{SU(3)_C} \otimes \mathrm{SU(2)_L} \otimes \mathrm{U(1)_Y},$$

where single elements of the product are respectively:

- the three-dimensional group $\mathrm{SU(3)_C}$, which governs the strong interactions of quarks, binding them into hadrons and providing stability to the nucleus overcoming electric repulsion. The generator of strong interaction is colour, thus three degrees of freedom are involved;
- the group $\mathrm{SU(2)_L}$ of isotopic spin conservation, representing a local symmetry which governs the weak interactions of quarks and leptons;
- the one-dimensional group $\mathrm{U(1)_Y}$ of electrodynamics.

The electrodynamics is described by an *abelian* group, since the phase factors commute with each other. On the other hand, weak and strong interactions involve different states, therefore the phase factors become matrices, which generally do not commute with each other: the associated symmetry is called a *non-abelian* symmetry.
A clear analogy between electromagnetic and weak interactions was explained in 1961 by S. Glashow who proposed a structure based on a group symmetry SU(2) $\otimes$ U(1). It is particularly convenient to choose I_3, the third component of weak isospin in the flavour analogy, as the designated generator; it applies only to left-handed (L) fermions[1]. The abelian U(1) group is associated with another generator, the hypercharge (Y), defined by the Gell-Mann and Nishijima relation:

$$Q = I_3 + \frac{1}{2}Y. \tag{1.4}$$

[1]Please note that both left-handed and lepton number are represented by L. In this theory of the SM the L stands for left-handed only.

1.2 From the Spontaneous Simmetry Breaking to the Higgs boson

The gauge principles applied to Yang-Mills theories lead inevitably to a model of interactions mediated by massless bosons and it was supposed that any massless gauge bosons would surely have been detected. However, according to a theoretical approach, experimentalists foresaw the existence of massive vector bosons, carriers of the weak interaction. Consequently, from the beginning the main obstacle to the application of the Yang–Mills approach to the weak interaction theory was the problem of mass. Moreover, gauge theories were compatible only with exact symmetries, but the physical world manifests a large fraction of symmetry principles which holds only approximately. The next section presents these unsolved questions.

1.2.1 Gauge invariance in the electroweak theory

Let us examine in detail implications of local gauge invariance for the electroweak theory.
The Dirac equation for a free fermion can be given as

$$(i\gamma^{\mu}\partial_{mu} - m)\psi(x) = 0, \tag{1.5}$$

driven from the Lagrangian density:

$$\mathcal{L} = \bar{\psi}(x)(i\gamma^{\mu}\partial\mu - m)\psi(x). \tag{1.6}$$

Requiring local gauge invariance under a $\mathrm{SU(2)_L} \otimes \mathrm{U(1)_Y}$ transformation, we need to introduce four gauge fields $(W^1_{\mu}, W^2_{\mu}, W^3_{\mu}, B_{\mu})$ and to replace the derivative ∂_{μ} with the covariant derivative:

$$D_{\mu} = \partial_{\mu} + \frac{ig'}{2}B_{\mu}Y + \frac{ig}{2}\vec{\tau}\vec{W}_{\mu}, \tag{1.7}$$

where g is the coupling of the weak-isospin group $\mathrm{SU(2)_L}$, $\frac{g'}{2}$ is the coupling constant for the weak-hypercharge group $\mathrm{U(1)_Y}$ and

$$W^l_{\mu\nu} = \partial_{\nu}W^l_{\mu} - \partial_{\mu}W^l_{\nu} + g\varepsilon_{jkl}W^j_{\mu}W^k_{\mu}, \tag{1.8}$$

$$B_{\mu\nu} = \partial_{\nu}B_{\mu} - \partial_{\mu}B_{\nu}. \tag{1.9}$$

The index l related to fields W^l and the extra-term with Ricci tensor ϵ_{jkl} underline that generators do not commutate with each other because of the non-abelian nature of the symmetry group $\mathrm{SU(2)_L}$.

The Lagrangian for the electroweak theory can be written as

$$\mathcal{L} = \mathcal{L}_{gauge} + \mathcal{L}_{leptons}, \tag{1.10}$$

where the kinetic term for the gauge fields is

$$\mathcal{L}_{gauge} = -\frac{1}{4}W^l_{\mu\nu}W^{\mu\nu l} - \frac{1}{4}B_{\mu\nu}B^{\mu\nu} \tag{1.11}$$

and the matter term is

$$\mathcal{L}_{leptons} = \bar{R}i\gamma^\mu(\partial_\mu + \frac{ig'}{2}B_\mu Y)R + \bar{L}i\gamma^\mu(\partial_\mu + \frac{ig'}{2}B_\mu Y + \frac{ig}{2}\vec{\tau}\vec{W}_\mu)L. \tag{1.12}$$

It describes the interaction between matter particles mediated by the exchange of massless gauge bosons: in fact, it does not contain quadratic terms for gauge fields. Trying to insert "by hand" a mass term, the Lagrangian invariance would be destroyed.

In the early 1960's, physicists were thinking about two logically coherent solutions: either there would exist a dynamical mechanism to give a non-null mass to gauge fields, or they would be effectively massless and have not been observed yet.

1.2.2 Spontaneous symmetry breaking

A turning point of the problem was the idea of spontaneously broken symmetry: there might be symmetries of the Lagrangian that are not symmetries of the vacuum, known as ground states. One of the main themes in modern physics is the study of how symmetries of the Lagrangian can be broken [4, 5, 6, 7, 8].

"*While we would like to believe that the fundamental laws of Nature are symmetric, a completely symmetric world would be rather dull, and as a matter of fact, the real world is not perfectly symmetric.*" (A. Zee, 2010)

In Nature it could happen that some physical laws are characterized by hidden symmetries because the ground state is not invariant under corresponding transformations. Thus, the Lagrangian density is invariant under a certain symmetry ($\partial\mathcal{L} = 0$); however, the physical vacuum is not unique and, consequently, not invariant under the symmetry transformations. This situation is usually named as *spontaneous symmetry breaking* (SSB).

This reasoning has to be applied to QFT. For a generic scalar field the Lagrangian is

$$\mathcal{L} = \frac{1}{2}(\partial_0\phi)^2 - \frac{1}{2}(\partial_i\phi)^2 - U(\phi); \tag{1.13}$$

we look for minima of the potential energy, specifically for the minimum of the potential $U(\phi)$, because spatial variation in ϕ only modifies the energy. The value assumed by ϕ in the vacuum is known as the *vacuum expectation value* (VEV) of ϕ and is denoted as $< \phi >$.

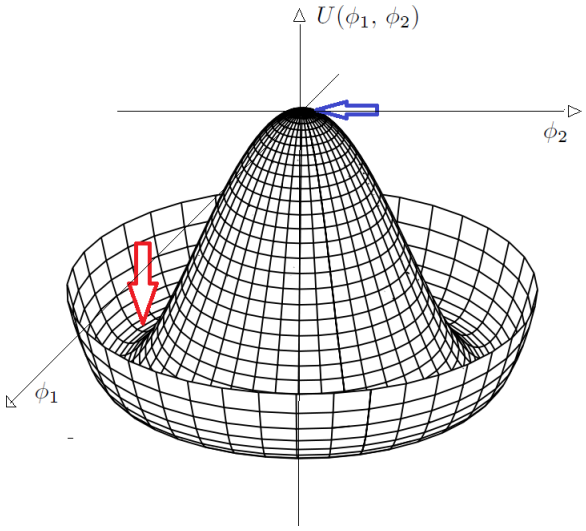

Figure 1.2: A "mexican-hat" potential typical of a two-scalar fields theory.

Before looking at the real case of SSB related to the $\mathrm{SU(2)_L} \otimes \mathrm{U(1)_Y}$ gauge group, we consider how SSB may arise in a simple mathematical model. The essentials for a theoretical understanding of the phenomenon are contained in a simpler global case, which we consider in the paragraph below.
Let us consider a real scalar field, whose potential may be written in the form:

$$U(\phi) = -\frac{1}{2}\mu^2\vec{\phi}^2 + \frac{\lambda}{4}(\vec{\phi}^2)^2. \tag{1.14}$$

In a one-dimensional space, it is possible to see clearly that two cases could be distinguished depending on the sign of μ^2:

- if the parameter $\mu^2 > 0$, the potential has an unique minimum at $\phi = 0$, coincident with the vacuum state, and the symmetry is manifest;
- else if the parameter $\mu^2 < 0$, the potential minima are located in two degenerate lowest-energy states, either of which may be chosen to be the vacuum: this is a spontaneously broken symmetry.

We are interested in the second case.

In a two-dimensional space, corresponding to a continuous symmetry, the potential has the so-called "mexican-hat" form (given in Figure 1.2), with minima at $\vec{\phi}^2 = \frac{\mu^2}{\lambda}$.
The dynamics determined by $\mathcal{L}$ implies a degenerate set of vacuum states that are non-invariant under the symmetry: the continuum of infinite vacuum states may be distinguished only by the direction of $\vec{\phi}$ in a specific vacuum. We choose a particular direction of $\vec{\phi}$ to have

$$\phi_1 = +v = +\sqrt{\mu^2/\lambda}, \tag{1.15}$$

$$\phi_2 = 0. \tag{1.16}$$

Consequently, we choose

$$\phi_1 = v + \phi_1', \tag{1.17}$$

$$\phi_2 = \phi_2'; \tag{1.18}$$

considering fluctuations around this field configuration and expanding $\mathcal{L}$, we obtain:

$$\mathcal{L} = \frac{\mu^4}{4\lambda} + \frac{1}{2}[(\partial\phi_1)^2 + (\partial\phi_2)^2] - \mu^2\phi_1^2 + O(\phi^3). \tag{1.19}$$

Let us note a remarkable feature here: the quadratic term ϕ_1^2 reveals that the field ϕ_1 has assumed a mass equal to $\sqrt{2}\mu$, while the term ϕ_2^2 is absent. This is a field without mass. This emergence of a massless field after SSB is a general and exact phenomenon explained by the Goldstone's theorem.

1.2.3 Goldstone's theorem

The SSB does not cause any problem if applied to a discrete symmetry. However, for global gauge invariance related to a continuous symmetry, SSB gives rise to massless scalar Nambu–Goldstone bosons: for every spontaneously broken symmetry there must be a massless and spinless particle.
According to this theorem, if there exists a conserved operator Q_i which causes a transformation on the component A_j of a field,

$$[Q_i, A_j(x)] = \sum_k t_{ijk}\, A_k(x), \tag{1.20}$$

where t_{ijk} is the representative matrix of the transformation, and if it is possible to break the symmetry so that $\sum_k t_{ijk} \times < 0|A_k|0 > \neq 0$, therefore $A_j(x)$ has a massless particle in his spectrum [12].

The Nambu-Goldstone bosons result from the break-down of a global symmetry, which is generalized to a local one in the Yang-Mills theory: because of the gauge invariance the problem seems to be more difficult.
At this point, the scenario involved zero-mass excitations as a product of SSB, which would be Nambu–Goldstone boson, on one hand and massless vector fields generated passing from a global symmetry to a local one on the other hand: they were called respectively Nambu-Goldstone fields (NG) and Yang-Mills fields (YM). Nevertheless, a special interplay between these two types of fields was supposed to be possible, endowing the gauge particles with mass and removing the Nambu–Goldstone bosons from the spectrum.

The Brout-Englert-Higgs (BEH) mechanism, which gives rise to this mutual coupling, is an elegant solution to all the problems that have emerged up until now and is a central ingredient in our current understanding of electroweak interaction.

"*It is of interest to inquire whether gauge vector mesons acquire mass through interaction.*" (F. Englert e R. Brout, 1964)

1.2.4 BEH mechanism: $\mathbf{SU(2)_L \otimes U(1)_Y}$

The theories presented by Brout, F. Englert and P. W. Higgs and by G. S. Guralnik, C. H. Hagen and W. B. Kibble in 1964 showed how gauge vector bosons could acquire mass through interaction without violating the Lagrangian invariance if the vacuum was degenerate [5, 12, 10, 11, 14].

"*Comforted by these facts, we decided to confront, in relativistic field theory, the long range forces of Yang-Mills gauge fields with the Nambu-Goldstone bosons of a broken symmetry.*" (G. S. Guralnik, C. R. Hagen and T. W. B. Kibble, 1964)

To illustrate this phenomenon, let us look at a Lagrangian density $\mathcal{L}(\phi, \partial_\mu\phi)$ similar to 1.13, substituting ∂_μ with the covariant derivative $D_\mu\phi = (\partial_\mu - ieA_\mu)\phi$ and combining two real fields ϕ_1 and ϕ_2 in a single complex field:

$$\phi = \phi_1 + i\phi_2, \tag{1.21}$$

$$\phi^*\phi = \phi_1^2 + \phi_2^2, \tag{1.22}$$

so that

$$\mathcal{L} = -\frac{1}{4}F_{\mu\nu}F^{\mu\nu} + (D\phi)^*(D\phi) + \mu\phi^*\phi - \lambda(\phi^*\phi)^2. \tag{1.23}$$

Using polar coordinates, one has $\phi = \rho e^{i\theta}$ and $D_\mu\phi = [\partial_\mu\rho + i\rho(\partial_\mu\theta - ieA_\mu)]e^{i\theta}$ yielding to,

$$\mathcal{L} = -\frac{1}{4}F_{\mu\nu}F^{\mu\nu} + \rho^2(\partial_\mu\theta - eA_\mu)^2 + (\partial\rho)^2 + \mu^2\rho^2 - \lambda\rho^4. \tag{1.24}$$

Under a gauge transformation,

$$\phi \to e^{i\alpha}\phi, \qquad \theta \to \theta + \alpha, \qquad A_\mu \to A_\mu + \frac{1}{e}\partial_\mu\alpha, \tag{1.25}$$

the combination $B_\mu = A_\mu - \frac{1}{e}\,\partial_\mu\theta$ is gauge invariant.

Let us see the effect of SSB: the Lagrangian, writing $\rho = \frac{1}{\sqrt{2}}(v+\chi),\ v = \sqrt{\frac{\mu^2}{\lambda}}$, takes the form:

$$\mathcal{L} = -\frac{1}{4}F_{\mu\nu}F^{\mu\nu} + \frac{1}{2}M^2B_\mu^2 + e^2v\chi B_\mu^2 + \frac{1}{2}e^2\chi^2B_\mu^2 + \frac{1}{2}(\partial\chi)^2 - \mu^2\chi^2 - \sqrt{\lambda}\mu\chi^3 - \frac{\lambda}{4}\chi^4 + \frac{\mu^4}{4\lambda}. \tag{1.26}$$

We recognize a vector field B_μ with mass $M = ev$ which interacts with a scalar field χ with mass equal to $\sqrt{2}\mu$. The phase $\theta(x)$, which would have originated a Nambu-Goldstone boson, has disappeared: it has been "eaten" by the gauge field A_μ. Consequently, A_μ has acquired mass.
It is known that a massive vector boson has got three degrees of freedom (corresponding to three states of spin), while a massless vector boson has got only two degrees of freedom (two states of photon's helicity). Because of BEH mechanism, two degrees of freedom of massless gauge field and a single degree of freedom of NG boson combine themselves producing a longitudinal degree of freedom of the massive gauge field B_μ, which becomes massive.

Let us now extend this approach to the group of symmetry $\mathrm{SU(2)_L} \otimes \mathrm{U(1)_Y}$. In 1967-1968, S. Weinberg and A. Salam presented the electroweak unification theory, including SSB and the BEH mechanism in a non-abelian gauge theory. The way to spontaneously break gauge symmetry represented a challenging question in particle physics. The answer suggested by the SM is the existence of a scalar field whose interactions select a vacuum state in which electroweak symmetry is hidden. With the Lagrangian of the electroweak interaction given in 1.10 and the addition of a proper scalar term with the following form,

$$\mathcal{L}_{scalar} = (D_\mu \phi)^\dagger (D_\mu \phi) - U(\phi) \tag{1.27}$$

with

$$U(\phi) = -\mu^2 \phi^\dagger \phi + \lambda^2 (\phi^\dagger \phi)^2, \tag{1.28}$$

the Lagrangian becomes:

$$\mathcal{L} = \mathcal{L}_{gauge} + \mathcal{L}_{leptons} + \mathcal{L}_{scalar}. \tag{1.29}$$

D_μ represents the covariant derivative 1.7 for the isospin doublet ϕ, which indicates a complex doublet of scalar fields:

$$\phi = \begin{pmatrix} \phi^+ \\ \phi^0 \end{pmatrix} \tag{1.30}$$

$$\phi^+ = \frac{\phi_1 + i\phi_2}{\sqrt{2}} \qquad \phi^0 = \frac{\phi_3 + i\phi_4}{\sqrt{2}}. \tag{1.31}$$

ϕ^+ denotes charged fields while ϕ^0 indicates neutral fields. Selecting as the physical vacuum state the configuration $\phi \to \frac{1}{\sqrt{2}} \begin{pmatrix} 0 \\ v \end{pmatrix}$, all four electroweak generators (τ^i and y) are broken. However, their linear combination, corresponding to the operator Q, is unchanged. This fact implies that the vacuum state is not invariant for symmetry groups $\mathrm{SU(2)_L}$ and $\mathrm{U(1)_Y}$, but invariance is conserved in the case of $\mathrm{U(1)_{EM}}$: thus, three mediators of weak interaction acquire mass but the photon remains massless.

At this point, since ϕ is a doublet of $\mathrm{SU(2)_L}$, let us expand the theory around the potential minimum in this way:

$$\phi(x) = e^{i\vec{\tau}\cdot\vec{\theta}(x)/v} \begin{pmatrix} 0 \\ \frac{v+h(x)}{\sqrt{2}} \end{pmatrix}, \tag{1.32}$$

where $\vec{\tau}$ are SU(2) generators, $\vec{\theta}(x)$ represents an arbitrary phase and $h(x)$ a scalar field; redefining the quantities W^1_μ and W^2_μ as

$$W^\pm = \frac{W^1_\mu \mp i W^2_\mu}{\sqrt{2}}, \tag{1.33}$$

in the Lagrangian an additional term appears of the form:

$$...\frac{g^2 v^2}{4} W^+_\mu W^{-\mu} + \frac{v^2}{8}(g W^3_\mu - g' B_\mu)^2 ... \ . \tag{1.34}$$

The linear combination $(gW^3_\mu - g'B_\mu)$ becomes massive, while the orthogonal one remains massless and represents the photon. Hence,

$$Z_\mu = \frac{gW^3_\mu - g'B_\mu}{\sqrt{g^2+g'^2}} = W^3_\mu \cos\theta_W - B_\mu \sin\theta_W, \tag{1.35}$$

$$A_\mu = \frac{gW^3_\mu + g'B_\mu}{\sqrt{g^2+g'^2}} = W^3_\mu \cos\theta_W + B_\mu \sin\theta_W, \tag{1.36}$$

where θ_W is the *Weinberg angle*, which represents the weak mixing angle in the Weinberg–Salam theory of the electroweak interaction:

$$g' = g \tan\theta_W. \tag{1.37}$$

Finally we obtain:

$$M^2_Z = \frac{v^2\,(g^2+g'^2)}{4}, \quad M_W = M_Z \cos\theta = \frac{gv}{2}. \tag{1.38}$$

In conclusion, let us note how the BEH mechanism is able to give a mass to fermions, which are necessarily massless in principle because of gauge invariance. At first let us observe the piece of Lagrangian which describes the exchange of a vector boson $W^\pm$ and Z^0 in a leptonic doublet:

$$\mathcal{L}_{Yukawa} = -\frac{g^2}{2\,M^2_W} \bar{\nu}_L \gamma^\mu e_L \bar{e_L} \gamma_\mu \nu_L, \tag{1.39}$$

$$\mathcal{L}_{Yukawa} = \frac{g}{\cos\theta} Z_\mu [\frac{1}{2}(\bar{\nu}_L \gamma^\mu \nu_L - \bar{e}_L \gamma^\mu e_L) + \sin^2\theta\, \bar{e}\gamma^\mu e]; \tag{1.40}$$

more generally:

$$\mathcal{L} = -\frac{G_e}{\sqrt{2}} v(\bar{e_L} e_R + \bar{e_R} e_L) - \frac{G_e}{\sqrt{2}} (\bar{e_L} e_R + \bar{e_R} e_L) h; \tag{1.41}$$

the first term is responsible for the creation of a mass term $-m\bar{\psi}\psi$, while the second one represents the interaction between the particle and the *Higgs boson*.
The Higgs boson is a particle predicted by the SM necessary in the BEH mechanism. It has been the main actor of the experimental research for many decades up to its discovery in 2012. Actually its nature is known: it is a massive neutral scalar boson (spin $s = 0$).

A correct choice of $\frac{G_e}{\sqrt{2}} v = m_e$ implies the creation of fermion mass; the coupling between Higgs boson and fermions is proportional to the fermion masses. Here we will not deal with the inclusion of the other two lepton generations and of quarks in the theory. Let us add only that in 1971 M. Veltman and G. 't Hooft demonstrated that the theory was renormalizable.

"*An optimist might say that we are on the road to the first truly unified theory of the fundamental interactions. All of these marvellous developments are based upon the ideas of spontaneous symmetry breakdown and gauge fields.*"
(S. Coleman, 1973)

This definitive success made the electroweak theory the most impressive application of SSB and BEH mechanism, providing a consistent and predictive model later confirmed by experimental results, that will be described in the next section.

1.3 The Higgs boson discovery

1.3.1 Search for the Higgs boson: from LEP and Tevatron to LHC

The SM theory was not able to predict mass m_H of the Higgs boson. Therefore, the particle had to be searched for in the widest possible mass range. In the first studies, the Higgs boson has eluded detection and lower limits on its mass were set [15, 16, 17].

Comparing SM predictions with precision electroweak data, collected by LEP (*Large Electron-Positron* collider at CERN, *European Organization for Nuclear Research*), SLC (*Stanford Linear collider* at SLAC) and Tevatron ($p\bar{p}$ collider at Fermilab), an indirect experimental bound on the SM Higgs boson has been placed by using a global fit on electroweak parameters in which m_H was the only free parameter. For example, Figure 1.3 shows one of the last measurements before the discovery, where the mass value was supposed to be $m_H < 154$ GeV at 95% of confidence level (CL) [18].

The direct searches at LEP up to the final year of operation (2000), allowed to determine a lower bound on the Higgs mass using data collected at energies between

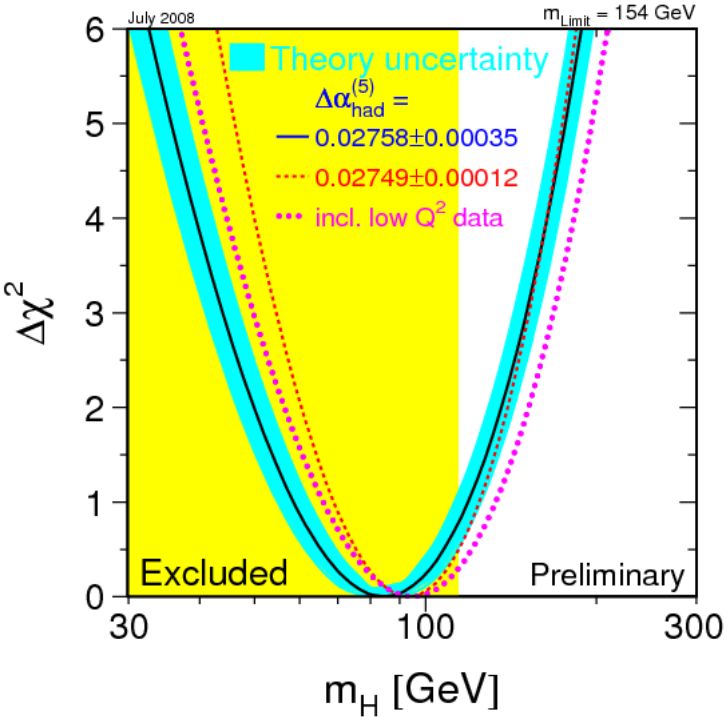

Figure 1.3: Experimental limits on the SM Higgs boson mass given by a global fit on electroweak parameters.

$\sqrt{s} = 189 - 209$ GeV (2461 pb^{-1}, of which 536 pb^{-1} were accumulated at $\sqrt{s} > 206$ GeV). A signal with mass $m_H \leqslant 114.4$ GeV was excluded at 95% CL.
Moreover, at the Tevatron a mass in the range of 162-166 GeV was excluded at 95% CL.

Successively, one of the most important prospects for the *Large Hadron Collider* (LHC) at CERN laboratory, the most powerful particle accelerator in the world, was to observe the Higgs boson. In fact, thanks to its high energy LHC offered a greater capability to explore large mass ranges. The details about the observation of a new particle with mass near 125 GeV, compatible to the SM predictions, by the ATLAS and CMS experiments is given in the next section.

1.3.2 Higgs production and decay modes at LHC

Let us review briefly the main production mechanisms of the SM Higgs boson in proton-proton collisions at LHC [19]. The various cross-sections are presented as a function of the center-of-mass energy in Figure 1.4 and in Table 1.1.

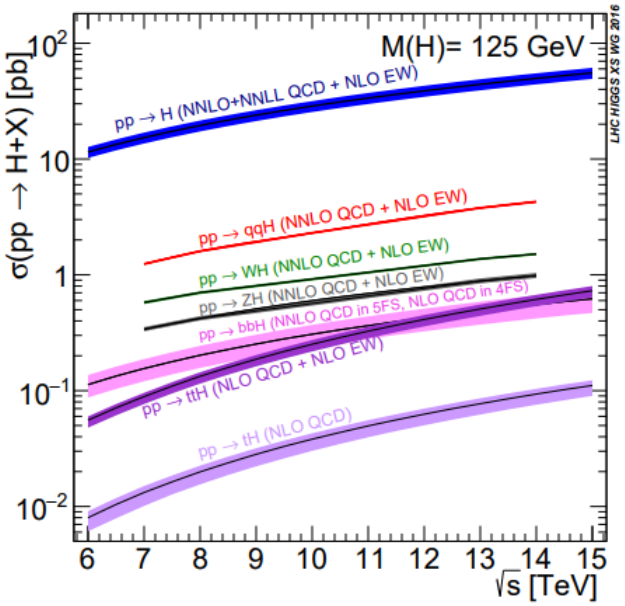

Figure 1.4: The SM Higgs production cross-sections as a function of $\sqrt{s}$.

Gluon-gluon fusion This production mode is the dominant one contributing to the Higgs boson production in the whole mass range. It presents the highest cross-section due to the high luminosity of gluons in p-p collisions. At his Leading-Order (LO), the gluon fusion produces a Higgs boson through a triangular loop of heavy top quarks (Figure 1.5). Radiative corrections are significant: in fact, considering Next-to-Leading-Order (NLO) and Next-to-Next-to-Leading-Order (NNLO) QCD corrections, the cross-section increases by a factor of about 50% and 30-40%, respectively.

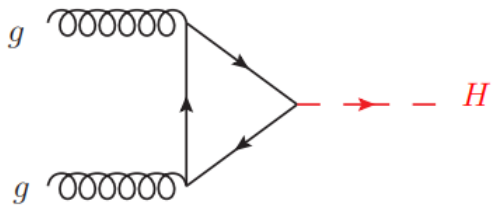

Figure 1.5: Higgs boson production through gluon-gluon fusion.

Vector boson fusion In this production mode, two quarks take part in a weak process which leads them to emit a vector boson each; thus the fusion of these two vector bosons produces H (Figure 1.6). It represents the second dominating contribution to the Higgs production. This production mode presents a clear experimental signature of signal associated with two hadronic jets in the very forward regions (at

$\sqrt{s}$	**Production cross-section for** $m_H = 125$ **GeV (pb)**					
	ggF	VBF	WH	ZH	$t\bar{t}H$	Total
7	$15.3^{+10\%}_{-10\%}$	$1.24^{+2\%}_{-2\%}$	$0.58^{+3\%}_{-3\%}$	$0.34^{+4\%}_{-4\%}$	$0.09^{+8\%}_{-14\%}$	17.5
8	$19.5^{+10\%}_{-11\%}$	$1.60^{+2\%}_{-2\%}$	$0.70^{+3\%}_{-3\%}$	$0.42^{+5\%}_{-5\%}$	$0.13^{+8\%}_{-13\%}$	22.3
13	$44.1^{+11\%}_{-11\%}$	$3.78^{+2\%}_{-2\%}$	$1.37^{+2\%}_{-2\%}$	$0.88^{+5\%}_{-5\%}$	$0.51^{+9\%}_{-13\%}$	50.6
14	$49.7^{+11\%}_{-11\%}$	$4.28^{+2\%}_{-2\%}$	$1.51^{+2\%}_{-2\%}$	$0.99^{+5\%}_{-5\%}$	$0.061^{+9\%}_{-13\%}$	57.1

Table 1.1: The SM Higgs boson production cross-sections (in pb) for $m_H = 125$ GeV as a function of $\sqrt{s}$ in pp collisions at LHC [19].

small angle with respect to the beam axis); for this reason, it is possible to obtain a good separation from background.

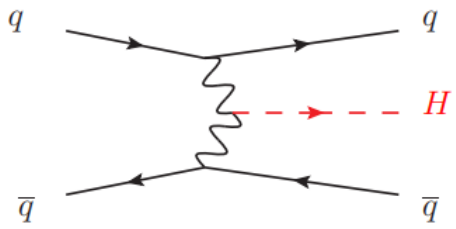

Figure 1.6: Higgs boson production through vector boson fusion.

Higgs-strahlung This production mode is the third dominating mode at LHC. In this case, the Higgs boson is "irradiated" from a vector boson ($W^{\pm}$ or Z^0); the internal line of the Feynman diagram represents a virtual boson produced during the interaction (Figure 1.7). It is an important production mechanism because it provides unique information on VH coupling, where V indicates a vector boson ($W^{\pm}$ or Z^0).

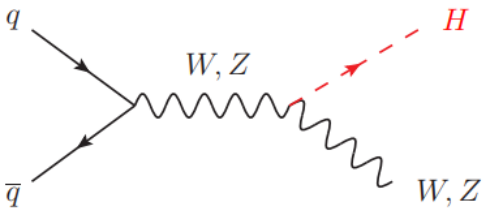

Figure 1.7: Higgs boson production through Higgs-strahlung.

$t\bar{t}$ fusion This process describes the production of a top-antitop pair ($t\bar{t}$) originated by two gluons; Higgs boson is produced by the fusion of a top and an anti-top (Figure 1.8). The channel is characterized by a final state including the Higgs boson and two top quarks; so it could be exploited to measure Higgs coupling with this particle directly. It is the smallest contribution to the Higgs production.

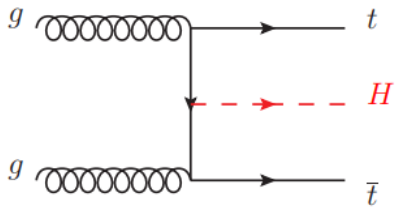

Figure 1.8: Higgs boson production through $t\bar{t}$ fusion.

The interaction vertex between the Higgs boson and a fermion f, the so-called *Yukawa vertex*, is shown in Figure 1.9, so-called *Yukawa vertex*.

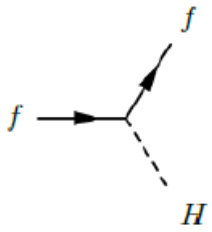

Figure 1.9: Yukawa interaction vertex between the Higgs boson (H) and a fermion f.

As mentioned before (at the end of section 1.2.4), the Higgs coupling to fermions is proportional to the fermion masses:

$$g_{f\bar{f}H} = \sqrt{\sqrt{2}\,G_F}\; m_f. \tag{1.42}$$

Vector bosons $W^{\pm}$ and Z^0 also interact with the Higgs particle through cubic or quartic vertices; their couplings are linearly dependent on the square of boson masses:

$$g_{VVH} = 2\sqrt{\sqrt{s}\,G_F}\; m_V^2, \tag{1.43}$$

where V stands for Z or W. Consequently, the mean lifetime and the total width Γ depend on the Higgs boson mass and the branching ratios (BR) of possible Higgs decay modes depend on the mass of the particles in the final state. For a Higgs mass of ~ 125 GeV, the Higgs total width is $\Gamma_H = 4.07 \times 10^{-3}$ GeV, corresponding to a mean lifetime of 1.6×10^{-19} s [19].

A Higgs mass of about 125 GeV provides an extraordinary occasion to investigate the Higgs couplings to many SM particles.
The dominant decay mode of a light Higgs boson [19] is $H \to b\bar{b}$, with a BR of 58%, followed by $H \to W^+W^-$ (2%) and $H \to ZZ^*$ (0.3%). These two channels are studied using the decay of each vector boson into a pair of fermions. Then there are $H \to gg$, $H \to \tau^+\tau^-$ and $H \to c\bar{c}$; the rates for decays as $H \to \gamma\gamma$, $H \to \gamma Z$, $H \to \mu^+\mu^-$ are very small. However, the $H \to \gamma\gamma$ decay channel (through a top loop) ensures a very clean signature and has been fundamental for the Higgs discovery. Moreover, since the decay channels into two photons, two gluons or $Z\gamma$ are induced by a vector boson or top-quark loop, they offer a useful mean to investigate Higgs coupling to these SM particles.

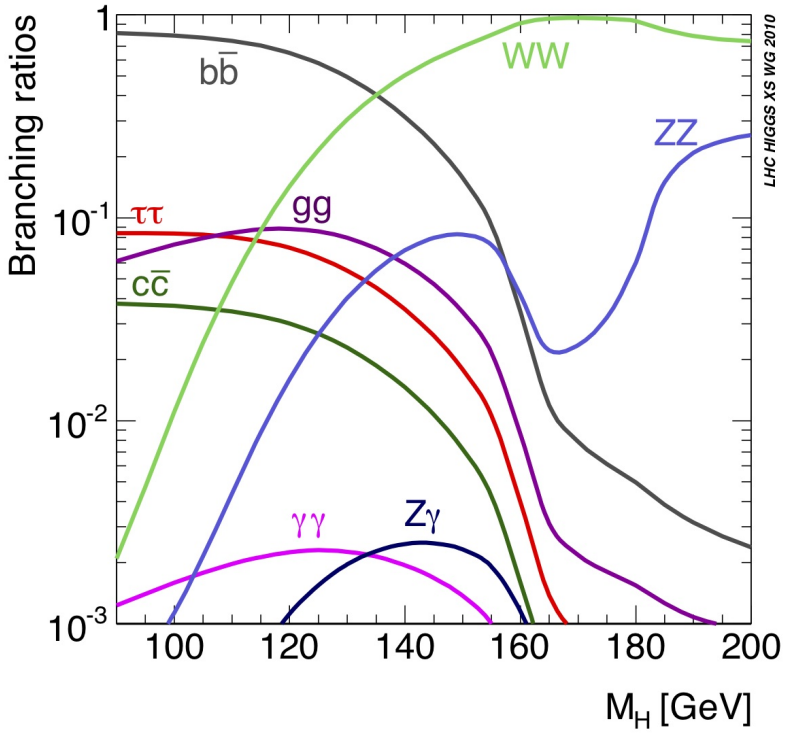

Figure 1.10: BR of the most relevant decay channels of the SM Higgs boson in the mass region near 125 GeV.

Table 1.2 lists some of the main decay channels of the Higgs boson, shown in Figure 1.10, each with its BR and relative uncertainty. These uncertainties are due to the missing higher-order corrections in the theoretical calculations on one hand and the errors on the SM input parameters on the other hand (in particular fermion masses and the QCD gauge coupling).

DECAY CHANNEL	BR	RELATIVE UNCERTAINTY
$H \to \gamma\gamma$	2.27×10^{-3}	$^{+5.0\,\%}_{-4.9\,\%}$
$H \to ZZ$	2.62×10^{-2}	$^{+4.3\,\%}_{-4.1\,\%}$
$H \to \mathrm{W^+W^-}$	2.14×10^{-1}	$^{+4.3\,\%}_{-4.2\,\%}$
$H \to \tau^+\tau^-$	6.27×10^{-2}	$^{+5.7\,\%}_{-5.7\,\%}$
$H \to b\bar{b}$	5.84×10^{-1}	$^{+3.2\,\%}_{-3.3\,\%}$
$H \to Z\gamma$	1.53×10^{-3}	$^{+9.0\,\%}_{-8.9\,\%}$
$H \to \mu^+\mu^-$	2.18×10^{-4}	$^{+6.0\,\%}_{-5.9\,\%}$

Table 1.2: BR for the main decays of the SM Higgs boson and relative uncertainties [19].

1.3.3 The Higgs boson discovery at the ATLAS and CMS experiments

Since the Higgs cross-section and its total width depend strongly on the unknown Higgs mass, the search for this particle covers a large mass spectrum and different decay channels: pair of vector bosons, pair of photons, pair of quarks $b\bar{b}$ or leptons $\tau^+\tau^-$.
The ATLAS and CMS experiments studied five main decay modes[2] in the mass region between 100 GeV and 1 TeV:

- $H \to \gamma\gamma$
- $H \to ZZ$
- $H \to W^+W^-$
- $H \to b\bar{b}$
- $H \to \tau^+\tau^-$

On 4^{th} July 2012, the ATLAS and CMS experiments at LHC presented their results [20, 21], announcing that they had each observed an excess of events over the expected backgrounds in the mass region around 125 GeV, consistent with the SM Higgs boson's production and decay.

[2]The Z and $W^{\pm}$ were allowed to be off-mass shell as well.

"*You need a lot of motivation, a lot of energy, and a lot of curiosity, [...] The search for knowledge is a long and difficult task.*"
(F.Gianotti, ATLAS spokesperson, 2012)

The most significant evidence was given by the following two channels, which guaranteed the best mass resolution and allowed a good sensitivity for a large spectrum of masses:

$H \to \gamma\gamma$ In this channel two photons are requested; the identification criteria is based on the configuration of shower in the electromagnetic calorimeter and missing energy in the hadronic calorimeter[3]. Invariant mass distribution is characterized by a very narrow peak in the mass region of 110-150 GeV. Dominant backgrounds are $\gamma\gamma$ production and events including γ + jet and jet + jet, where one or two jets are mis-identified as photons. The Higgs decay into two photons ensures that new particle's spin is different from 1 [22].

$H \to ZZ^* \to 4l$ $(l = e, \mu)$ In this analysis Higgs candidates are identified as two pairs of isolated leptons with same flavour and opposite charge. The decay into a pair of vector bosons indicates that the new particle is a boson [23].
A more detailed discussion of this channel is presented in the following paragraph, because it is the main topic of this thesis.

Both experiments observed clearly a new scalar boson with $m_H \sim 125$ GeV, combining data collected during the years 2011 and 2012 at energies $\sqrt{s} = 7$ TeV and $\sqrt{s} = 8$ TeV, respectively (Figure 1.11). The significance of observation, given in Table 1.3, exceeds 5σ in both cases.

Plots (a) and (b) in Figure 1.11 show the invariant mass distribution of two photons above the total expected background at center-of-mass energies $\sqrt{s} = 7 - 8$ TeV, related to the $H \to \gamma\gamma$ analysis. Under them, plots (c) and (d) show the distribution of the four-lepton invariant mass for the $H \to ZZ^* \to 4l$ analysis.
The Higgs boson mass was estimated using different decay modes, among which above mentioned channels were the most relevant; Table 1.3 shows measurements presented by CMS and ATLAS experiments on the date of the announcement of the Higgs discovery:

ATLAS	$m_H = 126 \pm 0.4$ (stat) ± 0.4 (syst) GeV/c^2	$5.9\,\sigma$
CMS	$m_H = 125 \pm 0.4$ (stat) ± 0.5 (syst) GeV/c^2	$5.0\,\sigma$

Table 1.3: Measured mass for the Higgs boson by ATLAS [20] and CMS [21] experiments in 2012. The observation significance is also given.

[3]Calorimeters as well as other sub-detectors are described in more detail in the contest of the CMS experiment in the next chapter

"*It is somewhat surreal to find that work we did nearly fifty years ago is once again at the center of attention. This is a triumph for the standard model of particle physics, but even more for the experimenters. The achievement of the two great experimental collaborations reported here is quite magnificent.*"
(T. Kibble, C. R Hagen and G. Guralnik, 2012)

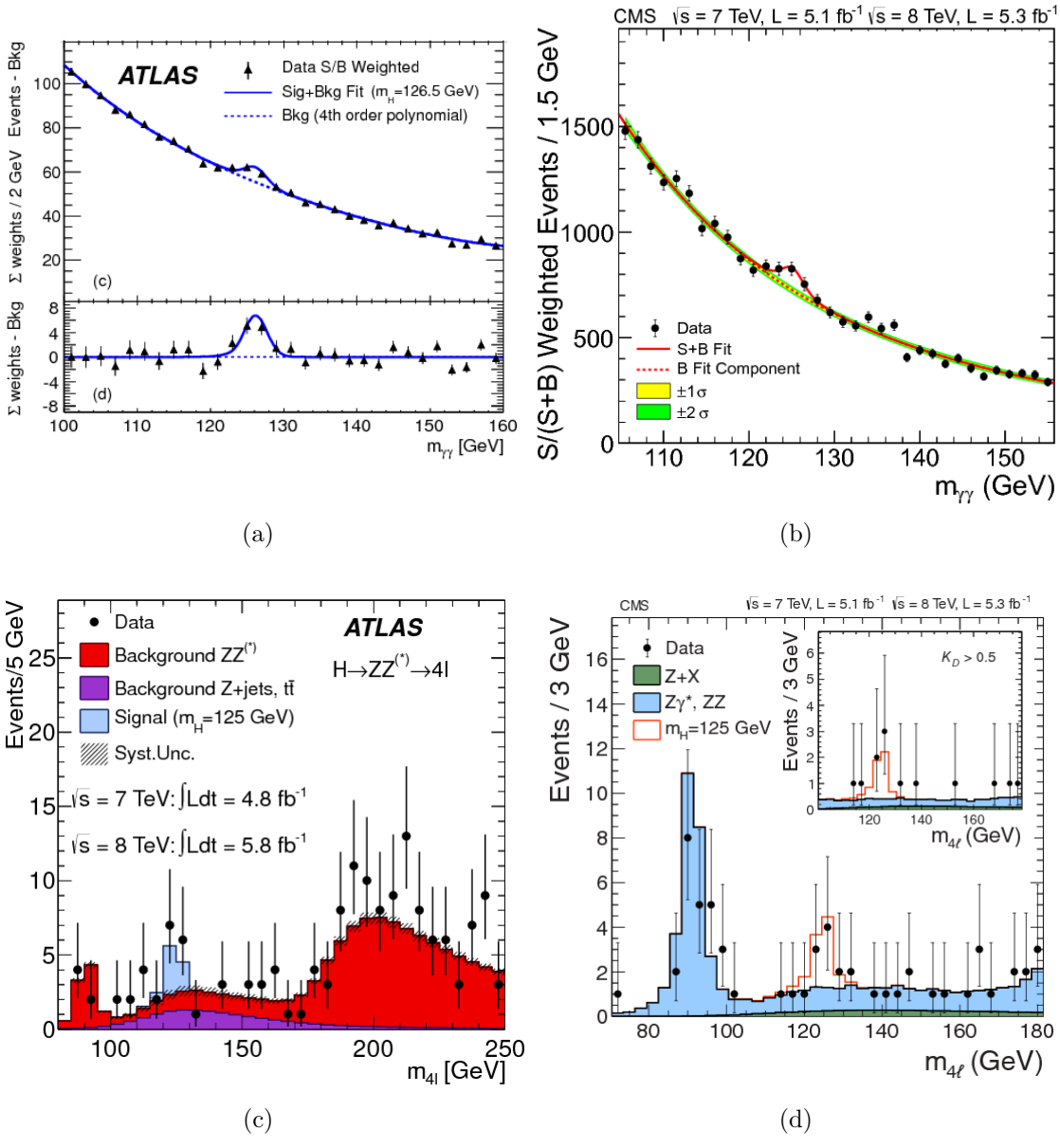

Figure 1.11: ATLAS (left) and CMS (right) distributions of the invariant mass of diphoton candidates (a, b) and of four-leptons candidates (c, d) after all selections using the combined 7 TeV and 8 TeV data samples [20, 21].

"*We're probing something that our theories can't handle, [...] What's great about having the particle is that we now have the source of the problem in our laboratory.*"
(J. Incandela, CMS spokesperson, 2012)

Since then more accurate measurements have been performed, which have validated and confirmed the hypothesis that the new particle was effectively the predicted Higgs boson of the SM.
Today the experimental research is geared towards improving measurements of the Higgs boson properties as precisely as possible and studying its couplings with particles of the SM, particularly with the quark top and the vector bosons $W^{\pm}/Z^0$.

1.3.4 The golden channel: $H \to ZZ^* \to 4l$ $(l = e, \mu)$

Since in this work the Higgs decay in the four-muons final state via ZZ^* production has been studied, the Higgs decay mode into four leptons (Figure 1.12) is presented in more details.
It is known as the "golden channel" because its final state is completely reconstructed and it is characterized by a clean signature. Thus it offers the possibility of an excellent reconstruction of the event and a good separation from backgrounds, together with a high efficiency.

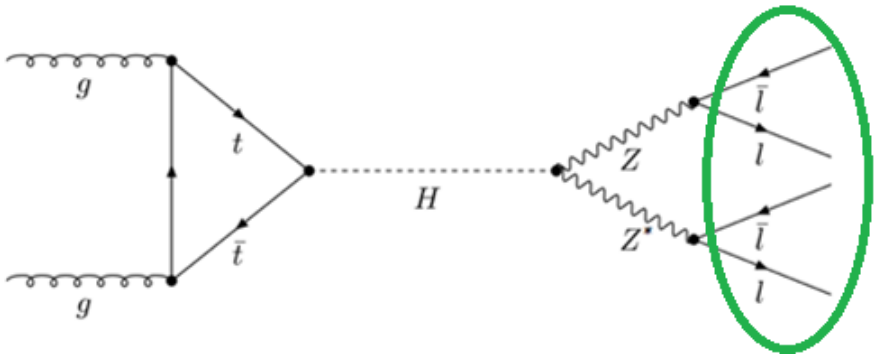

Figure 1.12: Feynmann diagram for the process $H \to ZZ^* \to 4l$.

As mentioned before, to select a Higgs candidate two pairs of isolated leptons are required, having same flavour and opposite charges. Hence, search for Higgs boson essentially relies on reconstruction and identification of leptons isolated from other particles in the event. Because of the presence of four leptons in the final state, to select this process a crucial role is played by the electromagnetic calorimeter and the muon system.

The main background sources for this channel are:

- The irreducibile non-resonant background around 125 GeV due to the SM ZZ production derives from direct production of neutral vector bosons in $q\bar{q}$ or gluon-gluon processes (Figure 1.13).

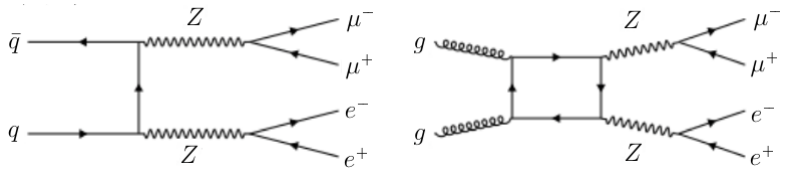

Figure 1.13: Feynmann diagrams for the irreducible ZZ background.

- The reducible background is mainly consist of Z+jets, WZ+jets and $t\bar{t}$ events, in which final states contain two or three isolated leptons and additional jets which can produce secondary leptons (Figure 1.14). Extra leptons can either come from heavy-quarks decay or from light-quark or gluon-jets misidentification.

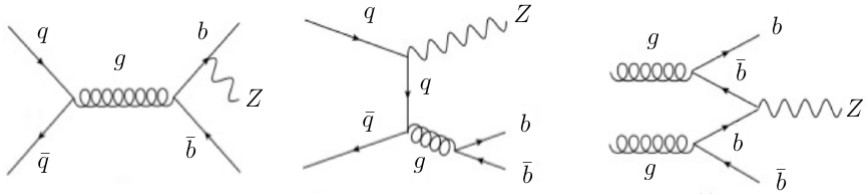

Figure 1.14: Feynmann diagrams for the reducible background Z + jets.

For all these reasons, in these studies for the Phase-2 muon detector upgrade the $H \to ZZ^* \to 4\mu$ plays an extremely important part.

Chapter 2

LHC and the CMS experiment

"*Machines take me by surprise with great frequency.*"
(A. Turing, 1950)

2.1 High energy physics at the LHC

The Large Hadron Collider (LHC) [15, 25, 26, 24] is a gigantic machine built at CERN laboratory near Geneva (Figure 2.1), spanning the boarder between Switzerland and France. The LHC is installed in the 27 km tunnel that was built for CERN's previous big accelerator, LEP, in operation until 2000, at a mean depth of 100 m. Today, the LHC is the world's most powerful particle accelerator and it presents the most extraordinary challenges that particle physics has ever faced.
The design of such accelerator aims at studying rare events produced in proton-proton (p-p) collisions at high center-of-mass ($\sqrt{s}$ up to 14 TeV) and at investigating the smallest fundamental building blocks that constitute our universe.

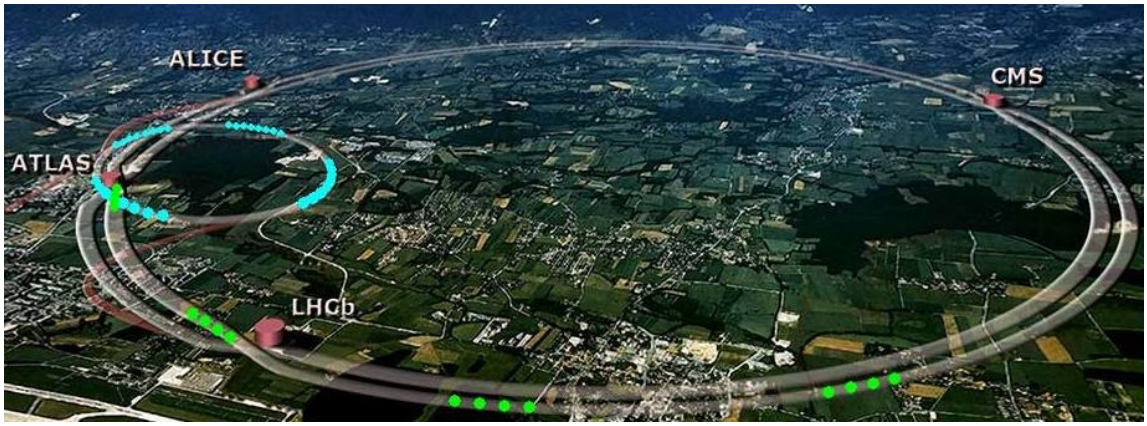

Figure 2.1: Aerial view of the LHC with the location of the four main experiments.

It is a two-ring low-temperature superconducting collider, able to accelerate two beams of hadrons (protons) or ions travelling in opposite directions at a speed very close to the speed of light. The beams cross in four points of the two rings: four experiments are located around these points. The collider is organized in eight arcs and straight sections; each straight section is approximately 528 m long and can serve as an experimental or utility insertion.

2.1.1 A historical account of the origin and development of the LHC

During the 1980's the LEP collider was being designed and built, but meanwhile a committee of physicists at CERN were focusing on a joint project for the next big particle accelerator, involving the United States and Europe. In June 1994 representatives of the nineteen nations belonging to CERN met to consider final approval of the LHC project; the project was approved by the CERN Council in December [26]. Because of financial reasons, it was initially decided that the project would be set up in two stages. However, as a result of diplomatic activities and intense negotiations which ensured significant contributions from the non-Member States, the Council approved the construction of the machine in a single step. The LHC Conceptual Design Report was published in October 1995, containing a description of the accelerator's architecture and the basis for the consequent detailed development of the project.

Soon after, during the years 1996-1998, the CERN Collaboration officially approved the installation of four experiments on four sites: ALICE, ATLAS, CMS and LHCb, shown in Figures 2.1 and 2.2. Then, two smaller experiments were added: TOTEM (located near CMS) and LHCf (near ATLAS).
ATLAS (A Toroidal LHC Apparatus) [27] and CMS (Compact Muon Solenoid) [28] are two large general-purpose experiments, independently designed to study the widest possible range of physics at subatomic level, from the primary aim of searching for the Higgs boson to supersymmetry (SUSY) and extra dimensions. ALICE (A Large Ion Collider Experiment) aims to study heavy-ion collisions, exploiting Pb-Pb collisions to produce a state known as *quark-gluon plasma*, which is fundamental in order to discover the origin of particles that constitute the matter of our universe today rose up and to understand the phenomenon of confinement [29]. LHCb (LHC beauty experiment) focuses on the b-quark physics, the study of the CP violation and the slight asymmetry between matter and antimatter [30].

After long time spent in the construction and testing of magnet models and prototypes, the industrial production of all components was ready for installation in the tunnel: the LHC went into operation on the 23^{th} of November 2009 at a center-of-mass energy of $\sqrt{s} = 900$ GeV.
In order to increase the luminosity and the center-of–mass energy of the LHC to reach the original design conditions, and to perform ordinary maintenance, long

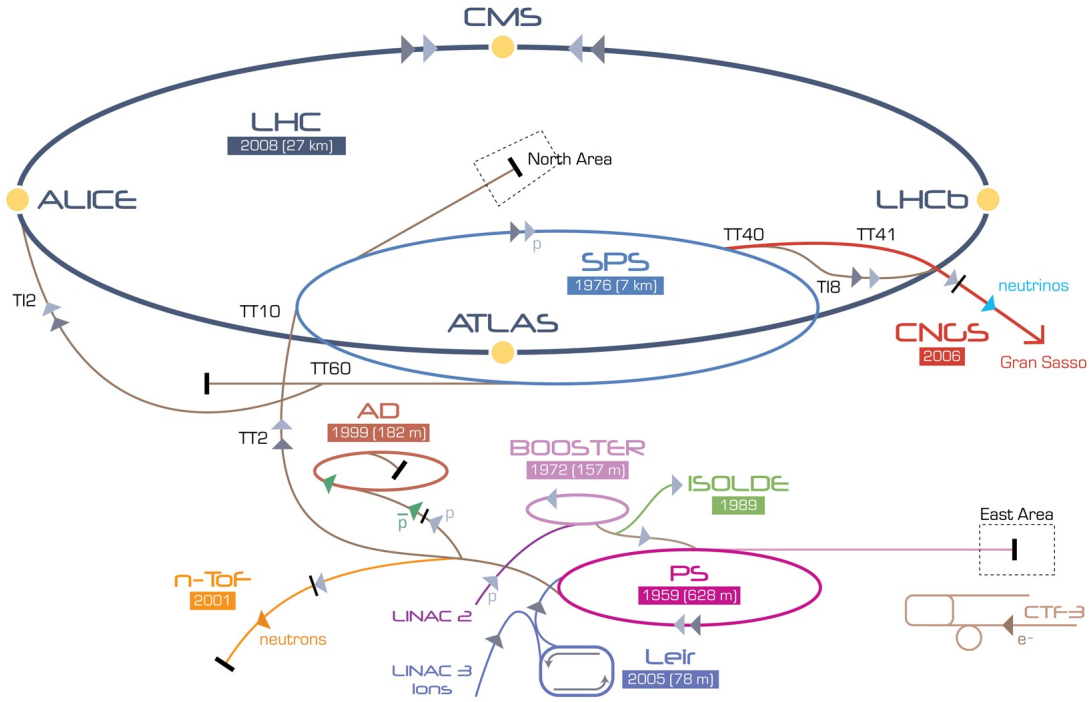

Figure 2.2: Schematic layout of the experiments around the circumference of the LHC and of the CERN accelerator complex.

shutdown periods are alternated with run periods.

Run-1 indicates the completed data-taking period in 2011 and 2012 (about 30 fb^{-1}), when collisions were characterized by a center-of-mass energy $\sqrt{s}$ = 7 - 8 TeV. The discovery of the Higgs boson dates back to this period.

Run-2 has begun in spring 2015, after the first Long Shutdown (LS1), and is still ongoing. The LHC has reached a proton-proton collision energy of $\sqrt{s}$ = 13 TeV: each beam is accelerated to an energy of 6.5 TeV. So far, an integrated luminosity of 35.9 fb^{-1} has been collected.

2.1.2 The CERN accelerator complex

Production and progressive acceleration of protons and beam injection in the LHC ring occur in different steps. Before arriving at the LHC, protons are prepared in a chain of smaller machines (Figure 2.2) with increasingly higher energies: each machine injects the beam into the next one, which accelerates the beam up to a higher energy, and so on.

1. Protons are obtained by stripping orbiting electrons from hydrogen atoms;

2. a *Linear Accelerator* (LINAC2) carries out the initial proton acceleration up to 50 MeV;

3. protons are then injected into the *Proton Synchrotron Booster* (PSB), where the beam is accelerated to 1.4 GeV;

4. protons are sent to the *Proton Synchrotron* (PS) and accelerated up to 25 GeV;

5. at this point, protons are sent to the *Super Proton Synchrotron* (SPS), where they reach an energy of 450 GeV;

6. protons are finally transferred in bunches to the two adjacent parallel beam pipes of the LHC, where they circulate for many hours around the ring in well-defined bunches, the first in a clockwise direction and the second in an anticlockwise direction.

2.1.3 Proton-proton physics at the LHC

To understand the requirements of the LHC experiments and the solutions adopted in the project of the machine, we need to review which kind of physics is expected to be studied at the collider.

At such collision energies, the elementary structure of protons plays an important role. Protons are composite particles, including not only three valence quarks, but also a sea of quarks-antiquarks and gluons, called *partons*, which is a manifestation of the strong confining forces. The proton internal structure can be modelled as a parton beam in which each parton carries a fraction x of the total momentum (Figure 2.3):

$$p_{parton} = xP_{proton}. \tag{2.1}$$

Parton Distribution Functions (PDF) describe the spatial distribution of partons as a function of x. Since the interactions occur between partons, there are a lot of particles that accompany a hard scattering, referred to as *underlying events*. Moreover, there is a non-null probability of multiple interactions in a single collision, called *minimum bias*: the extremely high luminosity (10^{34} cm^{-2} s^{-1}) of the LHC results in some 10^{16} minimum bias events in a full year!

The effective energy available in a collision ($\sqrt{\tilde{s}}$) is related to the nominal center-of-mass energy by the expression:

$$\sqrt{\tilde{s}} = \sqrt{s}x_a x_b,$$

where x_a and x_b are proton's momentum fractions carried by the two interacting partons.

In modern accelerators, the acceleration scheme is based on Radio Frequency (RF) fields and the bunch structure is a consequence of this. During a RF cycle,

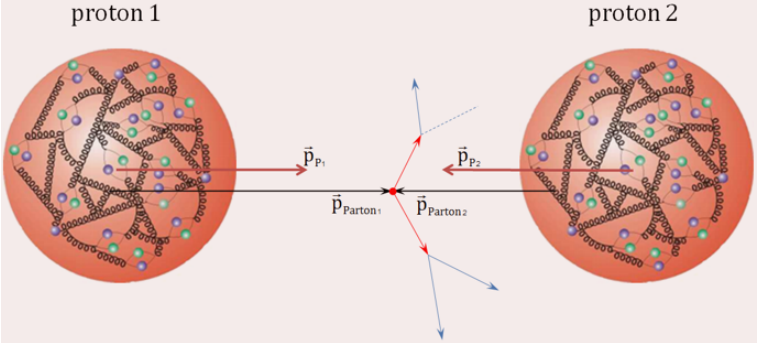

Figure 2.3: The elementary structure of the proton.

particles are only accelerated passing through an accelerating cavity, when the RF field presents the correct orientation.
In the LHC, under nominal operating conditions, each proton beam consists of 2808 bunches and each bunch contains as many as 10^{11} protons. Bunches of particles measure a few centimeters long and a millimeter wide when they are far from a collision point. However, the bunch size is not constant around the ring: circulating around the ring, each bunch gets squeezed and expanded. In fact, by squeezing its size as much as possible around the collision points (to about 16 mm), it is possible to increase the probability of a proton-proton collision.
The number of bunches represents an important parameter to influence luminosity $\mathcal{L}$ in a machine:

$$\mathcal{L} = f\frac{n_1 n_2}{4\pi\sigma_x\sigma_y}, \tag{2.2}$$

where n_1 and n_2 indicates the number of particles contained in Bunch1 and Bunch2 respectively, f represents the bunch crossing frequency and σ_x and σ_y are the transverse dimensions of the beam.
The LHC uses a bunch spacing of 25 ns (in Run-1 the bunch crossing interval was 50 ns), which corresponds to a frequency of 40 MHz. For every bunch crossing (on average about 40 million times a second) about 20 collisions between 200 billion particles takes place in the LHC. This fact implies the production of millions of particles and, consequently, many technical challenges.
The number of events per second produced (event rate) corresponds to:

$$R = \mathcal{L}\sigma_{proc}, \tag{2.3}$$

where σ_{proc} is the production cross-section of the physic process in question.

A strong magnetic field is required in order to maintain particles on a circular trajectory: the two beams are curved thanks to opposite magnetic fields. To bend protons in the LHC accelerator is necessary a magnetic field B with an intensity given by the equation:

$$p[\text{TeV}] = 0.3\, B[\text{T}]\; r[\text{km}], \tag{2.4}$$

where p is the momentum of the particle and r is the radius of the LHC.

2.1.4 The LHC collider

To build the LHC, the most powerful and technologically advanced superconducting electromagnetic dipoles and RF cavities have been developed.
A particle accelerator relies heavily on three elements [25]:

Vacuum A particular feature of LHC is having three separate vacuum systems, presenting different requirements with respect to classical vacuum systems: insulation vacuum for cryomagnets, insulation vacuum for the helium distribution line and beam vacuum.
On one hand, the requirements for the beam vacuum are the most stringent among the three, because it has to allow proper beam lifetime and background to the experiments avoiding collisions with gas molecules: heat input to the 1.9 K helium circuit in cryogenic system has to be reduced as much as possible. For this reason, the pressure is 10^{-13} atm (ultrahigh vacuum).
On the other hand, the insulation vacuum is the largest volume to be pumped in the LHC for the cryomagnets (~ 9000 m^3).

The magnet system The LHC presents separate magnetic fields and vacuum chambers in the eight arcs, alternated to straight sections which are at the insertion regions where the experimental detectors are located. The magnets are installed sector by sector; there are 154 dipoles per arc connected in series so that each sector is independent from the others.
In a collider, the maximum energy that can be achieved is directly proportional to the strength of the dipole field, responsible of a specific acceleration circumference. LHC is equipped with a large variety of magnets (dipoles, quadrupoles, sextupoles, octupoles, decapoles, etc.), which amount to a total of 9600. The most numerous ones are the dipoles (1232), but each family of magnets undertakes a specific task:

- dipoles provide the very high field of 8.3 T over their length, thanks to a high current which flows in them (for example, a current of 11000 A is necessary to bend the 7 TeV beams around the 27 km ring);
- quadrupoles are used to focus the beam in order to maximize the chance of two protons colliding head-on;
- high-order multipole magnets contribute to correct the field errors in the main ring magnets (dipoles and quadrupoles) and in the interaction region magnets.

The LHC is unique among superconducting synchrotrons because of its superconducting technology, based on niobium-titanium (NbTi) cables with an operating temperature of 1.9 K (–271.3°C). The LHC cryogenic system is based on the use of superfluid helium, which is pumped into the magnet system; it has a very high

thermal conductivity, ideal for the refrigeration and stabilization of large superconducting systems. The cooling of the elements is a fundamental activity in order to increase the performance of NbTi and maximize the field strength of the superconducting magnets.

Cavities LHC uses eight RF cavities per beam, which operate at 4.5 K and are characterized by small energy losses and large stored energy. They are grouped in fours in cryomodules, with two cryomodules per beam.
Their function is to accelerate the beams by exploiting RF fields and to squeeze proton bunches as compact as passible in order to make hand-on collisions easier and to guarantee high luminosity at the collision points.

2.1.5 Data processing

For what concerns the computing needs of the LHC experiments [31], the data flow from all four experiments amount to 15 PB per year: data come from 150 million sensors delivering signals 40 million times per second, reduced to about 100 collisions of interest per second. In order to have this enormous amount of data available for the analysis all around the globe, a data storage and analysis infrastructure has been provided for the entire high-energy physics community: the *Worldwide LHC Computing Grid* (WLCG).

The data are distributed according to hierarchical model which is organized in four levels, or *Tiers*, called 0, 1, 2 and 3 (Figure 2.4). Each Tier provides a specific set of services.

1. Initially, Tier-0 is the CERN Data Center and receives the raw data emerging from the data-acquisition systems, recording and roughly processing them.

2. Then, the data are distributed to 13 Tier-1 centers, which host computers with enough storage capacity for large amounts of data. Here the users carry out their analysis tasks requiring access to the permanent data storage (raw, processed and simulated data).

3. The Tier-1 centers make data available to Tier-2 centers (more than 100), which are typically universities, scientific institutes and laboratories. They have to provide adequate computing power and storage services for Monte Carlo event simulation and for end-user analysis. Then the data generated at Tier-2 centers are sent to Tier-1 centers for permanent storage.

4. At the end of the chain, individual scientists, which take part in the processing and analysis of the LHC data, can access the Grid through local (or Tier-3) computing resources.

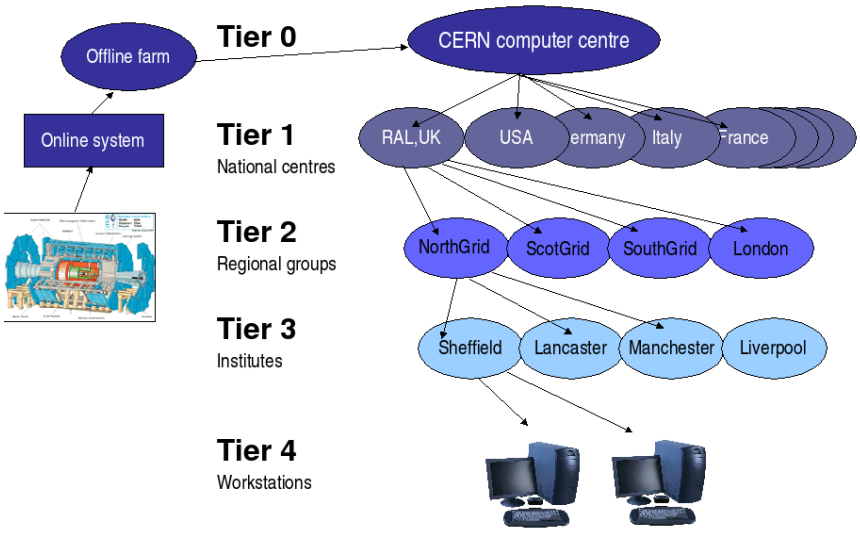

Figure 2.4: WLCG Tier structure.

2.2 The CMS experiment

"*We propose to build a general purpose detector designed to run at the highest luminosity at the LHC.*" (The CMS Collaboration, 1992)

More than 4000 people (scientists, engineers, technicians and students) from more than 202 institutes and 47 countries around the world are currently involved in the CMS collaboration, one of the largest international scientific organizations in history [32, 33, 34, 35]. The collaboration operates and collects data from the CMS detector.
The LHC provides extraordinary opportunities for particle physics: according to the main goals of the experiment, CMS is designed to detect a wide range of particles and phenomena produced in the LHC's high-energy proton-proton collisions to explore physics at the TeV scale. In order to study the phenomenon of electroweak symmetry breaking, it was optimized for the search of the SM Higgs boson in the mass region 90 GeV - 1 TeV, but it could detect a large variety of signatures arising from alternative electroweak symmetry breaking mechanisms. Finally, it also allows to study top, beauty and τ physics and heavy-ion collisions.
An unusual feature of the detector is that all sections of CMS were designed and constructed in various institutes across the globe before being brought to CERN for the final assembly instead of being built in-situ into an underground cavern near Cessy in France. The complete detector is a giant structure which measures 21.6 m in length and 15 m in diameter and totally weighs 14500 ton.

In the next sections, the physics capability of the CMS experiment and the strategy adopted by CMS to explore the rich physics programme offered by the LHC are illustrated.

2.2.1 The CMS detector design

According to the experiment's aims, the main design considerations of CMS are:

(i) a highly performant muon system,

(ii) a high quality electromagnetic calorimeter,

(iii) a robust and powerful central tracking system to achieve excellent charged particle reconstruction and detailed vertex reconstruction,

(iv) a hadron calorimeter characterized by good hermiticity and sufficient energy resolution.

Each part of CMS is optimized for the detection and measurement of a specific type of particle and the choice of the magnetic field configuration strongly influences the rest of the detector design. The CMS detector is built around the magnet, taking the form of a cylindrical coil of superconducting cable large enough to accommodate the inner tracker and the calorimetry inside.
A high magnetic field is needed to achieve a good momentum resolution; the field is confined by a steel "yoke" that forms the bulk of the detector. The result is a compact design for the muon spectrometer, hence the name Compact Muon Solenoid (CMS). A transverse view of CMS is shown in Figure 2.5.

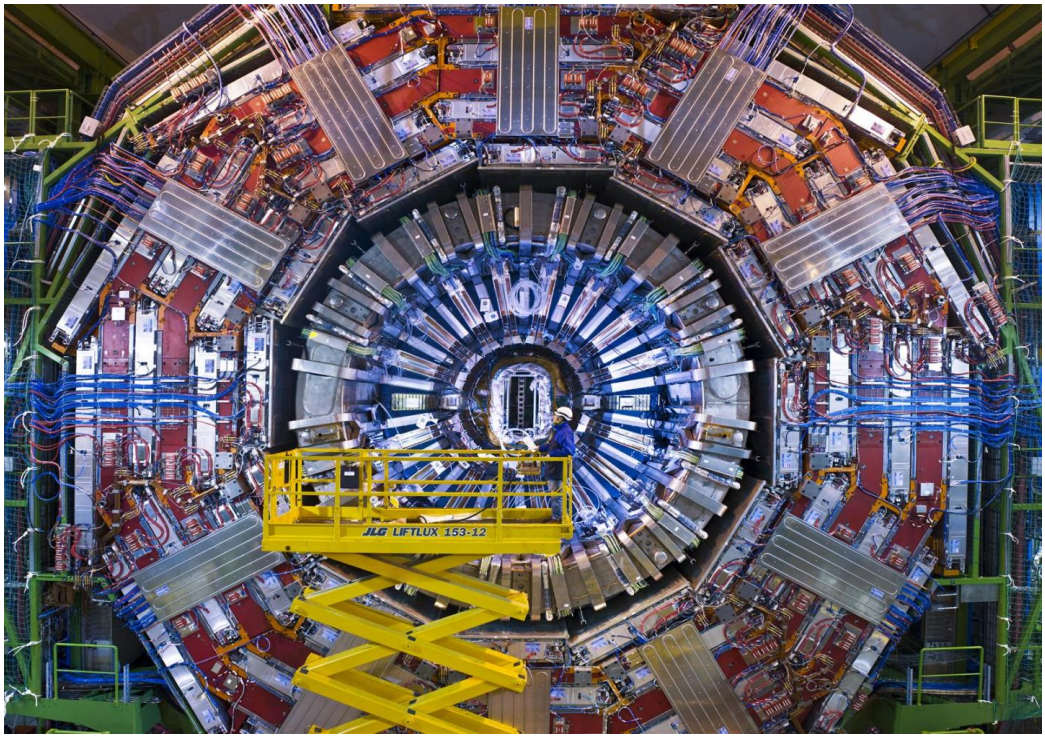

Figure 2.5: Transverse view of the CMS detector.

Protons collide in the center of the detector. On their way out, particles encounter the following sub-detectors (Figure 2.6):

- an inner **tracking system** based on silicon pixel and fine-grained micro-strip detectors;
- a fully active scintillating crystal **electromagnetic calorimeter**, necessary for the identification of photons and electrons thanks to the energy they deposit in the material;
- a brass-scintillator sampling **hadronic calorimeter**, which allows the identification of hadrons and the reconstruction of jets;
- a huge **solenoid magnet** located at the heart of CMS which provides a high uniform magnetic field of 3.8 T (about a hundred thousand times the magnetic field of the Earth!);
- a multilayer **muon system**, in which the muon detectors are organized in four stations interleaved with magnet return yokes to ensure robustness.

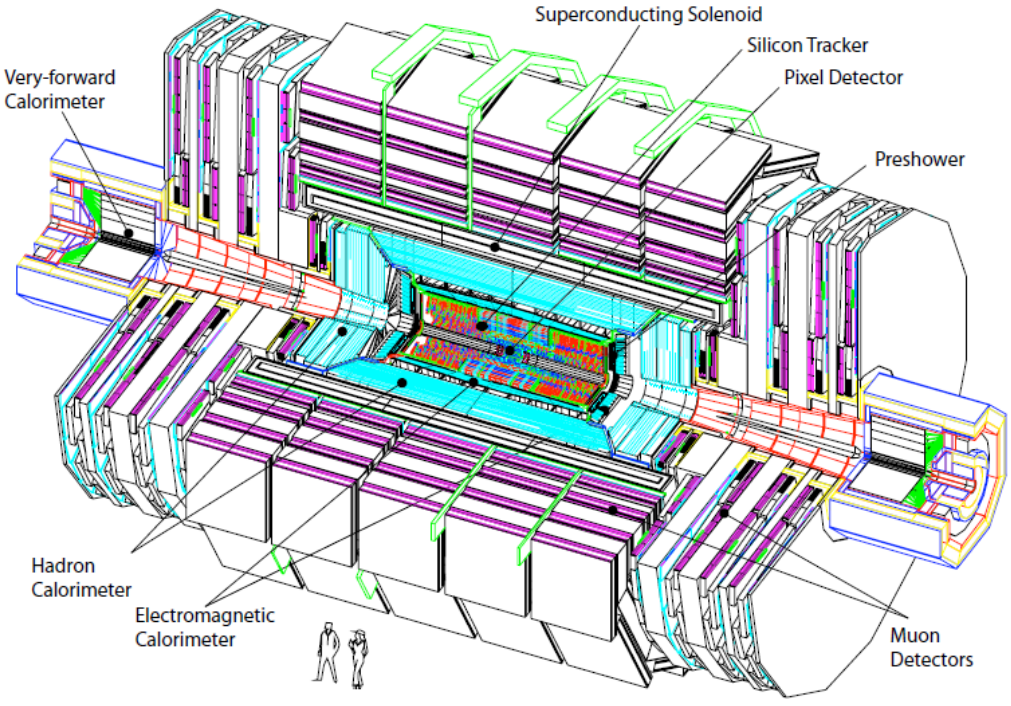

Figure 2.6: Overall view of the CMS detector.

2.2.2 The coordinate frame

In most particle physics experiments, the origin of the coordinate system is centered at the nominal collision point inside the experiment, situated on the longitudinal z-axis along the beam direction, while the x-y plane identifies the transverse plane (the x-axis pointing radially inward toward the center of the LHC and the y-axis pointing vertically upward). It is often convenient to describe four momenta of particles by their energy and two angles: the azimuthal angle ϕ is around the beam axis in the transverse plane, while the polar angle θ is measured from the z-axis.

Interesting physics concentrates on regions of the transverse plane at large η values, far from the beam pipe. Thus, the energy and momentum measured transverse to the beam direction are useful quantity to describe events generated during a collision and are denoted by E_T and p_T.
The transverse energy could be defined as:

$$E_T = E \sin\theta$$

The transverse momentum is Lorentz invariant under boosts along the z-axis, so it is possible to assume that it is conserved in the transverse plane:

$$p_T = \sqrt{p_x^2 + p_y^2}.$$

The missing energy is measured in the transverse plane and is denoted by E_T^{miss}:

$$E_T^{miss} = -\sum_i \vec{p_T} \quad \text{with} \quad |E_T^{miss}| = \sqrt{\Big(\sum_i p_x^i\Big)^2 + \Big(\sum_i p_y^i\Big)^2}.$$

Moreover, instead of using the polar angle θ, it is sometimes convenient to construct a quantity with better transformation properties under boosts along the beam axis, for example the *rapidity*, defined as:

$$y = \frac{1}{2} \log \frac{E + p_z}{E - p_z},$$

because rapidity differences remain invariant under boosts along the z-axis. It tends to zero for particles with only a transverse component of the momentum, while it tends to $\pm\,\text{inf}$ for particles parallel to the z-axis. However, this quantity does not provide an intuitive interpretation, so an analogue quantity is introduced, the *pseudorapidity*, denoted by η:

$$\eta = -\ln\Big(\tan\frac{\theta}{2}\Big).$$

Small values of the θ angle corresponds to large values of η. If $m << E$, these two quantities are more or less equal.

Finally, to describe particles in terms of η, ϕ and z, another quantity is defined, Δr, which provides a distance measurement in the $\eta - \phi$ plane:

$$\Delta R = \sqrt{\Delta\eta^2 + \Delta\phi^2},$$

where $\Delta\eta$ and $\Delta\phi$ represent the distance between two objects in terms of pseudo-rapidity and azimuthal angle respectively.

2.2.3 The magnet system

To bend the paths of final state particles from collisions in the LHC, the CMS detector uses a large superconducting solenoid [36] made of niobium-titanium (NbTi) cables wrapped with copper and enclosed in a 12000 ton iron yoke which is part of the outer muon detecting system.
Some of its main parameters are given in Table 2.1.
Compared to a toroid, an advantage is related to the smaller overall size: in fact a large bending power can be obtained for a solenoid with modest dimensions. Moreover with the field parallel to the beams, the bending of the track starts at the primary vertex ($R = 0$) and then continues in the transverse plane, where the transverse position of the vertex could be determined to an accuracy better than 20 μm thanks to the small dimensions of the beam. A strong bending allows for an efficient trigger, which depends on the vertex determination. Moreover, a good momentum resolution is a direct consequence of the high magnetic central field; the powerful tracking is ensured by a favourable length/radius ratio.

One of the main features which have guided the design of these magnets is the issue of stability, leading to choose, as shown in Figure 2.7:

- high-purity aluminium stabilized conductor able to front higher rated current and magnetic forces;

- indirect thermosiphon cooling to keep the magnet at $T = 4$ K to maintain the superconducting mode;

- a monolithic four-layer winding structure capable of sustaining all the induced magnetic forces by itself.

Nominal field	4T
Inner bore	5.9 m
Length	12.9 m
Number of turns	2168
Current	19.5 kA

Table 2.1: Parameters of the CMS superconducting solenoid.

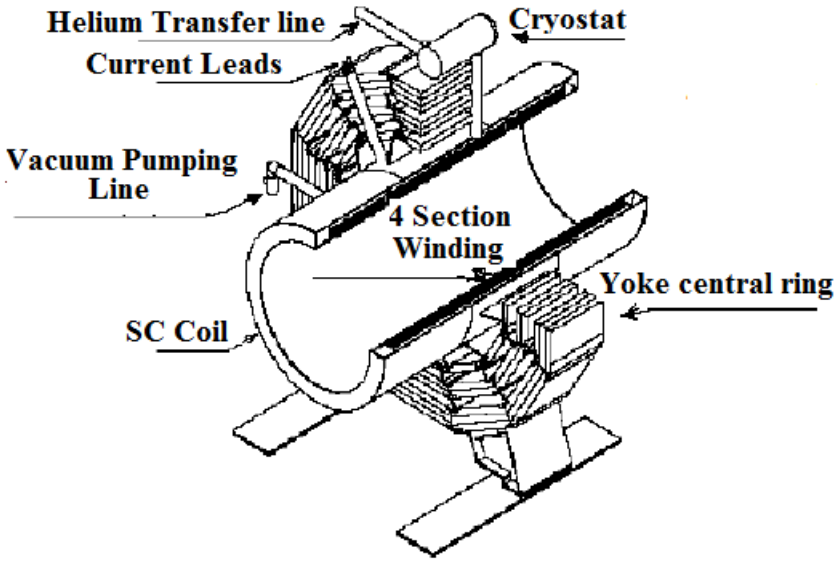

Figure 2.7: Open view of the cold mass.

The iron yoke plays the role of an absorber and is used to return the flux; it is divided into two main components.

- **The barrel yoke** is the cylinder surrounding the superconducting coil (1.8 T) and is divided along the beam axis into five 2.9 m long sections: the central barrel ring is fixed around the interaction point and supports the superconducting coil, while the other four sections can slide on rails along the beam direction; most of the muon chambers are inserted in the iron yoke. Each barrel ring is made up of three iron layers.

- **The endcap yoke** is composed of three independent rings that magnetically close the barrel yoke and can be separated to provide access to the forward muon stations. The high magnetic field has a direct impact in terms of forces, due to the axial magnetic attraction, on the two endcap yokes: to reinforce their structure, the first and second disks supporting the electromagnetic and hadronic endcap are made from two 300 mm thick solid plates.

The vacuum tank is made of stainless steel and accomodates the superconducting coil, symmetrically supported from it. On one hand, the outer shell of the vacuum tank is attached to the inner part of the central barrel ring; on the other hand, the inner shell supports all the barrel sub-detectors (tracker and calorimeters) via a system of horizontal welded rails.

2.2.4 The tracker

The primary design goal of the tracking system [37, 38], which is the largest tracker ever built for a collider experiment, is to provide good particle momentum resolution and efficient primary and secondary vertex reconstruction. In addition, to address the problem of pattern recognition at high luminosities, detectors with small cell sizes are required. Finally, it is important to reconstruct high p_T isolated tracks produced in the central rapidity region with a transverse momentum resolution better than $\delta p_T/p_T = (15 \cdot p_T \oplus 0.5)\%$. In fact, to identify isolated leptons it is fundamental to reconstruct all tracks with p_T greater than 2 GeV in the barrel region and to check that all interesting particles in an event are consistent with a common vertex.

The tracking volume is given by a cylinder 5.8 m long with a diameter of 2.6 m and is entirely made of silicon detectors, covering the region $|\eta| < 2.5$ with radius $R < 1.2$ m and $|z| < 2.7$ m. They are arranged in concentric cylindrical volumes: a barrel geometry characterizes the central pseudorapidity region, while at higher values of pseudorapidity the interaction region is surrounded by two endcap layers of silicon pixel detectors.
To solve stringent resolution and granularity requirements in the high, medium and lower particle density regions, two different detector technologies have been adopted, both characterized by a fast response (Figure 2.8).

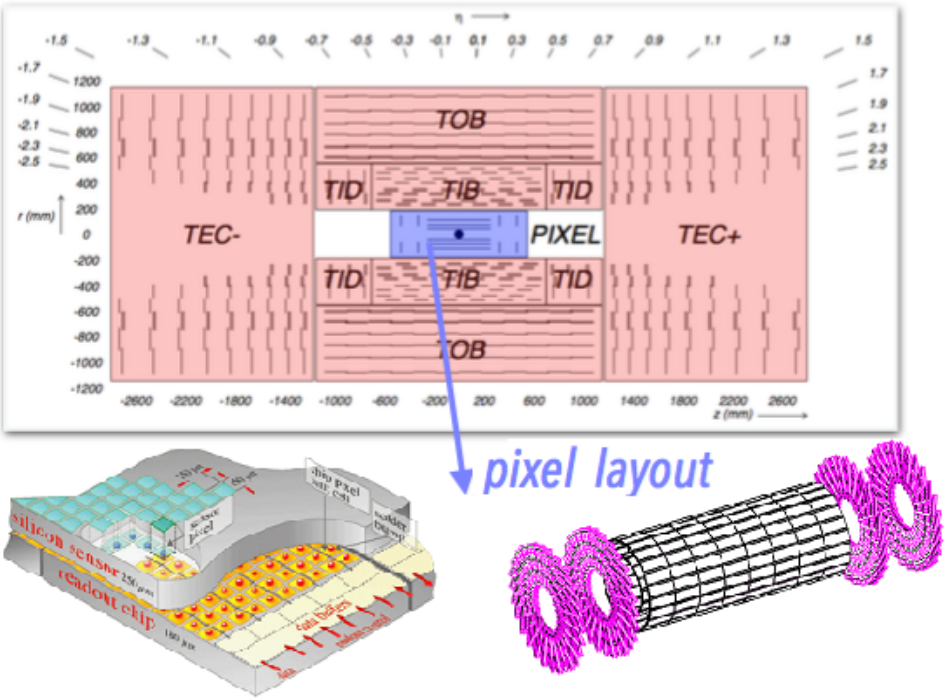

Figure 2.8: Transverse view of the CMS tracker, with a focus on the pixel system (right) and a pixel detector element (left).

- **Silicon pixel detectors** are placed in the inner region below 20 cm, close to the interaction point, to allow the measurement of the impact parameter of charged-particle tracks, as well as the position of secondary vertices.
  The CMS pixel system is constituted by three barrel layers at 4.3 cm, 7.3 cm and 10.4 cm and two endcap disks made of 24 blades in a turbine-like shape each on each side of the barrel. The layers are composed of modular detector units. These modules consist of a thin, segmented sensor plate with highly integrated readout chips: about 65 million pixel cells, each of 100×150 mμ^2 are grouped in 1400 sensors for a total surface of 1.06 m^2. They provide very low occupancy, high resolution and precise vertex reconstruction.
  For the barrel, in the $R - \phi$ direction hit resolutions at the 10 μm level can be obtained, while in the z-direction a spatial resolution of 15 μm is achieved for inclined tracks. Lower resolutions characterize the endcap regions (15 μm and 20 μm respectively).

- **Silicon micro-strip detectors** are organized in ten layers about 10 cm long in the outer region between 20 and 120 cm. On one hand, there are four inner barrel (TIB) layers and two inner endcaps (TID), each composed of three small rings. On the other hand, six concentric layers form the outer barrel (TOB) and two endcaps (TEC) close off the tracker.
  This part of the detector kept at operate temperature of -15°C is composed of 15200 highly sensitive modules with 10 million detector strips read by 80000 microelectronic chips. Each module consists of three elements: a set of sensors characterized by fast response and good spatial resolution, a mechanical support structure and readout electronics. Silicon micro-strips allow to reduce the number of read-out channels maintaining a good resolution and provide the required high granularity and precision keeping the cell occupancies below 1%. A spatial resolution of 40-60 μm is provided in the $R-\phi$ transverse plane and of 500 μm in the z-axis.

2.2.5 The calorimeter system

The combined CMS calorimeter system includes an electromagnetic calorimeter (ECAL), a hadron calorimeter (HCAL) and forward calorimeters (HF) [39, 42, 40, 41]; it is shown in Figure 2.9.
The central pseudorapidity range ($|\eta| < 3.0$) is covered by the barrel and endcap calorimeter system consisting of a hermetic crystal electromagnetic calorimeter (ECAL) surrounded by a brass/scintillator sampling hadron calorimeter, similarly divided in barrel (HB) and endcap (HE). In addition, thanks to two forward calorimeters around the beam pipe at $|z| = 11.2$ m and very close to the beam axis, a coverage up to $|\eta| < 5.0$ is obtained. Finally, an outer calorimeter (HO) is placed outside the magnet coil to obtain a better energy resolution of the barrel calorimeters.

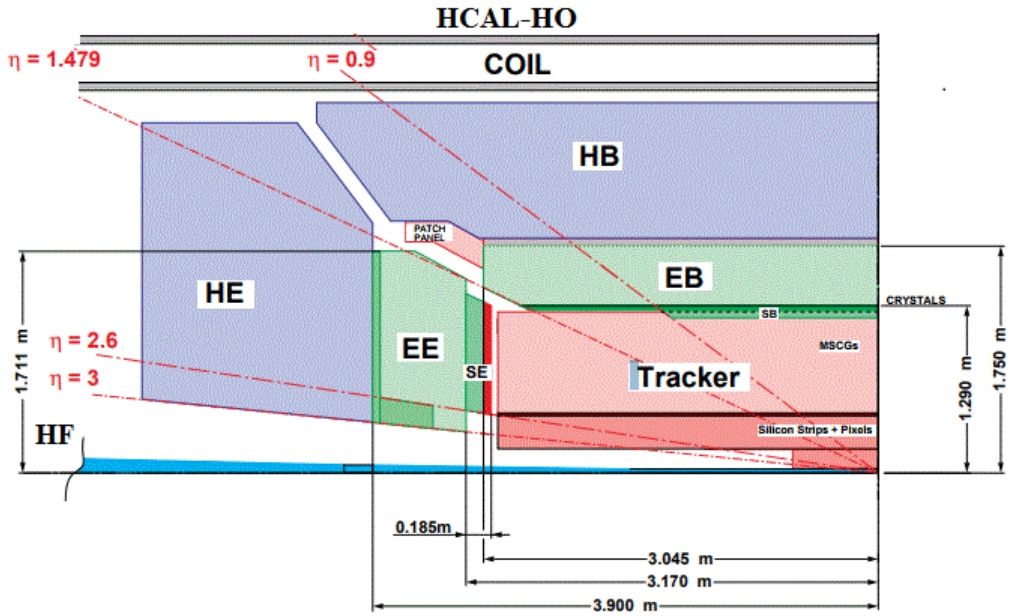

Figure 2.9: Schematic view of the CMS calorimetry system.

The search for the Higgs boson and for a large variety of SM and other new physics processes at the LHC strongly relies on the information from the calorimeters. The energies of the final state particles such as electrons and photons must be measured with high precision.
Moreover, an indirect measurement of the presence of non-interacting, uncharged particles provided by the calorimeters is crucial to compute the missing energy which could be a signature of new particles and phenomena.

ECAL

A scintillating crystal calorimeter ensures the best performance for energy resolution since most of the energy from electrons or photons is deposited within the homogeneous crystal volume of the calorimeter. The ECAL uses lead tungstate ($PbWO_4$) for the almost 80000 crystals which provide important physical and optical characteristics, such as compactness, high granularity, excellent time resolution and a fast scintillation response (about 80% of the light emitted in 25 ns). High density crystals ($\rho = 8.28$ g/cm^3) with a small Molière radius (2.2 cm) allow a very compact electromagnetic calorimeter system, with pseudorapidity coverage up to $|\eta| < 3.0$. The mechanical design of the ECAL is optimized for the use of $PbWO_4$ crystals: space used for the mechanical structure within the active volume of the calorimeter is minimized.

It is possible to distinguish two regions, as shown in Figure 2.10: the cylindrical barrel ECAL (EB) up to $|\eta| < 1.48$ and two endcaps ECAL (EE) in the region

$1.48 < |\eta| < 3.0$. A pre-shower system is installed for π^0 rejection just in front of the barrel ECAL (SB) and the endcap ECAL in the region $1.65 < |\eta| < 2.6$ (SE). The scintillation light produced through Bremsstrahlung and pair production is collected and amplified by silicon avalanche photodiodes (APDs) in the barrel region, since they can provide gain in the presence of the high transverse magnetic field. In the endcap region, vacuum phototriodes (VPTs) are used to compensate the relative low light yield of $PbWO_4$; here the photodetectors suffer from a much higher integrated radiation dose (50 kGy) and neutron fluence (7×10^{14} n/cm^2).

In the mass range 25-500 GeV, the energy resolution of the ECAL can be parametrized as:

$$\left(\frac{\sigma}{E}\right)^2 = \left(\frac{a}{\sqrt{E}}\right)^2 + \left(\frac{\sigma_n}{E}\right)^2 + (c)^2,$$

where

- E is the particle energy in GeV;
- a is a stochastic term which considers a photostatistics contribution and fluctuations on the lateral containment of the shower or on deposits of energy;
- σ_n is the noise, which contains three different contributions: preamplifier noise, digitization noise and pile-up noise;
- c is a constant term reflecting energy leakage of the crystals, non-uniformity of the longitudinal light collection and calibration errors.

Typical energy resolutions are measured with electrons; the excellent performance can be parametrized by a stochastic term of 2.8%, a noise term of 12% and a constant term of 0.3%.

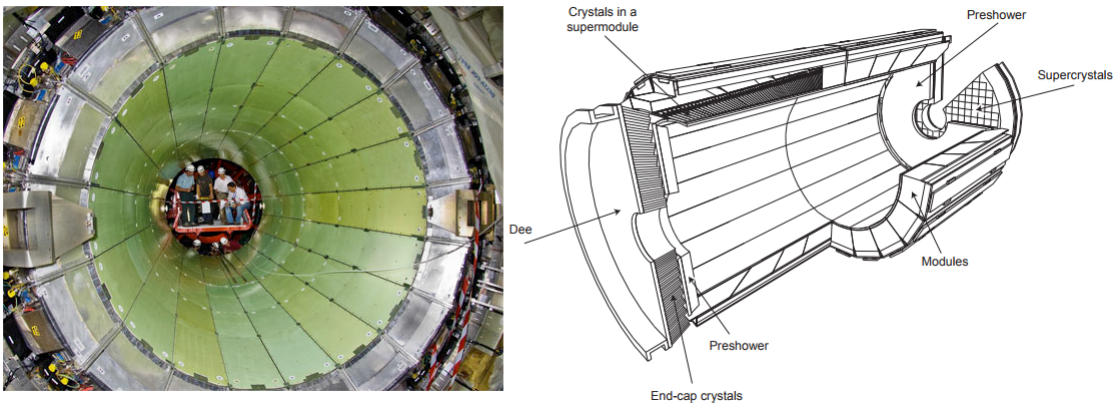

Figure 2.10: CMS electromagnetic calorimeter.

HCAL

The hadron calorimeter consists of a barrel part up to $|\eta| < 1.3$ and an endcap part in the region $1.3 < |\eta| < 3.0$, which contain more than 2500 channels respectively. The barrel part is installed between the ECAL and the coil from $R = 1.9$ m to $R = 2.95$ m, corresponding to a total of seven interaction lengths (λ) at $\eta = 0$ (10λ at $\eta \geqslant 1$). Brass absorber plates are alternated to the active medium (plastic scintillator tiles), coupled to an hybrid photo-detector (HPD) readout.
It is segmented with $\Delta\eta \times \Delta\phi = 0.087 \times 0.087$, necessary for the separation of nearby jets, the determination of their direction and an adequate mass resolution.

The expected hadronic energy resolution are:

$$\frac{\sigma}{E} \simeq \frac{65\%}{\sqrt{E}} \oplus 5\% \quad \text{(for HB)},$$

$$\frac{\sigma}{E} \simeq \frac{85\%}{\sqrt{E}} \oplus 5\% \quad \text{(for HE)}.$$

Forward calorimeters

The hermeticity of the detector is guaranteed by the forward calorimeters, which provide full geometric coverage for the measurement of the transverse energy in the event. They are subject to very high radiation and very high rate environment.
They are made of quartz fibers as active element, predominantly sensitive to Cerenkŏv light from neutral pions, embedded in a steel absorber: this design allows a very localized response to hadronic showers. Finally, the Cerenkŏv light emitted in the quartz fibers is detected by photomultipliers.

The energy resolution in this region is:

$$\frac{\sigma}{E} \simeq \frac{100\%}{\sqrt{E}} \oplus 5\%.$$

2.2.6 The muon detector

To be in line with the goals of the experiment, an efficient detection of muons is one of the most relevant tasks of CMS. In fact, muons are often indicators of "interesting" physics because they are produced via electroweak interaction, where a W, Z or Higgs is involved, or maybe some new, unknown particle.
The robustness of the CMS muon identification system [43] is provided by two independent measurements of the muon momentum in two different regions of the detector: inside the inner tracking volume and after the coil in the muon system. Since muons have little interaction with matter and they mostly loose energy by ionization in the detector, they are the only charged particles able to cross all the inner detector layers and reach the muon system. For this reason, the relevance of this outer part of the detector is evident: it allows to achieve an efficient muon

identification and an excellent charge determination, to maximize the ϕ acceptance for muons, to improve momentum resolution at high p_T and to have a robust stand-alone muon trigger.

The muon spectrometer exploits three different technologies of gaseous detectors, which are based on the ionization electrons produced by the passage of charged particle in the gas: Drift Tubes (DT) in the central region $|\eta| < 1.2$ and Cathode Strip Chambers (CSC) in the endcap region $0.9 < |\eta| < 2.4$, complemented by Resistive Plate Chambers (RPC) covering up to $|\eta| < 1.6$ to ensure redundancy and improve trigger capabilities. Figure 2.11 shows how the chambers are assembled: in the Muon Barrel (MB) there are four stations of DT and RPC, divided into five wheels along the z-axis, and in the Muon Endcap (ME) CSC and RPC are organized in four disks transverse to the beam axis.

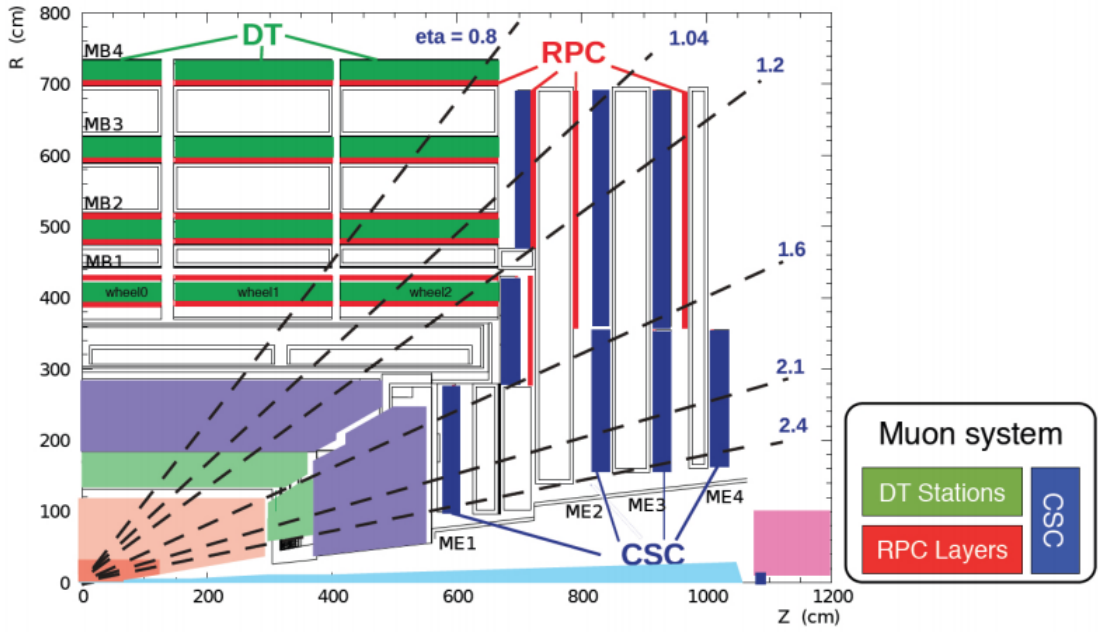

Figure 2.11: Longitudinal view of one quarter of the muon spectrometer.

Drift Tubes

DT are tracking detectors with trigger capabilities which cover the muon spectrometer barrel. The full DT system consists of 250 rectangular chambers (2×2.5 m^2) divided into five wheels along z and arranged in groups of four stations. Each wheel is divided into twelve sectors in ϕ and each sector covers $\sim 30°$ (Figure 2.12).
Each chamber is composed of three superlayers (SL) and each SL consists of four layers of drift cells, as shown in Figure 2.13: two SL have wires parallel to beam axis, which provide a measurement of the perpendicular coordinate in $R - \phi$, and the other one has wires normal to beam axis and measures the coordinate along the

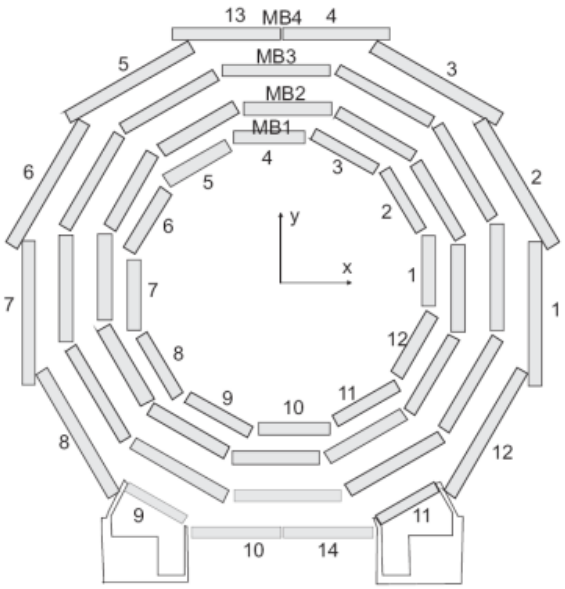

Figure 2.12: Transversal view of the CMS DT system.

direction parallel to the beam ($R - z$ plane). A cell is a rectangular drift tube (4.2 $\times$ 1.3 cm^2) composed of an anode wire and two cathode strips, filled with a mixture of 85% – 15% Ar-CO_2.

A layout with layers non aligned with each other but offset by half a cell width leads to an excellent time resolution, lower than 3 ns, and to an efficiency of 99.8%. It measures muon positions giving two spatial coordinates, with a precision of 100 μm in the $R - \phi$ plane and better than 1 mrad in the θ-direction.

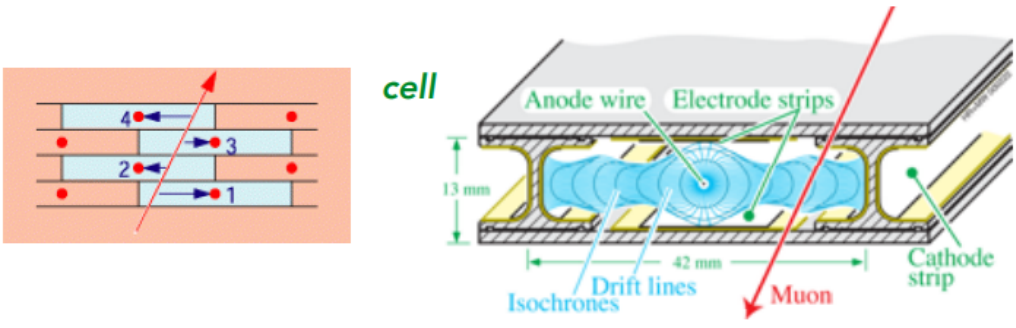

Figure 2.13: A scheme of the staggered four layers of DT cells in a SL (left) and section of a DT cell (right).

Cathode Strip Chambers

CSC are gaseous ionization detectors characterized by a short drift length which are employed in the endcap region to cope with high particle rates and a non-uniform magnetic field. In each endcap, trapezoidal detector chambers are organized into four stations supported by three vertical steel disks (468 chambers in total).
These chambers are Multiwire Proportional Chambers (MWPC) working in avalanche mode with a finely segmented cathode strip readout: strips measure $R - \phi$ while wires give a radial measurement. They consist of arrays of positively-charged anode wires crossed perpendicularly with negatively-charged copper cathode strips within a gas volume; when a muon crosses the cell, it ionizes the gas producing some charge; the charge then drifts toward the wire and gets multiplied, inducing a charge pulse in the strips. A mixture of Ar (40%), CO_2 (50%) and CF_4 (10%) is used [44].
In this way, two position coordinates for each passing particle are obtained. Together with a good spatial resolution (50-150 μm), a precise time information of about 3 ns is achieved.

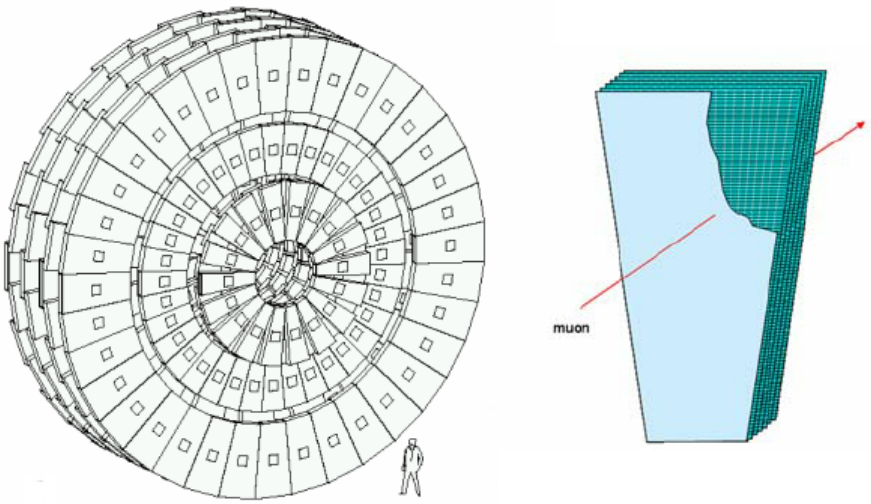

Figure 2.14: Layout of the CSC subsystem (left) and a schematic view of a CSC (right).

Resistive Plates Chambers

RPC are fast gaseous detectors coupled to DT and CSC to provide a parallel muon trigger system. As shown in Figure 2.15, they consist of double-gap chambers made of a high resistivity plastic material operated with a mixture of $C_2H_2F_4$ (96.2%), i-C_4H_{10} (3.5%) and SF_6 (0.3%) humidified at about 40% [45]. Four planes, two positively-charged anodes and two negatively-charged cathodes, are alternated to form two thick gas gap of 2 mm used in avalanche mode to cope with higher rates

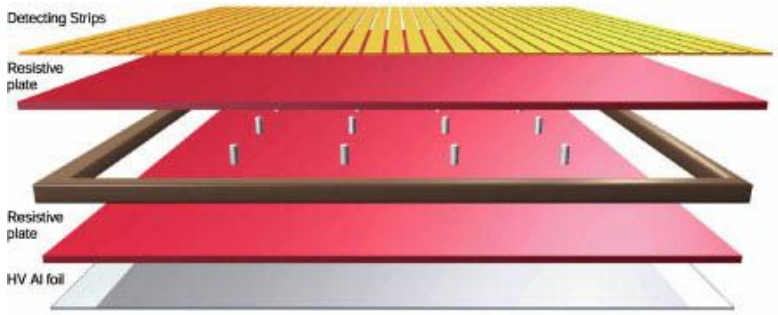

Figure 2.15: Schematic view of a RPC.

of particles. The plates and the electrodes are made of bakelite and graphite respectively, while the central region has rectangular aluminium strips which collect the signal produced when the particle passes.

RPC combine a good time resolution of about 2 ns with a spatial resolution of about 1 cm, depending on the strip width, cluster size and detector alignment. Moreover, they provide timing information for the muon trigger with a fast response and have an average detector efficiency of 95%. Matching track segments in DT and CSC chambers to any RPC cluster provides a measurement both for the efficiency and for the spatial resolution.

2.2.7 The trigger and the Data Acquisition system

The CMS performance at its peak of integrated luminosity implies a total event rate of a GHz, where about one billion p-p interactions take place every second. Hence, it is crucial to select only the potentially interesting events among all physical interactions and reduce the rate to just a few hundred events per second using an effective trigger strategy [46, 47].
Considering the high frequency of bunch crossing, a system able to select or reject events in a very short time (25 ns) is needed. However, it is impossible to collect all the information coming from the subdetectors and to process them at the same time. For this reason, a multilevel architecture has been designed to realize the trigger.
The CMS experiment uses a two-level trigger system:

- **L1 Trigger (L1T)** is implemented in hardware and is based on dedicated fast electronics. It automatically performs a rough reconstruction from the calorimeter system or the muon detector information in order to select or reject events. Starting from a set of objects such as photons, electrons, muons and jets, it provides a rejection factor of 10^4, selecting 100 events per second. They are delivered to the Data Acquisition System (DAQ), which reads data from various subsystems for offline storage, as shown in Figure 2.16. The flow of event data is controlled by an event manager system.

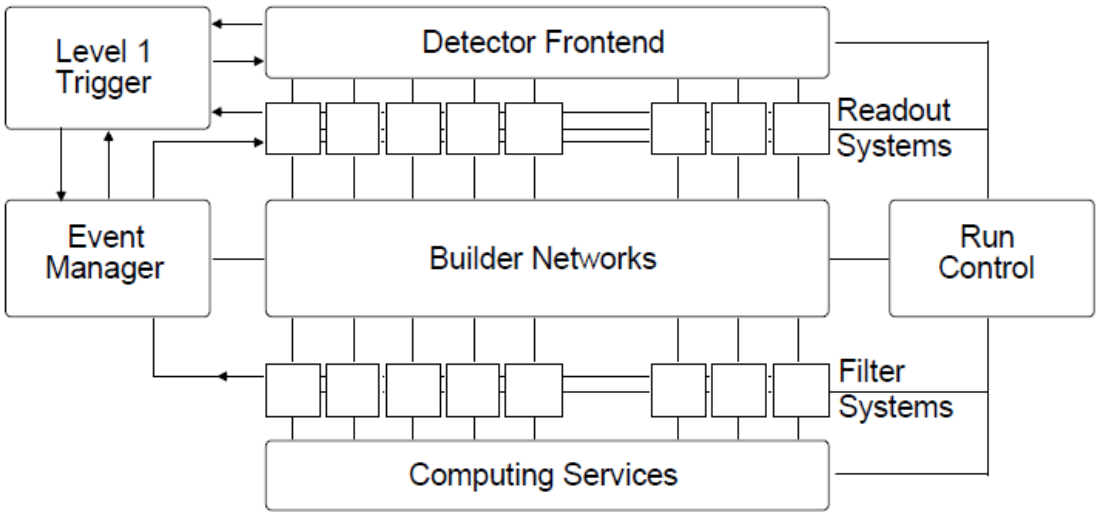

Figure 2.16: The design of the CMS Data Acquisition system.

- **High Level Trigger (HLT)** is a software system which consists of a computer farm of more than 1000 standard computers running the same software framework used for the offline analysis. Here the full information from many interactions is assimilated and synchronized to recreate the entire event using a complex analysis.
  It reduces the amount of data to be stored for the offline analysis and further processed to about 100 Hz, the limit imposed by the storage system. A reduction factor of about 10^3 is achieved in this final step.

2.3 The upgrade of the CMS detector

The LHC has exceeded the designed instantaneous luminosity of 10^{34} $\mathrm{cm}^{-2}\mathrm{s}^{-1}$ (as seen in Figure 2.17), resulting in dynamic inefficiencies and dead time caused by a limited size of the readout bandwidth. This affects detector performance for instantaneous luminosity above 1.6×10^{34} $\mathrm{cm}^{-2}\mathrm{s}^{-1}$.
Hence there are many technical and physics motivations for the CMS detector upgrade. The design of the CMS detector upgrade aims at coping with the very challenging beam conditions of the High Luminosity LHC (HL-LHC), the last phase of the LHC program, when the accelerator will operate at a higher instantaneous luminosity and center-of-mass energy of 14 TeV.
Detector resolutions as well as reconstruction and identification efficiencies are required to maintain the sensitivity of the actual analyses.

The CMS detector upgrade is organized in two different stages:

- Phase-1 upgrade [48, 49], which will take place from 2019 to 2020 during the second Long Shutdown (LS2);

- Phase-2 upgrade [51, 52], which indicates the improvements and upgrades of most of the CMS sub-detectors necessary to fully exploit the luminosity at the end of LHC's operation, earmarked for the period 2024 - 2026.

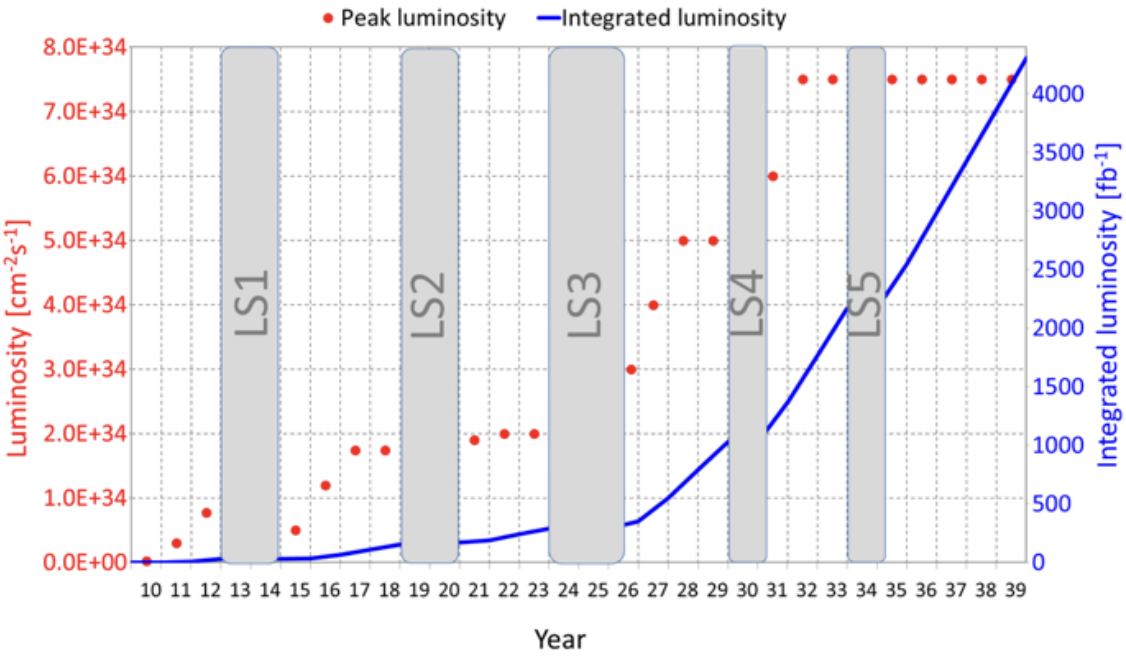

Figure 2.17: The outline LHC schedule and the luminosity evolution.

2.3.1 The HL-LHC goals

In order to allow the detectors to record events efficiently the HL-LHC will be operated in luminosity-levelled mode, with a maximum instantaneous luminosity delivered to the experiments of about $\mathcal{L} = 5 \times 10^{34}$ cm^{-2}s^{-1} (Figure 2.17).
On one hand, this will provide, in a ten year operating time, 3000 fb^{-1} of integrated luminosity: this enormous amount of data collected at $\sqrt{s} = 14$ TeV will allow to investigate the Higgs sector and check the SM predictions in search of any deviation, exploring the TeV scale in great detail. On the other hand, the high instantaneous luminosity will come at the price of an extremely high pile-up (PU), up to 200 overlapping events, for a bunch-crossing interval of 25 ns.

"*These will be years of tremendous opportunities and tremendous challenges. [...] It will be enormously exciting to see what nature has in store for us.*"
(J. Butler - CMS spokesperson, 2016)

The goal of the experimental research at the LHC actually is measuring as accurately as possible well-known particles and Higgs boson properties. At the same time, looking for completely new, unpredicted phenomena is of great interest to the CERN scientific program. In fact, the LHC will help to inquire the most fundamental unsolved questions in particle physics, both theoretical and experimental, for example:

- The mystery of the **baryon asymmetry** in our Universe: cosmological and astrophysical observations have revealed that the known universe is made only of matter, but the same amount of matter and antimatter is expected. Moreover, all of the visible matter accounts for only 4% of the Universe;
- the nature of **dark matter**: the search is open for particles that could make up dark matter (23%) and phenomena responsible for dark energy (73%). The neutral lightest supersymmetric particle is one of the main candidates for dark matter;
- fundamental forces and **gauge coupling unification**;
- **QCD behaviour** under extreme conditions;
- the origin of elementary particle masses and the **hierarchy or naturalness problems**.

2.3.2 Phase-1 detector upgrade

The CMS Collaboration has planned to realize specific changes by the end of LS2 to allow an optimized data taking during the LHC Run-3 operation years (2021 - 2023). The subdetectors mostly involved in the Phase-1 upgrade are:

The muon system In order to improve the trigger on muons with high transverse momenta and to cope with the impact of peak instantaneous luminosity on the muon trigger, the CSC and RPC upgrade is planned.
A fourth layer of CSC (ME4/2) and of RPC chambers will be added to extend detector coverage and preserve a low p_T threshold for the L1 Muon Trigger at high luminosity. Multi-Pattern Gas Detector (MPGD) technologies can ensure an efficient handling of high rate in this endcap region. Moreover, one super-chamber made of two back to back triple-GEM (*Gas Electron Multiplier*) detectors [50], called GE1/1, will be installed in the small angle region close to the beam axis (see Figure 2.18) to guarantee high trigger performance in a very challenging pile-up environment.

The tracking detector The outer microstrip tracker will remain the same while the pixel detector will be replaced to reduce data losses, using less material budget –a lighter material has been chosen- and a more efficient cooling system. There will

be one additional barrel layer and forward disk providing a higher rate capability and a greater number of readout channels: consequently, the inner most layer and the outer one will be moved closer to and further from the IP respectively, while the service electronics will be moved further away from the IP.

The HCAL A depth segmentation will be implemented to obtain higher granularity, hence better energy and position resolution, both in the barrel and endcap region. In addition, the photodetectors will be replaced with improved Silicon Photomultipliers (SiPM), characterized by compact size and immunity to magnetic fields, in order to improve the performance in higher luminosities. Higher gain and better quantum efficiency will allow to perform timing studies to improve pile-up subtraction and background rejection and, as a consequence, the signal over background ratio.
The photomultipliers (PMTs) of the Forward Hadron Calorimeter will be replaced with new photomultipliers that have thinner glass windows and metal envelopes to reduce the amount of Cherenkov light generated by charged particles passing through the glass. The replacement of the PMTs with more radiation tolerant PMTs and the improvement of the calibration and monitoring systems are also planned.

The trigger The Global Trigger in CMS relies on the information from the three muon subsystems and the Global Calorimeter Trigger. The aim of the upgrade is to maintain the same basic categories of functions implementing more algorithms, able to combine trigger objects and technical triggers with a larger variety. Regarding the calorimeter trigger, improved algorithm including event by event pile-up corrections will be implemented, while the muon trigger will be upgraded using custom-designed Advanced Mezzanine Card (AMC) boards, with more powerful Field Programmable Gate Arrays (FPGAs) and larger memories.

2.3.3 Phase-2 detector upgrade

In 2026 CMS must be ready to operate in the very challenging beam conditions expected for the HL-LHC: during LS3, the accelerator will be upgraded and the experiment will also undergo consistent changes and specific upgrades, especially required in the forward region of the detector to maximize the physics acceptance over the largest solid angle possible and to cope with the extremely high PU (up to 200 overlapping events for a bunch crossing interval of 25 ns). The extension of CMS sub-detectors will also allow to improve measurements of total energy and missing energy and b-tagging acceptance. Moreover, the optimization of new components to the HL-LHC environment and the replacement of some detector components which suffer from radiation damage will be necessary.
After these general considerations, let see the main elements of the Phase-2 CMS detector upgrade.

The tracker The current tracker will be affected by a significant radiation damage by LS3 and must be completely replaced for Phase-2 with more radiation tolerant and high granularity detectors.
The granularity of both the outer tracker and the pixel detector will be increased to maintain adequate track reconstruction performance and enable the determination of the primary vertex for all charged particles: in fact, pile-up mitigation in CMS strongly relies upon PF event reconstruction.
To cope with the occupancies, it is important to use less material. The tracker acceptance will be extended up to $|\eta| = 4.0$ to mitigate PU effects in jet identification and energy measurement, using in the outer tracker two types of modules –strip strip (2S) and strip macro-pixel (PS)- and an innovative tilted geometry in the inner barrel. In the inner tracker, two types of hybrid pixel modules (1×2-chips and 2×2-chips) will be used. This extended configuration will guarantee significant acceptance gain for multi-muon final states (as shown in [52]) and also cover the peak production region of jets accompanying Vector Boson Fusion (VBF) and Vector Boson Scattering (VBS) processes, which are considered as significant priorities of the physics program.

The HGCAL A relevant radiation damage will also affect the endcap calorimeters (both ECAL and HCAL) by LS3; in addition, endcaps will suffer large light losses. Hence, they will be replaced by a more radiation tolerant and higher granularity new sampling calorimeter referred to as *High Granularity Calorimeter* (HGCAL) [53], with a coverage up to $|\eta| \sim 3.0$.
It will be characterized by improved energy resolutions for single particles in very dense jets and unprecedented in-time event pile-up, allowing to "visualize" energy flow through fine granularity and optimized longitudinal segmentation and to investigate fast-timing. In this way, the fine structure of showers will be better measured, enhancing particle ID, energy resolution and PU rejection.

The muon system In order to perform high quality Phase-2 physics studies it is important to enhance L1 muon trigger, maintaining p_T thresholds to not loose important events containing Higgs boson, electroweak bosons or top-quark decays. Three main types of muon upgrades have been proposed for Phase-2, regarding the existing muon detectors and associated electronics, new muon detectors in the forward region to increase redundancy and new GEM technology chambers to increase the coverage for muon detection behind the new endcap calorimeters (Figure 2.18).

The forward region $1.6 < |\eta| < 2.4$, equipped with four stations of CSC, is the only part of the muon system which lacks redundant coverage. However, this is a challenging region for muons in terms of momentum resolution, so that the introduction of three additional stations is planned: two RPC with lower granularity, low resistivity and good timing resolution will be added to mitigate background effects and to ensure redundancy in the forward region; one GEM detector (so-called

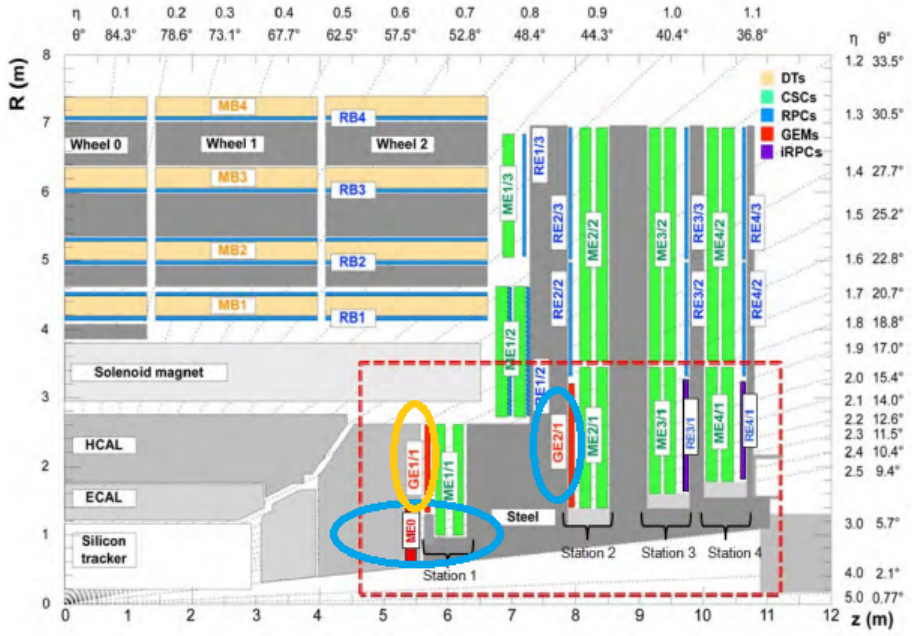

Figure 2.18: A quadrant of the muon system which shows in red the locations of Phase-2 forward muon detectors (GE1/1, GE2/1 and ME0) and in violet the Phase-1 improved RPC stations (RE3/1 and RE4/1).

GE2/1), similar to Phase-1 GE1/1, will be placed in the region $1.55 < |\eta| < 2.45$ with a high magnetic field, where the bending angles are largest and thus momentum determination most effective. The goal of these GEM chambers is to improve the momentum resolution for the standalone muon trigger as well as the matching with tracks in the global muon trigger.
Moreover, the CMS Collaboration has proposed the implementation of a GEM station, ME0 (*Muon Endcap 0*), in the space that becomes free behind the HGCAL and in front of existing ME1, in order to complete the muon coverage up to a pseudorapidity of 2.8 and to exploit efficiently the pixel tracking coverage extension. The extension of the muon detector, that is one of the central topic of this thesis and of the recent TDR, would imply an increased acceptance for all final states including muons and a better rejection of backgrounds where a good identification of muons is relevant.

The trigger The adaptation of the trigger rate capabilities and of the band-width will be necessary because of the increased need to cope with larger event rates and to read out efficiently all the significant information. Two main changes will concern the trigger to make the L1 Trigger efficient for the future physics goals: the rate will be increased from 100 kHz to 750 kHz and the latency for its decision will be modified from 3.4 μs to 12.5 μs.

Chapter 3

Monte Carlo samples

The upgrade physics performance studies are based on the Monte Carlo (MC) simulation samples for the signal and the relevant background processes in order to optimize the signal selection and estimate the background contribution assuming an upgraded CMS detector (see section 2.3).

3.1 Simulation

Considering the high complexity of the detectors and of the physics phenomena at high center-of-mass energies, to simulate events in a realistic way the whole simulation process is divided into different steps so that each level of simulation could be managed as accurately as possible:

1. event generation,
2. parton shower and hadronization,
3. simulation of the detector.

Monte Carlo samples used in these studies have been produced interfacing PYTHIA8 [54] (step 2) with different event generators (step 1) and processing them through a full simulation of the CMS detector based on GEANT4 [64, 65, 66] (step 3).

3.1.1 Event generation

Signal The Higgs boson signal events have been generated at next-to-leading (NLO) order in perturbative QCD (pQCD) with POWHEG2.0 [55, 56, 57] generator, for the main theoretical production modes: gluon-gluon fusion, vector boson fusion, $t\bar{t}H$ and WH/ZH. For WH/ZH the MINLO HVJ [58] extension of POWHEG2.0 is used.
For a Higgs mass of $m_H = 125$ GeV and a center-of-mass energy of 14 TeV, the

predicted cross-section for the dominant gluon-gluon fusion production mode, calculated at the NNLO + NNLL, is [59]:

$$\sigma = 49.68\,\text{pb}^{+3.76\text{pb}}_{-4.02\text{pb}}\ (\text{theory})\ \pm 1.54\,\text{pb}\ (3.10\%)\ (\text{PDF} + \alpha_s).$$

In this thesis, the main channel of interest, presented in section 1.3.4, is

$$gg \to H \to ZZ^* \to 4\mu,$$

characterized by a cross-section given by

$$\sigma(gg \to H) \times \text{BR}\ (H \to ZZ^* \to 4\mu) = 1.47 \times 10^{-3}\,\text{pb}, \tag{3.1}$$

considering the BR presented in Table 3.1 [59]:

BR $(H \to ZZ)$	2.619×10^{-2}
BR $(Z \to \mu^+\mu^-)$	3.366×10^{-2}
BR $(H \to 4\mu)$	2.967×10^{-5}

Table 3.1: The BR related to the process under analysis.

The cross-sections of the other SM Higgs boson production modes, presented in Table 3.2, are significantly smaller[1]:

VBF	$\sigma = 4.278^{+0.021}_{-0.013}$ (theory) ± 0.090 (2.1%) (PDF + α_s)
ZH	$\sigma = 0.986^{+0.038}_{-0.033}$ (theory) ± 0.016 (1.6%) (PDF + α_s)
W^+H	$\sigma = 0.922^{+0.004}_{-0.006}$ (theory) ± 0.017 (1.8%) (PDF + α_s)
W^-H	$\sigma = 0.591^{+0.002}_{-0.004}$ (theory) ± 0.011 (1.8%) (PDF + α_s)
$t\bar{t}H$	$\sigma = 0.614^{+0.037}_{-0.057}$ (theory) ± 0.022 (3.5%) (PDF + α_s)

Table 3.2: The SM Higgs boson production cross-sections (in pb) at 14 TeV for $m_H = 125$ GeV.

The default parton distribution function (PDF) $NNPDF30\_nlo\_as\_0118$ [60] has been used in all simulations. The decay of the Higgs boson to four leptons is modelled with JHUGEN [61, 62].

Irreducible background The so-called irreducible background to the Higgs boson signal comes from ZZ pair produced via $q\bar{q}$ annihilation or gluon-gluon fusion which decays to four muons. The ZZ background contribution is generated at NLO pQCD with POWHEG2.0.
This sample includes also a negligible contribution from $Z\gamma^*$ events.

[1]The cross-section of the $H \to ZZ^* \to 4\mu$ process is obtained by multiplying for the BR given above.

Reducible background The main reducible background comes from Drell-Yan (DY) processes with associated jets and $t\bar{t}$ events and are generated with Madgraph [63] and POWHEG2.0, respectively. The former occurs when a quark-antiquark annihilation creates a virtual photon or Z boson which decays into two muons, accompanied by two jets (principally c-jets and b-jets), which can contain a real muon surrounded by a significant activity. The latter is characterized by two top quarks which decay into a W boson ($W \rightarrow l\nu$) and a b-quark each, producing a possible final state with two clean muons and two b-jets including a real muon each. In both cases, two additional muons included within jets can produce a four-muons final state.

In addition to signal and background samples, for the detailed studies of the muon isolation variable, QCD samples enriched with muons with p_T larger than 15 GeV are produced with PYTHIA8.

To simulate the fragmentation and hadronization effects, all signal and background generators are finally interfaced with PYTHIA8, which is a tool for the generation of high-energy collisions and contains a set of physics models to simulate parton showers, multiparton interactions, beam remnants, fragmentation, particle decays and hadronization and finally produce the complex multihadronic final states.

3.1.2 Full simulation

The detector geometry and data taking conditions assumed in this study correspond to those proposed for the HL-LHC. Full Simulation samples with pile-up 0 and pile-up 200 processed through a detailed simulation of the CMS detector based on the full simulation toolkit GEANT4 are used for this analysis; the generated events are reconstructed with the same algorithms applied for the real data reconstruction. To produce the samples, the CMSSW_9_1_1_patch1 release has been used in the PhaseIITDRSpring17MiniAOD campaign[2].
The geometry used is Extended2023D4 and the global tag, which consists of all the information about the configuration (such as alignment and calibration) to define the offline conditions data, is 91X_upgrade2023_realistic_v3.

GEANT4

GEANT, which stands for *Geometry and tracking*, is a C++ based detector simulation toolkit characterized by a modular architecture and an object-oriented technology. A large variety of application domains exploits its functionality: from high energy physics and astrophysics to space engineering and medical physics.
It simulates the passage of particle through a general detector, taking into account

[2]The terminology of these lines represents very technical definitions that we use for the official CMS simulation samples production.

its geometric shapes and the materials used in its construction (for example, Figure 3.1 shows the CMS detector layout produced with GEANT4) and describing its sensitive regions, the readout schemes and how the information is stored. Moreover, it provides physics models able to describe in a realistic way all the physics processes (electromagnetic, hadronic and optical processes) which take place during the propagation of particles with matter.

The process followed by the software evolves in three main steps and is controlled by the *Run Manager* module:

1. it performs the geometry description and the construction of the detector, assembling some pre-programmed shapes in a hierarchy of volumes;

2. it creates the physics processes simulating the production of the primary vertex and the particle propagation through any geometrical arrangement of material and calculating cross-sections;

3. it sets up the run with any additional requirements of the simulation.

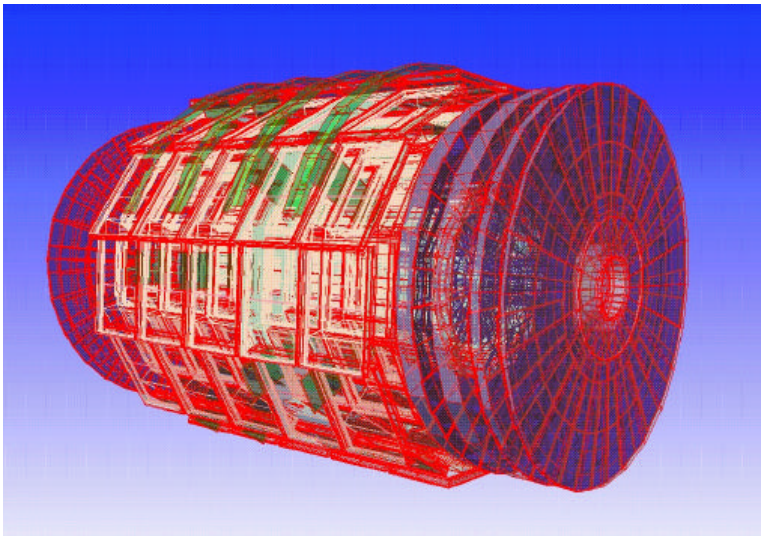

Figure 3.1: The CMS detector layout produced with GEANT4.

CMS SoftWare (CMSSW)

CMSSW [67, 68] is a single software framework used by offline reconstruction, high level trigger and physics analyses to process and analyse data in the CMS experiment.

The overall collection of CMS software is built around a Framework (Figure 3.2), which manages an Event Data Model (EDM), services needed by the simulation

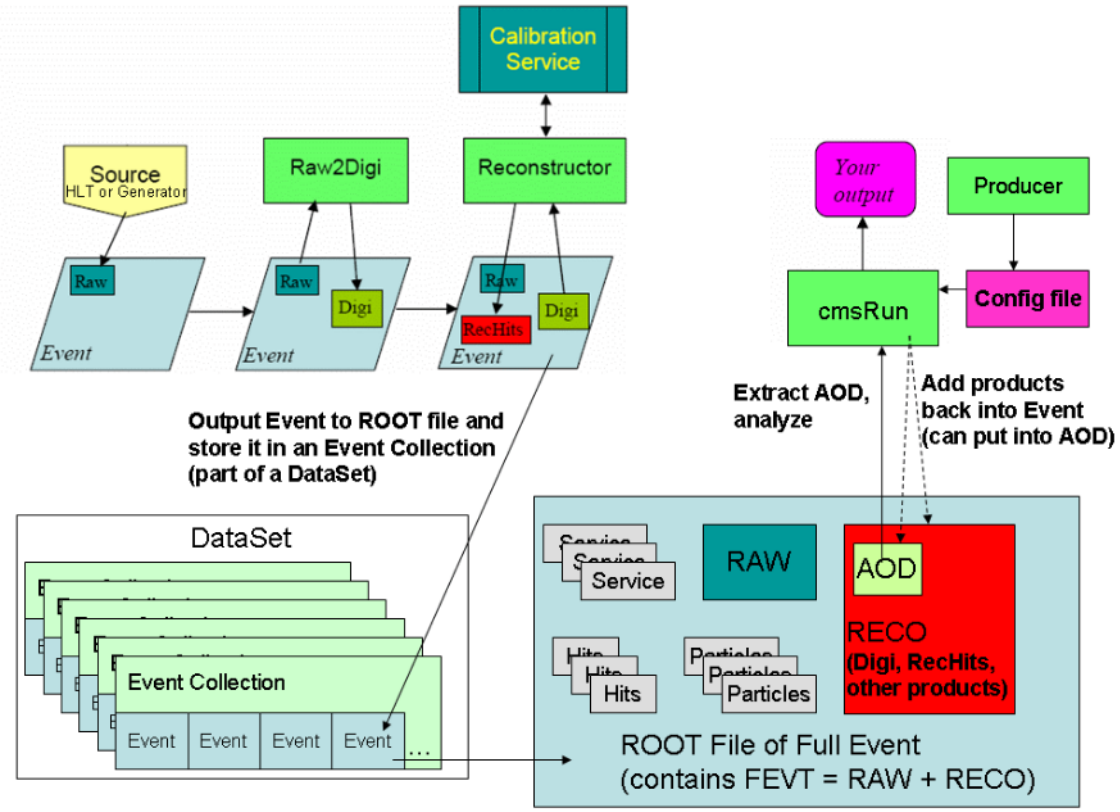

Figure 3.2: The CMS SoftWare framework for the event reconstruction.

and modules which contain all the code needed in the event processing (calibration, alignment, reconstruction algorithms, etc), so that physicists could perform analysis.

The CMSSW event processing model consists of one executable for both detector and Monte Carlo data, called cmsRun, which dynamically load all the required modules at the beginning of the job. It is configured at run time by the user's job-specific configuration file, which gives some inputs to cmsRun, for example:

- which data to use or modules to execute with corresponding parameter settings,
- which order to follow during the execution (path),
- how the events are filtered within each path,
- in which way the path must be connected to the output files.

The main goal of the Framework and EDM is to simplify the development and deployment of reconstruction and analysis software. The CMS Event Data Model (EDM) is developed around the concept of an Event.

Physically, an event is the result of a single readout of the detector electronics and of the signals that have been generated by particles, tracks, energy deposits, present in a number of bunch crossings. In software terms, an Event is a C++ object container where all raw and reconstructed data related to a particular collision are stored as a single entity in memory.
Products in an Event are logically grouped in separate units used to collect particular types of data separately, following these steps, as shown in Figure 3.3:

1. At first, RAW data are stored in containers called edm::Event;

2. as the event data is processed, products are then stored in the Event as reconstructed (RECO) data objects, created by the event reconstruction program. They contain objects from all stages of reconstruction, preserving links to the RAW information: hits in the detector are aggregated in cluster and tracks, which in turn are matched to create particle candidates. RAW and RECO data form the full event data (FEVT).

3. Analysis Object Data (AOD) are derived from the RECO information to provide data for physics analyses in a convenient, compact format. AOD alone contains enough information about the event to allow most kinds of physics analyses, without rerunning the reconstruction process on the data. They include physics objects such as tracks with associated hits, calorimetric clusters with associated hits, vertices, jets and high-level physics objects (electrons, muons, Z boson candidates, and so on).

The Event also contains metadata which describe the configuration of the software used for the reconstruction of each contained data object with information related to conditions and calibration data used for such reconstruction.

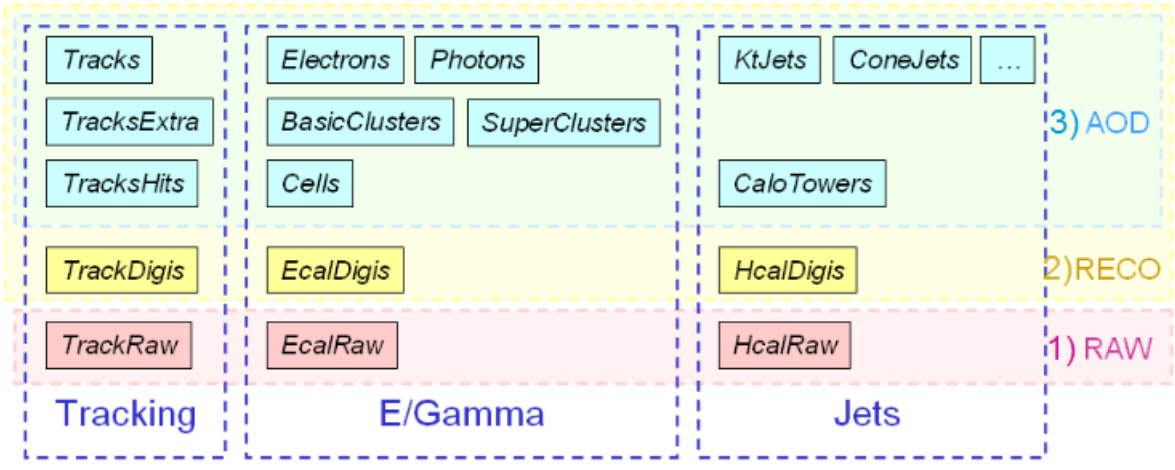

Figure 3.3: Different formats of data provided by CMSSW.

The Event data is output to ROOT files. The event can be analysed with ROOT [69], a modular data analysis software framework which provides all the tools needed to deal with big data processing, statistical analysis, visualisation and storage, and then can be used as a n-tuple for final analysis. When data are processed, they are passed from one module to the next one and then accessed only through the Event. Any C++ class can be placed in an Event without requirement on inheritance from a common base.

I have worked on MINIAODSIM samples (which are MC datasets produced centrally) of signal and background, linked in Table 3.3.

3.2 Reconstruction of physics objects

Efficient particle identification and good event reconstruction are required to guarantee high quality physics analyses. The CMS experiment has developed excellent techniques for the reconstruction and identification of physics objects [70], such as muons, electrons, jets, thanks to the versatility of its apparatus.

3.2.1 ParticleFlow reconstruction

The CMS Particle-Flow (PF) [71, 72, 73] event reconstruction algorithm is used to reconstruct and identify all stable particles produced in a collision with an optimized combination of information from all CMS sub-detectors, determining particle types, their energies and direction. This method has greatly improved the robustness of the object identification techniques against the high event pile-up (PU) and the reconstruction of higher-level objects such as hadronic jets or missing transverse energy.

The basic elements of the particle-flow event reconstruction are the charged particle tracks reconstructed in the central tracker and the energy clusters reconstructed in electromagnetic and hadronic calorimeters. The tracks are reconstructed applying an iterative tracking strategy which provides high efficiency and low fake rate: charged particle hits in the tracking detectors are used to determine their trajectories and to give a measurement of position and momentum. Reconstructed tracks allow to identify the Primary Vertex using the transverse impact parameter and the longitudinal coordinate z.
Starting from these reconstructed objects, particle candidates resulting from the PF algorithm are classified as:

- **electrons**, which are reconstructed using information from the inner tracker and the calorimeters and exploiting shower shapes and ratio of the energy deposited in the hadronic and electronic calorimeters. To reconstruct the trajectories a particular modelling of particle energy loss due to bremsstrahlung radiation within the tracker material and fitted with a Gaussian Sum Filter (GSF) [74] is used;

- **muons**, which are reconstructed by combining information from the silicon tracking and muon chambers independently, using different algorithms to reach a robust and efficient identification. Firstly, tracks are reconstructed independently in the inner-tracker (referred to as tracker track) and in the muon system (*Stand-alone Muon* track). Then these tracks are matched to each other and the hits are combined using a Kalman filter [75] to reconstruct a *Global Muon*. If at least one muon segment matches to the extrapolated track, the corresponding tracker track is considered as a *Tracker Muon*: it is identified by geometrically matching an inner track with segments in the muon chambers. A reconstruction efficiency of about 99% is provided by the high granularity of tracking detectors and high efficiency of the muon system;

- **charged hadrons**, which are reconstructed from the tracks in the central silicon tracker, searching for a match of the extrapolated track to a calorimetric energy cluster;

- **photons and neutral hadrons**, which are reconstructed from energy clusters in calorimeters, searching for clusters separated from the extrapolated position of tracks in the calorimeters.
  In the case of photons, the particle-flow clustering algorithm applies energy thresholds to all ECAL crystals to reduce noise effects; moreover, the isolation requirement is applied to reject PU. If neutral particles overlap with charged particles in the calorimeters, they can be detected as calorimetric excesses of energy with respect to the sum of the associated track momenta.

After reconstructing individual particles, the PF algorithm uses the full event information to refine the reconstruction and provide a coherent event description. These particles are used to calculate, for example, photon isolation or lepton isolation quantities and to build objects of higher complexity such as jets, τ, missing transverse energy.
All particles were clustered into jets with the anti-k_T algorithm [76], with a distance parameter $R = 0.5$: jet momentum and spatial resolution are good, thanks to the excellent ECAL granularity and the high quality of tracking detectors.
The τ lepton, characterized by a very short lifetime, is identified, thanks to its hadronic decays through the reconstruction of the intermediate resonances.
Finally, the missing transverse energy vector is reconstructed as the opposite of the transverse-momentum sum of all final-state particles reconstructed in the detector.

3.2.2 Muon identification

All the muon fits are finally collected into a single Muon object. It is useful to classify each muon according to how it was produced:

- **prompt**, i.e. from the decay of a W, Z or H boson or from a τ lepton produced in the hard proton-proton interaction. They are typically isolated from hadronic activity and come from the main interaction point, presenting hits in all layers of the tracker and in the muon chambers;
- **heavy flavor decay**, i.e. from the decay of a b-quark or c-quark hadron. Hits in all layers of the tracker are still expected;
- **light flavor decay**, i.e. from the decay of a light-quark hadron, such as a pion (π) or a kaon (K). If the decay occurs in the tracker, the track may exhibit a ''kink"[3].
- **fake muons**, such as punch-through (which occurs when jets escape the calorimeter and enter in the first muon station) or matching of random tracks and muon segments. A clear sign that there are not real muons is that they do not present MIP (minimum-ionization particles) deposits in the calorimeter.

Three Muon collections are distinguished on the basis of the typical identification (ID) selections:

Loose muons The candidate is required to be reconstructed either as a Global Muon or as a Tracker Muon: muon candidates which are reconstructed only on the muon detectors (without hits reconstructed on the inner tracking system) are discarded. In addition, the candidate must satisfy the selection criteria of the PF Muon algorithm.

Medium muons These muons are Loose muons with additional track-quality and muon-quality requirements.

Tight muons For this selection, the candidate needs to satisfy the PF muon algorithm selection and must be reconstructed as a Global muon track, with additional muon-quality restrictions related to the number of hits and the Interaction Point. The Tracker Muon algorithm has to match the muon inner track extrapolation to segments in at least two muon stations. Moreover hits on more than five layers of the inner tracking system are required and at least one pixel hit in the silicon tracker layers. Finally cuts on the IP in the transverse and longitudinal planes are applied with respect to the primary vertex of the event: $|Dxy| < 0.2$ cm and $|Dz| < 0.5$ cm.

Among the Run-2 Muon ID selections, another category is defined to take into account the possible extension of the muon system proposed for the Phase-2 Muon

[3]For example, when a pion decays within the tracker, $\pi^+ \to \mu^+ + \nu_\mu$, the curvature of the track changes because of the lower p_T and the presence of an invisible ν_μ.

detector upgrade: the **ME0 muons**.
ME0 selection requires a matching between a tracker track and a ME0 segment in global η and ϕ or in the bending angle (shrinking cut with muon p). The tagged track is a high purity tracker track, with at least one pixel hit in the silicon tracker layers; a cut on the transverse and longitudinal impact parameter with respect to the primary vertex of the event is also applied: $|Dxy|$ <0.2 cm and $|Dz| < 0.5$ cm.

3.2.3 Isolation

Muon isolation is fundamental to distinguish prompt muons from the muons embedded within jets (a simple scheme is shown in Figure 3.4) and is typically calculated by evaluating if the hadronic activity around the muon candidate is significant or not. It is necessary to measure the scalar sum of the transverse momenta of all reconstructed objects in its proximity within a cone of radius $\Delta R = 0.3$ centered on its direction vector, using information from the inner tracker and the transverse energies in calorimeter cells (both in the ECAL and HCAL).

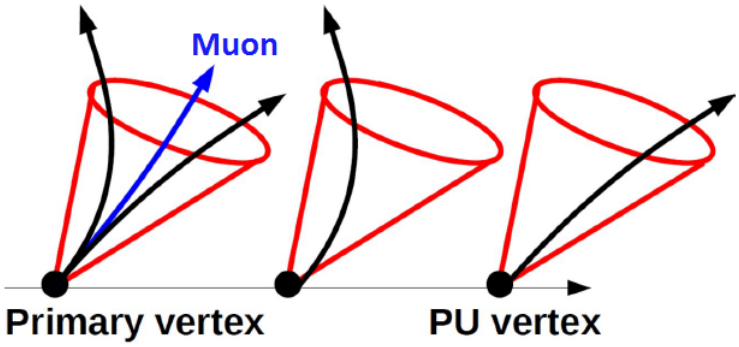

Figure 3.4: The muon isolation is calculated by the measurement of the activity around the particle within a cone of radius $\Delta R = 0.3$. It is also possible to distinguish between charged particle from primary vertex or from PU vertices.

Two different isolation methods to reject the non-prompt muons have been used for the studies of the Phase-1 detector:

- The **track-based isolation** uses only tracks coming from the tracker and originating from the primary vertex and takes the p_T sum of these tracks within a cone size of $\Delta R = 0.3$. The isolation value is then normalized with the muon p_T:

$$I_{track\_ISO} = \frac{\sum p_T^{tracks}}{p_T^{muon}}. \tag{3.2}$$

- The **particle-flow isolation** uses all PF candidates within a cone size (of the muon candidate) of $\Delta R = 0.3$, separating the particle flow objects into

four categories: charged hadrons from the primary vertex, neutral hadrons, photons and PU (charged hadrons not from the primary vertex). Each of the four components are p_T summed and combined using the following equation:

$$I_{PF\_ISO} = \frac{\sum^{ch\_had} p_T + \sum^{neu\_had} E_T + \sum^{\gamma} E_T}{p_T^{muon}}. \tag{3.3}$$

Since charged particles can be identified as originating from a PU vertex (Figure 3.4) but this is impossible for photons and neutral hadrons, a correction called $\Delta\beta$ *correction* is implemented. The idea is to estimate the contribution of PU vertices to photon and neutral isolation by measuring the charged hadrons from PU and scaling them by the expected neutral-to-charged ratio, which is 0.5:

$$I_{PF\_ISO} = \frac{\sum_{NOPU}^{ch\_had} + \max(\sum^{neu\_had} E_T + \sum^{\gamma} E_T - \Delta\beta, 0)}{p_T^{muon}}. \tag{3.4}$$

Since the particle density within the CMS detector will increase significantly because of the overabundance of PU expected at the HL-LHC, the average muon isolation value will become larger, too, representing one of the most relevant challenges for Phase-2 luminosity.

	SAMPLES	Entries
Signal	/GluGluHToZZTo4L_M125_14TeV_powheg2_JHUgenV702_pythia8/ PhaseIITDRSpring17MiniAOD-noPU_91X_upgrade2023_realistic_v3v1/MINIAODSIM	100000
	/GluGluHToZZTo4L_M125_14TeV_powheg2_JHUgenV702_pythia8/ PhaseIITDRSpring17MiniAOD-PU200_91X_upgrade2023_realistic_v3v1/MINIAODSIM	93374
	/ttH_HToZZ_4L_M125_14TeV_powheg2_JHUgenV702_pythia8/ PhaseIITDRSpring17MiniAODnoPU_91X_upgrade2023_realistic_v3v1/MINIAODSIM	4700
	/ttH_HToZZ_4L_M125_14TeV_powheg2_JHUgenV702_pythia8/ PhaseIITDRSpring17MiniAODPU200_91X_upgrade2023_realistic_v3v1/MINIAODSIM	86520
	/WminusH_HToZZTo4L_M125_13TeV_powheg2minloHWJ_JHUgenV702_pythia8/ PhaseIITDRSpring17MiniAODnoPU_91X_upgrade2023_realistic_v3v1/MINIAODSIM	1719
	/WminusH_HToZZTo4L_M125_13TeV_powheg2minloHWJ_JHUgenV702_pythia8/ PhaseIITDRSpring17MiniAODPU200_91X_upgrade2023_realistic_v3v1/MINIAODSIM	723
	/WplusH_HToZZTo4L_M125_13TeV_powheg2minloHWJ_JHUgenV702_pythia8/ PhaseIITDRSpring17MiniAODnoPU_91X_upgrade2023_realistic_v3v1/MINIAODSIM	15078
	/WplusH_HToZZTo4L_M125_13TeV_powheg2minloHWJ_JHUgenV702_pythia8/ PhaseIITDRSpring17MiniAODPU200_91X_upgrade2023_realistic_v3v1/MINIAODSIM	1192
	/ZH_HToZZ_M125_14TeV_powheg2minloHZJ_JHUgenV702_pythia8/ PhaseIITDRSpring17MiniAODnoPU_91X_upgrade2023_realistic_v3v1/MINIAODSIM	16439
	/ZH_HToZZ_M125_14TeV_powheg2minloHZJ_JHUgenV702_pythia8/ PhaseIITDRSpring17MiniAODPU200_91X_upgrade2023_realistic_v3v1/MINIAODSIM	10665
	/VBF_HToZZTo4L_M125_14TeV_powheg2_JHUgenV702_pythia8/ PhaseIITDRSpring17MiniAODnoPU_91X_upgrade2023_realistic_v3v1/MINIAODSIM	50197
	/VBF_HToZZTo4L_M125_14TeV_powheg2_JHUgenV702_pythia8/ PhaseIITDRSpring17MiniAODPU200_91X_upgrade2023_realistic_v3v1/MINIAODSIM	98388
Irreducible background	/ZZTo4L_14TeVpowhegpythia8/ PhaseIITDRSpring17MiniAODnoPU_91X_upgrade2023_realistic_v3v1/MINIAODSIM	99460
	/ZZTo4L_14TeVpowhegpythia8/ PhaseIITDRSpring17MiniAODPU200_91X_upgrade2023_realistic_v3v1/MINIAODSIM	364840
Reducible background	/TTTo2L2Nu_TuneCUETP8M1_14TeVpowhegpythia8/ PhaseIITDRSpring17MiniAODnoPU_91X_upgrade2023_realistic_v3v1/MINIAODSIM	968645
	/TTTo2L2Nu_TuneCUETP8M1_14TeVpowhegpythia8/ PhaseIITDRSpring17MiniAODPU200_91X_upgrade2023_realistic_v3v1/MINIAODSIM	718710
	/DYJetsToLL_M50_TuneCUETP8M1_14TeVmadgraphMLMpythia8/ PhaseIITDRSpring17MiniAODnoPU_91X_upgrade2023_realistic_v3v1/MINIAODSIM	50188
	/DYJetsToLL_M50_TuneCUETP8M1_14TeVmadgraphMLMpythia8/ PhaseIITDRSpring17MiniAODPU200_91X_upgrade2023_realistic_v3v1/MINIAODSIM	3675378
	/QCD_Pt20toInf_MuEnrichedPt15_TuneCUETP8M1_14TeV_pythia8/ PhaseIITDRSpring17MiniAODnoPU_91X_upgrade2023_realistic_v3v1/MINIAODSIM	1838815
	/QCD_Pt20toInf_MuEnrichedPt15_TuneCUETP8M1_14TeV_pythia8/ PhaseIITDRSpring17MiniAODPU200_91X_upgrade2023_realistic_v3v1/MINIAODSIM	2047924

Table 3.3: Signal and background MINIAODSIM samples (for PU 0 and PU 200) with their corresponding number of events.

Chapter 4

$H \to ZZ^* \to 4\mu$ analysis with the CMS Phase-2 muon detector upgrade

The $H \to ZZ^* \to 4\mu$ decay mode has a large signal-to-background fraction due to the possibility of complete reconstruction of the final decay products and to the excellent lepton momentum and hence the invariant mass resolution. As a consequence, this decay channel could be largely studied in the context of the CMS detector upgrade in order to discuss the extension of the muon system in η coverage through the insertion of the ME0 subdetector (see section 2.3), since the detection of four-muon events primarily relies on the muon system.

4.1 Lepton reconstruction and selection

Since the branching ratio of the Higgs decay to four muons is rather low (see Table 3.1), it is fundamental to maintain a very high lepton reconstruction and selection efficiency. For this reason, a careful study of adequate identification (ID) algorithms, isolation and expected backgrounds is needed.

4.1.1 ID algorithm

As explained in section 3.2.2, the muon identification can be performed at three different levels: Loose, Medium and Tight identification. In this thesis, the performance of $H \to ZZ^* \to 4\mu$ analysis is studied by applying the Loose Muon identification criteria, designed to be highly efficient for prompt muons as well as for muons from heavy and light quark decays.
Isolated Loose muons are selected in two different ways depending on their pseudo-rapidity:

- within the geometrical acceptance $|\eta| < 2.4$, Loose muons are requested to have a transverse momentum p_T greater than 5 GeV;
- in the extended high pseudorapidity region $2.4 < |\eta| < 2.8$, Loose muons are required to have a momentum p greater than 5 GeV. A cut on p instead of p_T is applied in order to recover events with muons close to the beam pipe which have a small p_T but comparatively high p, potentially coming from a Z boson decay.

Moreover, in both cases a cut on the longitudinal impact parameter (IP) -computed with respect to the primary vertex (PV)-, $|Dz| < 0.2$, is applied to minimize the probability that a muon comes from a pile-up vertex instead of a primary vertex. Finally, to get rid of background events with muons coming from the PU vertices or from decay of other particles different from a Z boson, the transverse IP, $|Dxy|$, and significance of IP with respect to the PV, defined as

$$IP \text{ significance} = \frac{IP}{\sigma_{IP}}, \tag{4.1}$$

where σ_{IP} is the error on the IP measurment, are required to be lower than 0.5 and 4, respectively.

Figure 4.1 shows the Loose Muon ID efficiency as a function of the muon p_T and η. The efficiency is defined as the number of reconstructed muons divided by the number of generated muons within the acceptance region.
A geometrical matching between the reconstructed muon and the corresponding generator-level muon is performed in the following way:

1. loop over all of the generated muons;
2. loop over all of the reconstructed muons to find which one is closest in ΔR to the generated muon;
3. check whether the distance between the generated muon and the closest reconstructed muon is $\Delta R < 0.2$.

We observe that the reconstruction efficiency of muons with p_T greater than 20 GeV exceeds 90% both for PU 0 and PU 200 scenarios. In addition, the distributions in function of $|\eta|$ show a slightly lower reconstruction efficiency in the forward region with respect to the central region, where it is about 100%.

4.1.2 Isolation

Muon isolation criteria plays an important role in order to suppress $Z+$jets and $t\bar{t}$ backgrounds to a level which allows observation of the Higgs decay into four muons.
In the $H \to ZZ^* \to 4l$ analysis adopted for the study of Run-2 data (2016) [77],

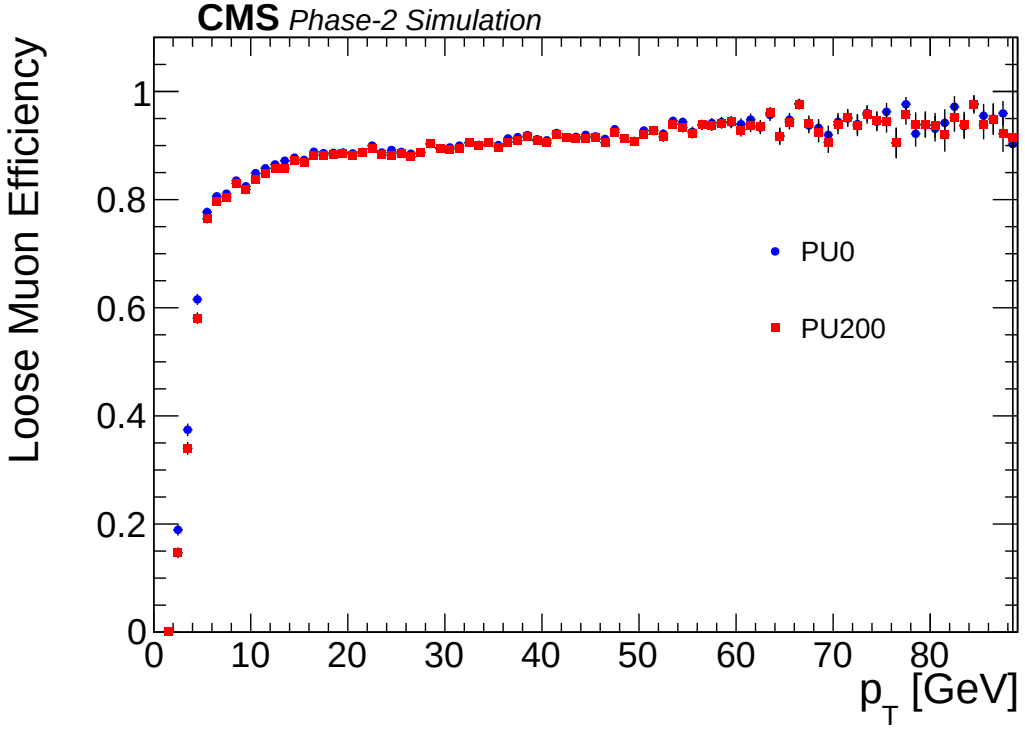

(a)

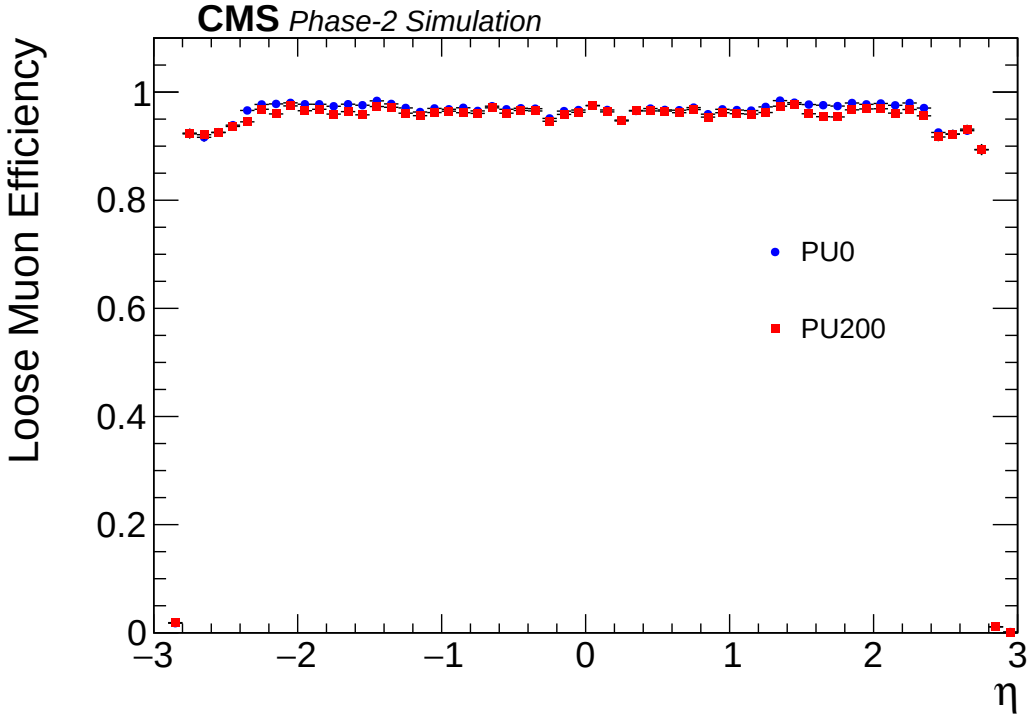

(b)

Figure 4.1: Loose muon reconstruction efficiency as a function of muon (a) p_T and (b) $|\eta|$.

leptons were considered isolated if they were reconstructed with an isolation requirement of $I^{\mu} < 0.35$. The PF algorithm was used to reconstruct leptons and calculate isolation, taking into account only the isolation sums restricted to a cone of angular radius $\Delta R = 0.3$ around the lepton direction at the PV.
However, an increase of PU implies a significantly higher value of the isolation variable due to large number of minimum-bias tracks going into the isolation cone which increases the momentum sum. Hence the isolation needs to be carefully tuned to cope with a high pile-up environment.

For the isolation of individual muons during the upgrade studies the **track-based isolation** is used. It estimates the surrounding activities around a muon by summing up the transverse momenta of all the charged and neutral particles reconstructed within a cone of $\Delta R < 0.4$ around the muon direction using only the information provided by the tracker to compute the momentum. Figures 4.2 and 4.3 show the track-based isolation distributions for the $H \rightarrow 4\mu$ signal and (muon enriched) QCD background for PU 0 and PU 200 separately for $|\eta| < 2.4$ and $2.4 < |\eta| < 2.8$ regions.
The QCD background isolation distribution looks flat in the whole pseudorapidity region both for PU 0 and PU 200. On the other hand, the signal distribution has a peak around zero in the central region $|\eta| < 2.4$ which implies the prompt nature of muons coming from the Higgs decay with very little activities around, while in the forward pseudorapidity region the high pile-up contamination results in larger values of isolation (non-isolated muons).

In order to retain the high signal efficiency and reject background as much as possible (with a discrimination between prompt muons coming from Z boson decay and muons arising from decays of hadron within jets via electroweak interaction), an isolation requirement with optimized cut values (presented in Table 4.1) was imposed.

Track-based Isolation and Loose ID			
PU = 0		PU = 200	
Barrel	Endcap	Barrel	Endcap
0.148	0.108	0.408	0.240
QCD Background (%)			
23.5	25.5	41.4	32.4

Table 4.1: Optimized track-based isolation cut values for Loose muons for PU 0 and PU 200 scenarios and corresponding QCD background contributions.

The isolation cut values for different $|\eta|$ regions and PU scenarios have been

obtained from ROC (*Receiver operating characteristic*) curves comparing the signal[1] selection efficiency and the muon enriched QCD background efficiency. The isolation cut was chosen by requesting that the 90% of signal selection efficiency be retained. Figure 4.4 shows the ROC curves for isolation for PU 0 and PU 200 for the isolation variable running in the range 0 - 10.
The muon isolation efficiency for the two considered regions of pseudorapidity with the implementation of the optimized cut values is shown in Figure 4.5.

4.2 Event selection

The event selection is designed to identify signal candidates from events containing four leptons in the final state. The same analysis used for 2016 Run-2 data [77] has been applied for the event selection in these studies. The events are required to have at least four well-identified and isolated leptons, each originating from a common primary vertex.
At first, the Z boson candidates are formed as pairs of opposite-charge muons ($\mu^+\mu^-$) with the requirement to pass $12 < \mathrm{m}_{\mu^+\mu^-} < 120$ GeV. They are then combined into ZZ candidates: among all muon pairs, the one with the invariant mass closest to the nominal Z boson mass is chosen as the first on-shell Z_1, while among all remaining pairs, the highest p_T one is chosen as the second Z_2.

To be considered for the analysis, ZZ candidates have to pass a set of kinematic requirements that improves the sensitivity to the Higgs boson decay.

1. The Z_1 invariant mass must be larger than 40 GeV.

2. At least two muons are required to have $p_T > 10$ GeV and at least one muon is required to have $p_T > 20$ GeV.

3. All muons must be separated in angular space by at least $\Delta R(l_i, l_j) > 0.02$ in order to suppress contribution from split tracks, where two nearby tracks reconstruct two muons using the same muon track reconstructed in the muon system.

4. The Z_2 invariant mass is required to be $\mathrm{m}_{Z_2} > 12$ GeV to exclude events containing a low-mass dilepton resonance.

5. All the opposite-charge muon pairs are required to satisfy $m_{\mu^+\mu^-} > 4$ GeV aiming to suppress events with muons originating from hadron decays in jet fragmentation or from the decay of low-mass hadronic resonances.

6. Finally, the four-muon invariant mass, m_{4l}, must be larger than 100 GeV.

[1] To perform efficiency and isolation studies the signal samples produced via gluon-gluon fusion only have been used.

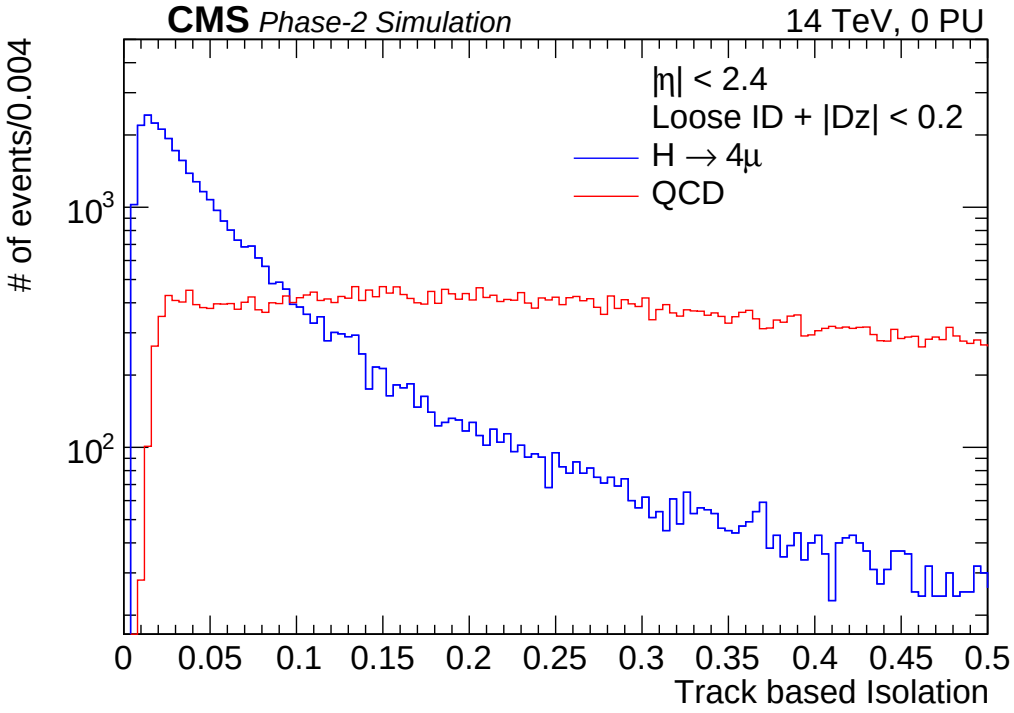

(a)

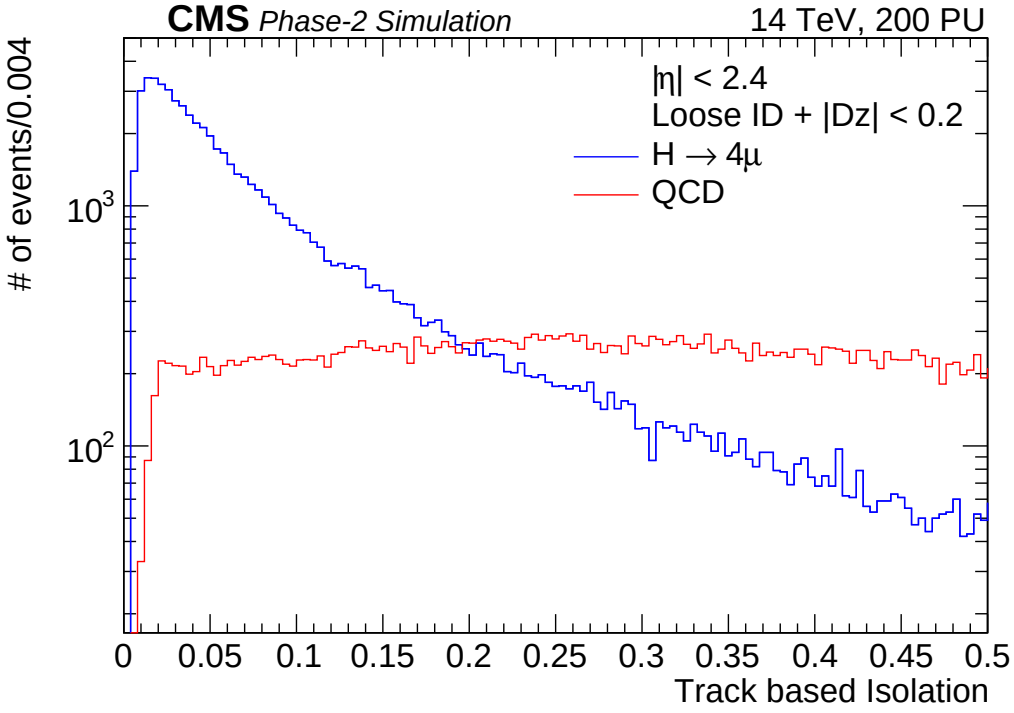

(b)

Figure 4.2: Track-based isolation distributions for $H \to 4\mu$ signal and QCD background for $|\eta| < 2.4$ for PU 0 (a) and PU 200 (b).

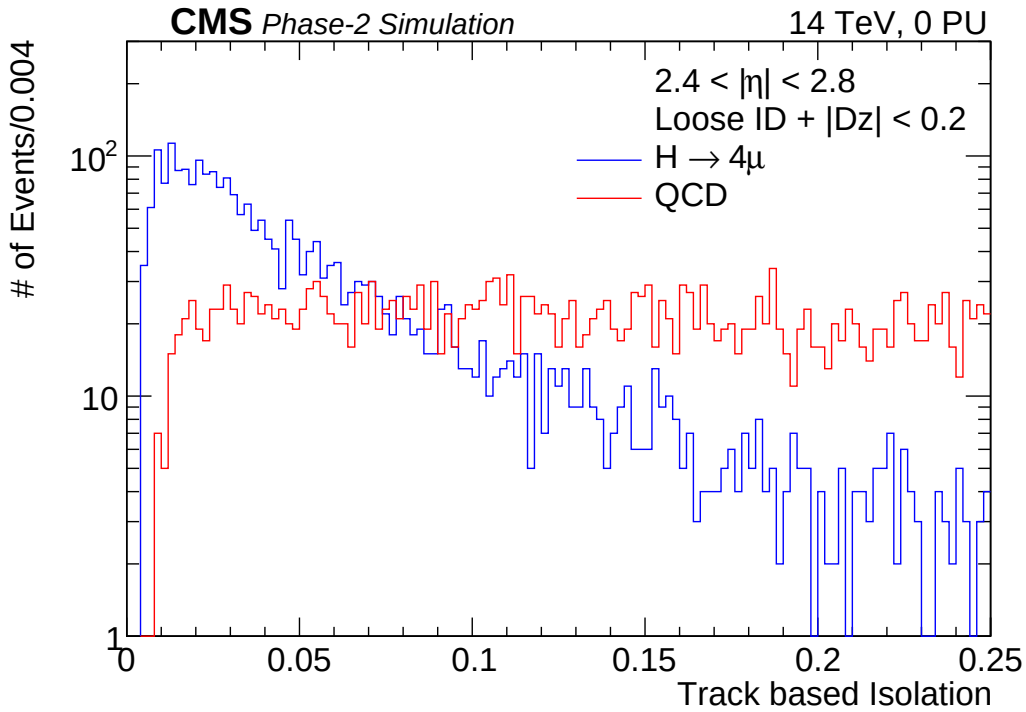

(a)

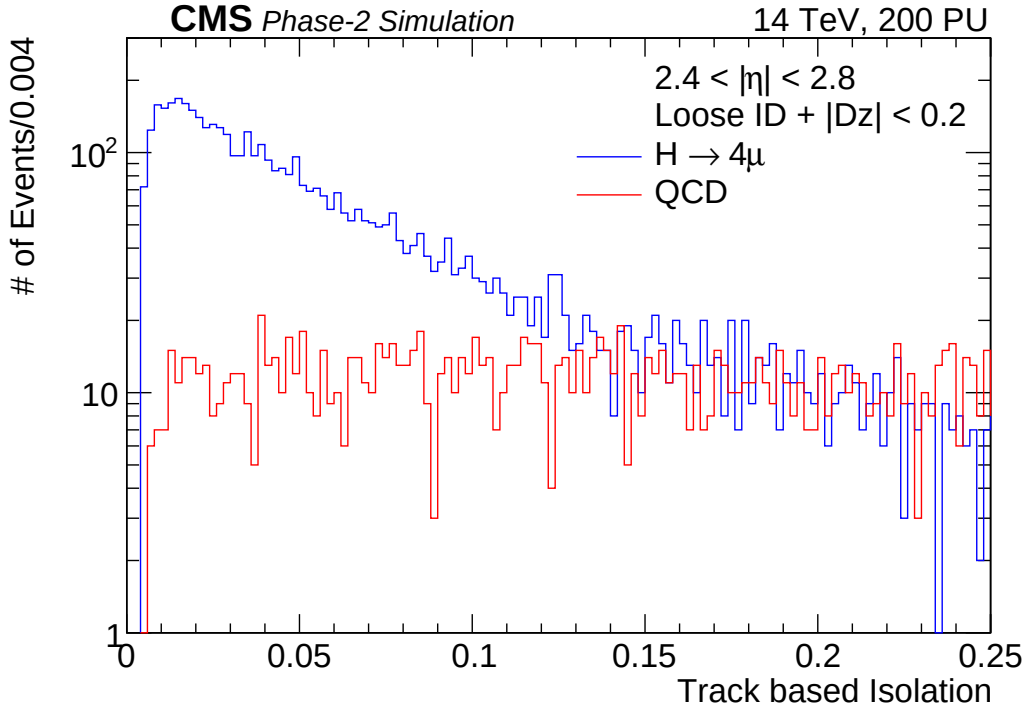

(b)

Figure 4.3: Track-based isolation distributions for $H \to 4\mu$ signal and QCD background for $2.4 < |\eta| < 2.8$ for PU 0 (a) and PU 200 (b).

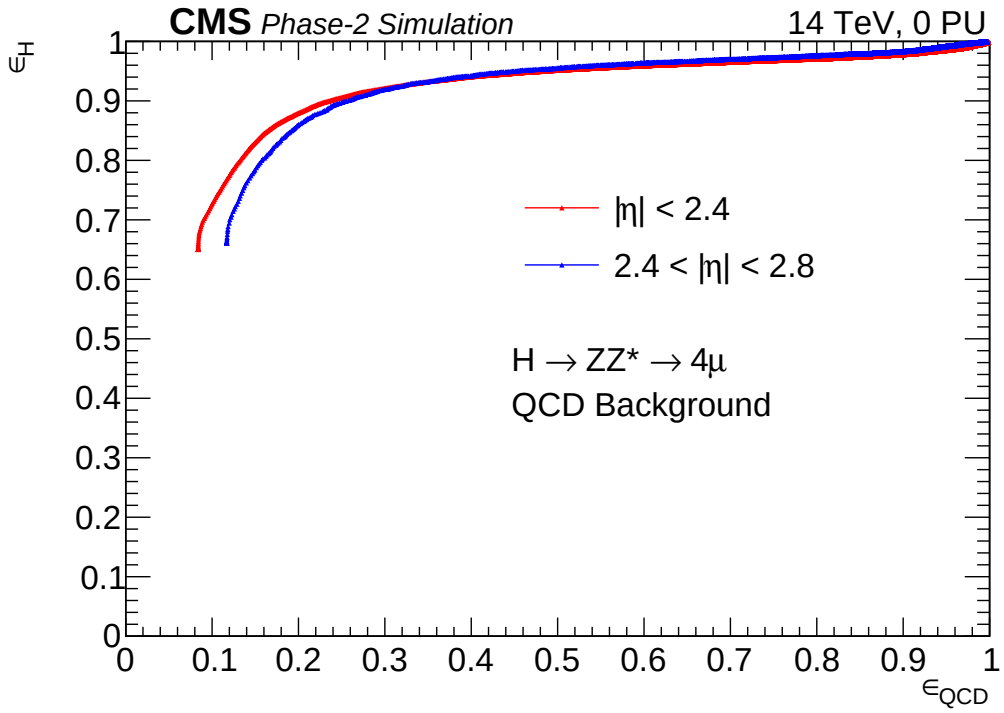

(a)

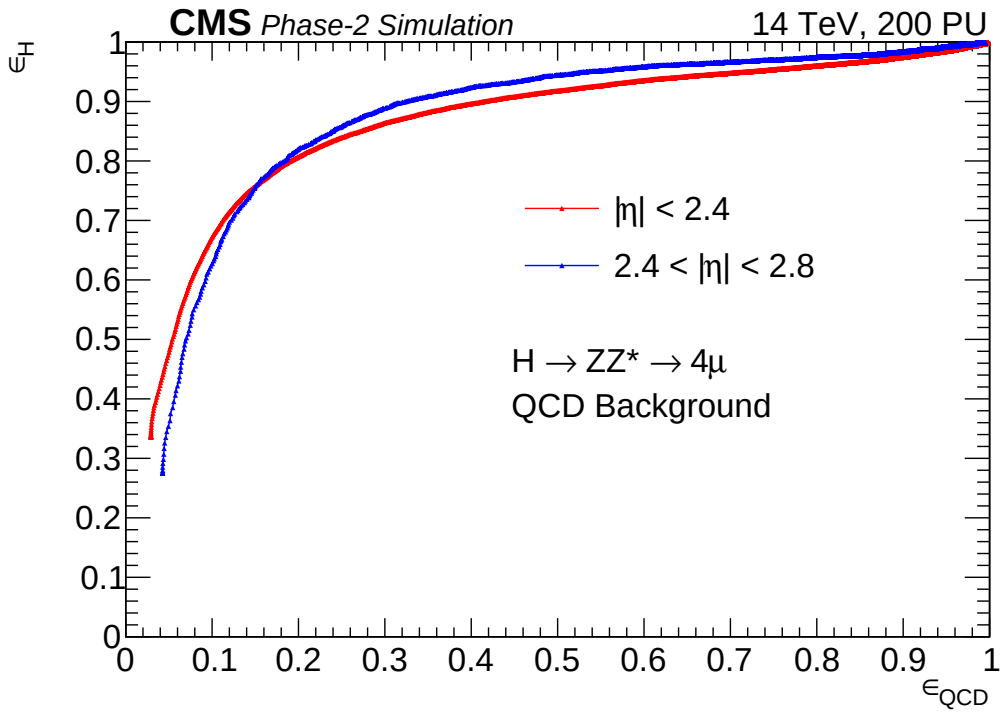

(b)

Figure 4.4: Track-based isolation ROC curves: $H \rightarrow 4\mu$ signal selection efficiency versus QCD background efficiency for PU 0 (a) and PU 200 (b).

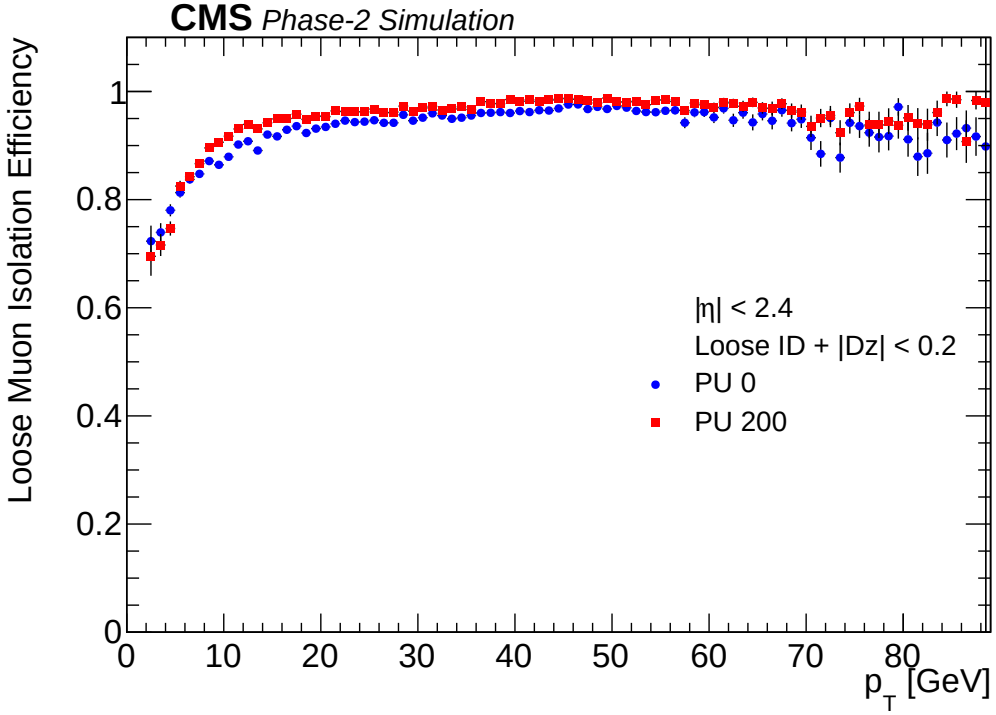

(a)

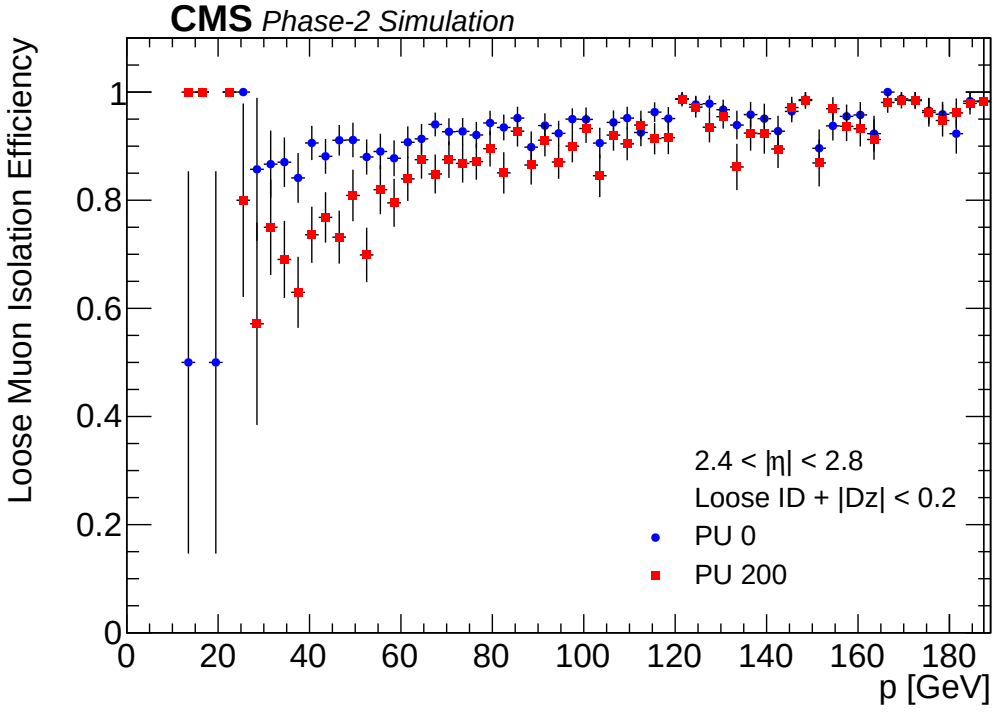

(b)

Figure 4.5: Track-based isolation efficiency with matching at the generator level for $|\eta| < 2.4$ (a) and $2.4 < |\eta| < 2.8$ (b).

At the end the Higgs boson is reconstructed with the four leptons used to reconstruct Z_1 and Z_2.

4.3 Background estimation

A careful study of all the background sources is necessary to evaluate whether background could be maintained under control effectively allowing a clear observation of the signal[2] in the challenging conditions foreseen for the HL-LHC.

Firstly, to evaluate the irreducible background contribution to the four muon invariant mass spectrum, the same analysis presented above has been applied to a sample of resonant $ZZ \to 4\mu$ events that present the same final state as the signal events with four prompt muons. The estimated ZZ background yield is given in Table 4.3.

Dealing with the reducible background is more complex. The reducible background is mainly composed of $Z+$jets (the dominant contribution) and $t\bar{t}$ events where the Z boson or $t\bar{t}$ pair decays into two leptons and the jets are falsely identified as prompt muons passing the entire selection chain, hereafter referred to as *fake muons*.
The main sources of reducible background are:

- non-isolated muons in jets, mostly originated in secondary vertices and produced in B and D mesons decays;
- real muons from light-flavor mesons (pions and kaons) decay;
- charged hadrons "punching through" the calorimeter and reaching the muon system;
- light quark jets misidentified as muons.

The statistics of the simulated events samples is typically not large enough to study and estimate this background: in fact, no events survive applying the signal selection. Therefore, according to the approch used in the Run-2 analysis (2016), so-called *the fake-rate method*, the same data-driven technique has been used for MC samples to estimate the reducible backgrounds due to the huge cross-section of the Z +jets processes.
This method comprises two steps:

[2]Please, remember that hereafter all the signal samples and the DY, $t\bar{t}$ and ZZ background samples have been used to perform these studies.

Step 1 A background control phase space region is defined to measure the probability of a fake muon candidate, referred to as *fakeable object*, to be misidentified like a muon. To perform the so-called *FR measurements* events are restricted to have only three objects (Z_1 and one additional fakeable object), checking if the Z_1 mass is comparable to the nominal Z boson mass (within a mass window ± 10 GeV). Avoiding to require four objects any possible signal-like contribution from the control phase space region is surely excluded and the FR is measured only in the Z +jets and $t\bar{t}$ control region.
The two muons which come from the Z_1 are required to have a transverse momentum greater than 20 GeV and 10 GeV respectively, while the third muon should have $p_T > 5$ GeV in the region $|\eta| < 2.4$ or $p > 5$ GeV in the region $2.4 < |\eta| < 2.8$. The FR measurement is performed on this third fakeable object.
If the fakeable object passes the optimized track-based isolation requirement, it is automatically used as a prompt muon. Let us consider that the total number of jets (N^{tot}_{jets}) is given by the sum of jets which pass (N^{P}_{jets}) or fail (N^{F}_{jets}) the isolation requirement:

$$N^{tot}_{jets} = N^{F}_{jets} + N^{P}_{jets}; \tag{4.2}$$

then, the *fake rate* (FR) is defined as

$$\mathrm{FR}_{jet\to\mu} = \frac{N^{P}_{jets}}{N^{tot}_{jets}}. \tag{4.3}$$

Step 2 The measured probability is applied to events containing a Z_1 boson and two additional fakeable objects in order to evaluate the contribution of fake muons in the signal region, which indicates all events with four muons passing identification and isolation requirements.
The number of background events in the signal region, N^{P}_{jets}, is estimated as:

$$N^{P}_{jets} = N^{F}_{jets}\frac{\mathrm{FR}}{1-\mathrm{FR}}. \tag{4.4}$$

In the background control region two categories depending on whether one or both fail the isolation requirement can be distinguished:

- 3P1F background events, referred to as N_{3P1F}, include three prompt muons and one fake muon, where one prompt muon is a fakeable object which definitely passes the isolation requirement. An event contaminates the signal region if the last object also passes the isolation cut.

- 2P2F background events, referred to as N_{2P2F}, have two prompt muons and two fake muons; they contaminates the signal phase space only if both the fakeable objects pass the isolation requirement.

Loose ID		
	PU = 0	PU = 200
FR ($\|\eta\| < 1.2$)	0.226 ± 0.038	0.297 ± 0.068
FR ($1.2 < \|\eta\| < 2.4$)	0.193 ± 0.038	0.419 ± 0.068
FR ($2.4 < \|\eta\| < 2.8$)	0.144 ± 0.076	0.352 ± 0.15
Z + jets + $t\bar{t}$ estimation	< 2900	< 3000

Table 4.2: Average FR for three different $|\eta|$ ranges with associated statistical uncertainties and estimated Z + jets and $t\bar{t}$ backgrounds, for PU 0 and PU 200.

The final estimate of the expected reducible background is therefore given by

$$N_B^{reducible} = \sum_i \frac{f_i}{1-f_i}(N_{3P1F} - N_B^{3P1F}) + \sum_{i \neq j} \frac{f_i}{1-f_i}\frac{f_j}{1-f_j} N_{2P2F}, \qquad (4.5)$$

where i refers to one fakeable object and j to the other one and the notation $f_{i,j}$ indicates the measured FR corresponding to the ith or jth muon.
The N_B^{3P1F} is the contamination 2P2F events into the phase space of 3P1F category: for this reason, it is subtracted from the events in 3P1F category before applying the FR.

The measured FR as a function of p_T in the central region or p in the forward region are shown in Figures 4.6 and 4.7 for a PU 0 and PU 200 scenario respectively. Table 4.2 shows the average FR related to the three $|\eta|$ ranges considered: the barrel region ($|\eta| < 1.2$), the endcap region ($1.2 < |\eta| < 2.4$) and the very forward region provided by the extension in pseudorapidity coverage of the muon detector ($2.4 < |\eta| < 2.8$) proposed.
The associated statistical uncertainties are very large due to the limited statistics, but the FR is found compatible to the ones obtained with the 2016 data [78].
The final Z + jets plus $t\bar{t}$ (referred to as $Z + X$ hereafter) estimation is also given in Table 4.2. It is also compatible with results of the 2016 data analysis [78]. Because of limited statistics, almost 100% statistical uncertainties are associated to the final estimation, so only upper limits on the background estimates have been quoted. According to Run-2 analysis, a systematic uncertainty of 40% is assigned (which is an optimistic choice).

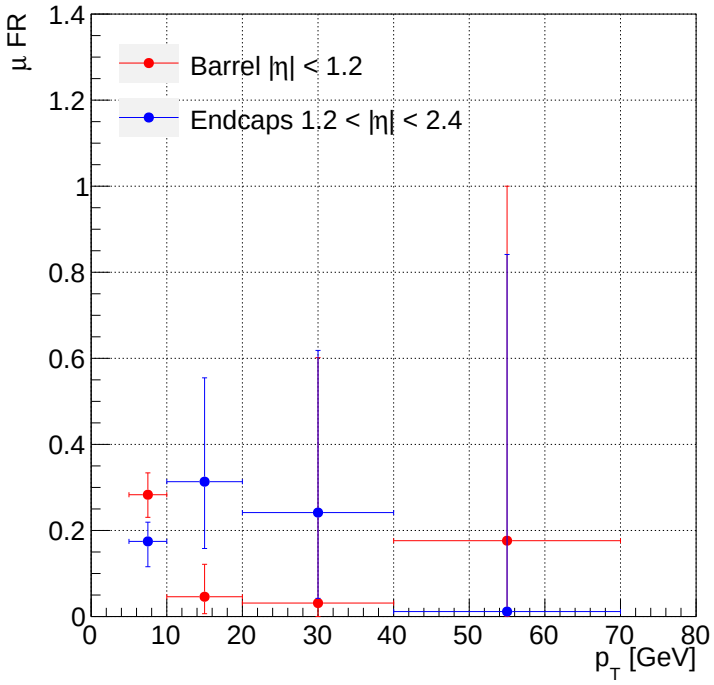

(a)

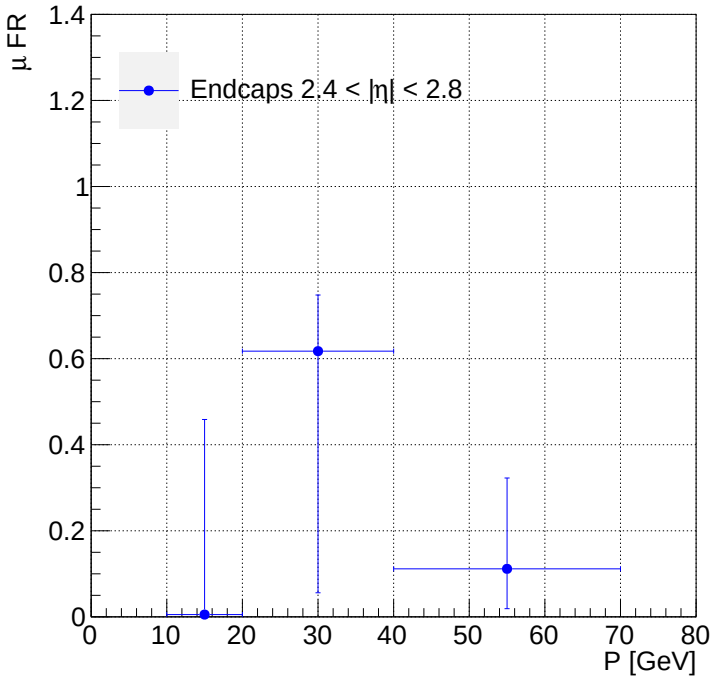

(b)

Figure 4.6: Muon FR as a function of p_T (a) and p (b) for a PU 0 scenario in the region ($|\eta| < 2.4$) and ($2.4 < |\eta| < 2.8$) respectively.

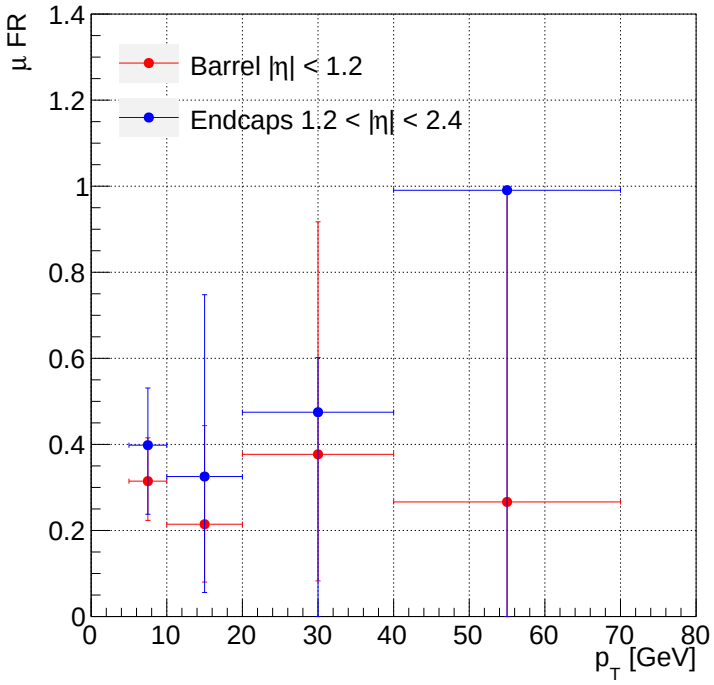

(a)

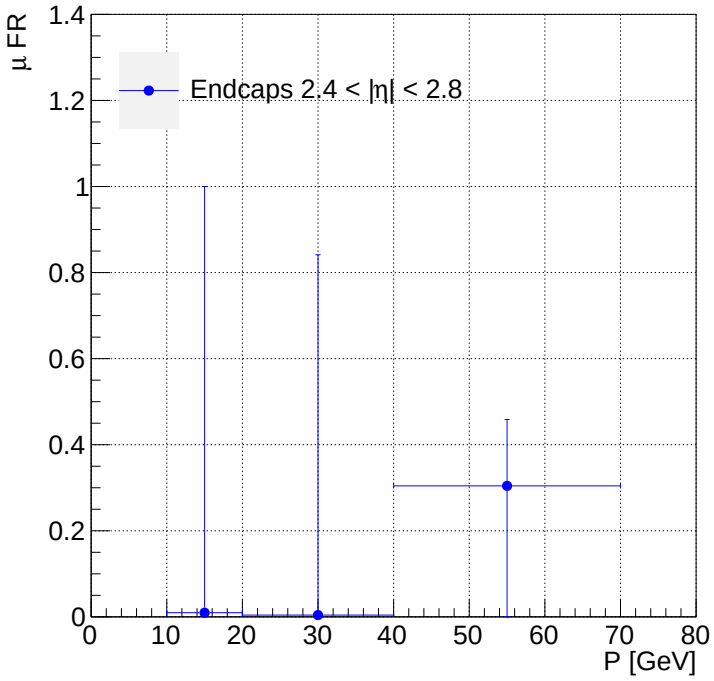

(b)

Figure 4.7: Muon FR as a function of p_T (a) and p (b) for a PU 200 scenario in the region ($|\eta| < 2.4$) and ($2.4 < |\eta| < 2.8$) respectively.

4.4 Results

A comparison between the 2017 geometry ($|\eta| < 2.4$) and the upgraded CMS detector configuration ($2.4 < |\eta| < 2.8$) is presented in Figure 4.10, where the percentage of events passing the full analysis chain with the Loose Muon identification and track-based isolation for two different pile-up scenarios is shown. The number of events is normalized to the number of events containing at least four generated muons within the geometrical acceptance. Let us note an increase of the signal acceptance of about 17% with the upgraded configuration.

Figure 4.8 shows the invariant mass distribution of the four leptons selected at the end of the analysis in the PU 200 configuration. The signal is shown together with the irreducible $ZZ \to 4\mu$ background and the reducible $Z + X$ background.

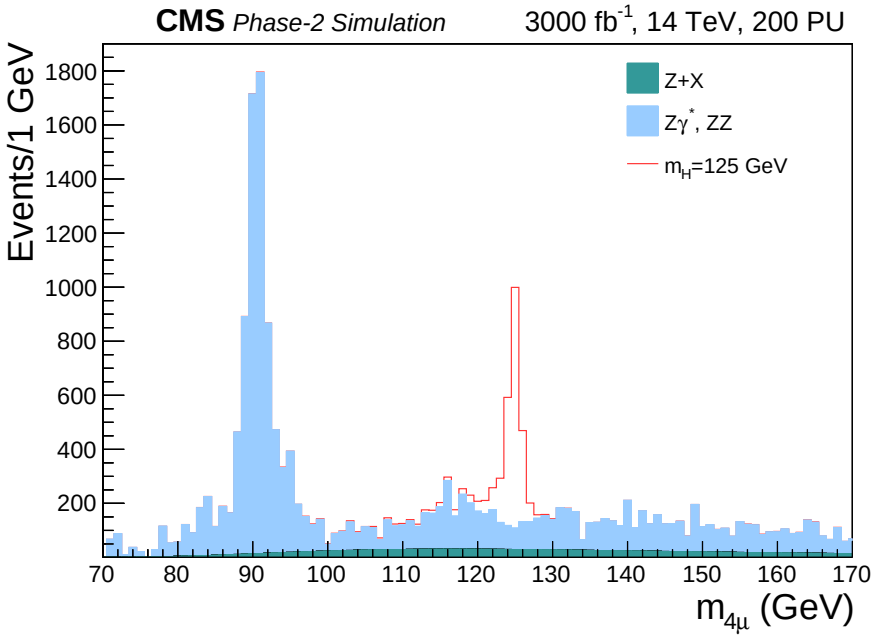

Figure 4.8: The four-lepton invariant mass distribution for selected events in the signal and background samples for a PU 200 scenario corresponding to an integrated luminosity of 3000 fb^{-1}.

Table 4.3 gives the number of $H \to ZZ^* \to 4\mu$ and estimated background event yields at the end of the selection, in two different $|\eta|$ ranges (with and without the acceptance extension), considering the full mass range $100 < m_{4\mu} < 1000$ GeV for PU 0 and PU 200 and also a mass window of $118 < m_{4\mu} < 130$ GeV for PU 200 in order to get the better significance, given by the ratio

$$\frac{S}{\sqrt{B}}. \tag{4.6}$$

The total number is normalized to an integrated luminosity of 3000 fb^{-1}, which

corresponds to the scenario expected at the end of the HL-LHC. Since the $Z + X$ estimates are computed using MC samples with very limited statistics, only conservative upper bounds are quoted.
The Higgs differential cross-section measurement as a function of the Higgs boson p_T will strongly benefit from the large statistics that will be collected with Phase-2 upgraded CMS detector, as we can observe comparing the Run-2 data (2016) results presented in Table 4.4 and results of this analysis in Table 4.3. For this measurement, the theoretical uncertainties are not strictly relevant and the high p_T region (> 200 GeV) will still be dominated by the statistical uncertainty at 3000 fb^{-1}.

Figure 4.9 shows the transverse momentum of the four lepton system for the signal and background samples in the mass window $118 < m_{4\mu} < 130$ GeV for the PU 200 configuration expected during the HL-LHC and with $|\eta| < 2.8$. Results are given for an integrated luminosity of 3000 fb^{-1}.

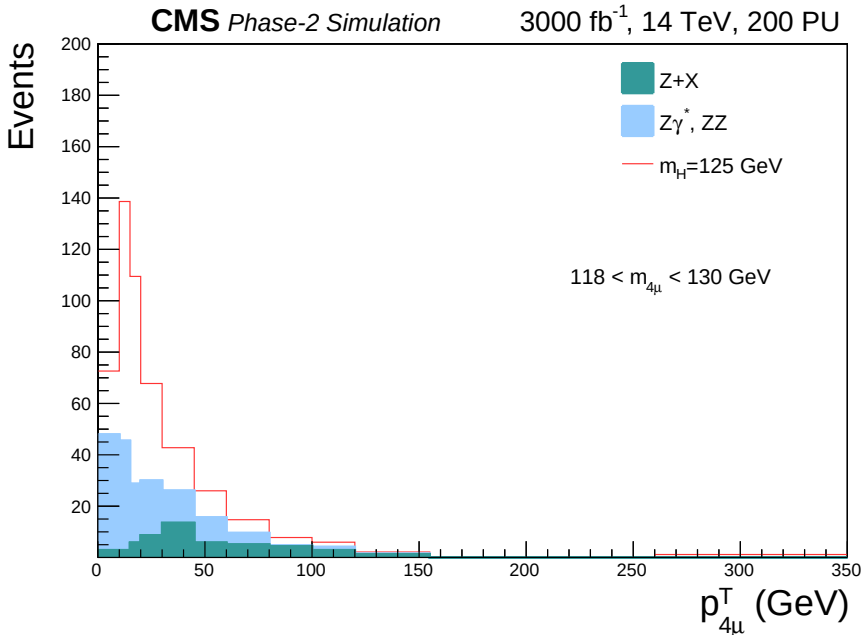

Figure 4.9: Four muon transverse momentum distribution for the signal, irreducible (ZZ and $Z\gamma^*$) and reducible $Z + X$ background in the mass region $118 < m_{4\mu} < 130$ GeV for a PU 200 scenario corresponding to an integrated luminosity of 3000 fb^{-1}.

This demonstrates that it will be possible to probe the processes in which Higgs boson is produced with high p_T (greater than 100 GeV), if a good detector performance at the HL-LHC will be mantained. This fact is particularly interesting because the yield and distribution of events in that range is sensitive to BSM physics that may be contributing to the Higgs boson production (e.g., via additional particles in the loop-induced $gg \to H$ process).

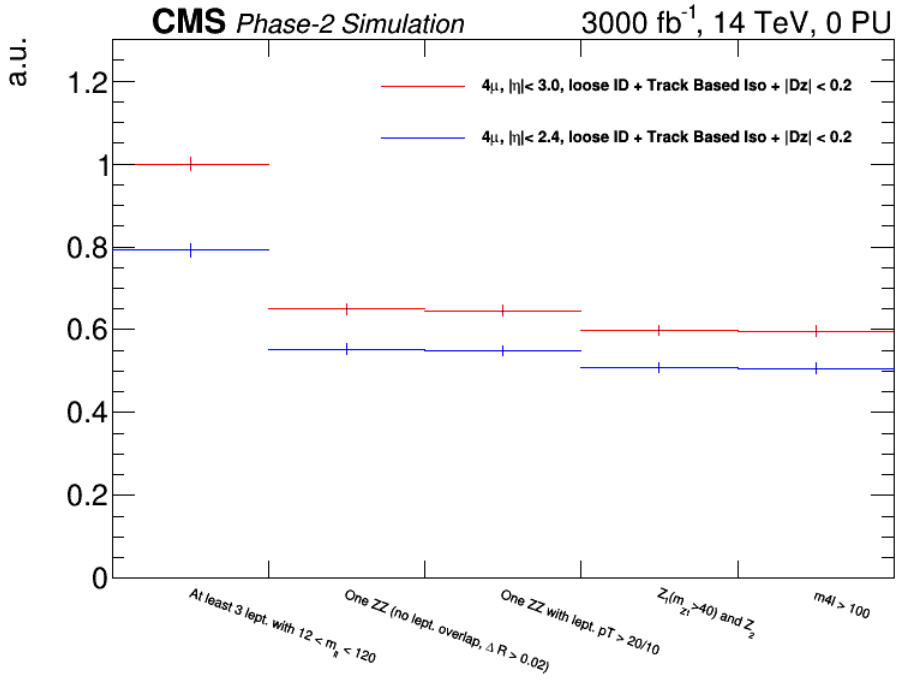

(a)

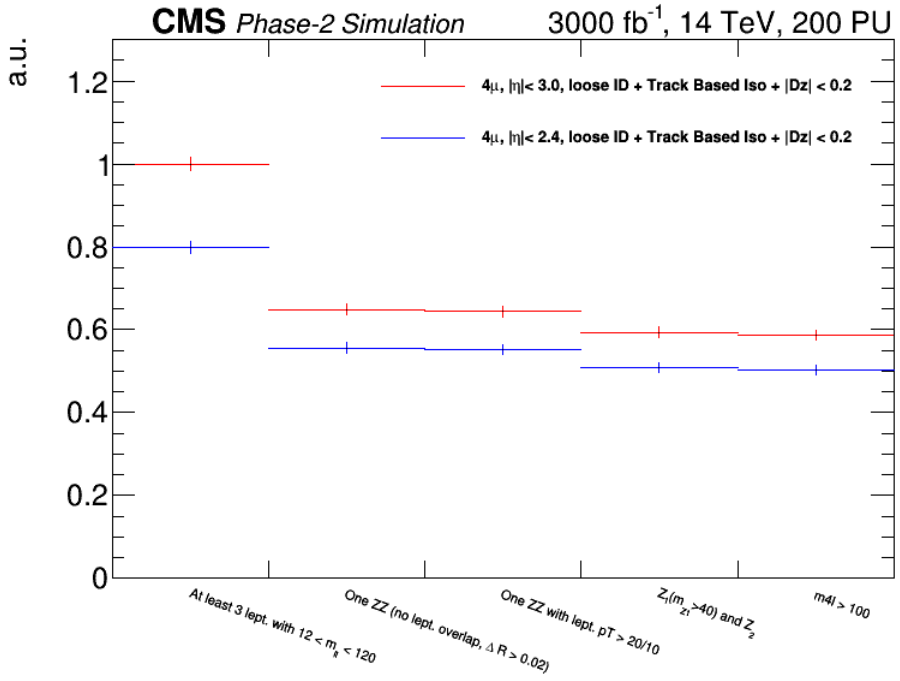

(b)

Figure 4.10: Cut-flow tables which show the percentage of events passing each step of the analysis applied to the $H \rightarrow ZZ^* \rightarrow 4\mu$ signal sample for the two geometrical configurations of the detector, for PU 0 (a) and PU 200 (b).

3000 fb^{-1}@ 14 TeV				
	PU = 0		PU = 200	
Channel - 4μ	$\|\eta\| < 2.8$	$\|\eta\| < 2.4$	$\|\eta\| < 2.8$	$\|\eta\| < 2.4$
ggH, $m_H = 125$ GeV	2142 $\pm$ 31	1822 $\pm$ 29	2128 $\pm$ 32	1826 $\pm$ 30
ZZ background	32273 $\pm$ 1049	25158 $\pm$ 926	28292 $\pm$ 513	22477 $\pm$ 457
$Z + X$ backgroud	< 2900	< 2900	< 3000	< 3000

3000 fb^{-1}@ 14 TeV, PU = 200		
Channel - 4μ, $118 < m_{4\mu} < 130$ GeV	$\|\eta\| < 2.8$	$\|\eta\| < 2.4$
ggH, $m_H = 125$ GeV	2164 $\pm$ 23	1858 $\pm$ 21
ZZ background	1465 $\pm$ 142	1177 $\pm$ 125
$Z + X$ background	< 800	< 800
$S/\sqrt{ZZ}$	~57	~54
$S/\sqrt{Z+X}$	~77	~66

Table 4.3: Number of signal and estimated background events from MC simulations, after the final selection, in the full measurement range (for PU 0 and PU 200) $100 < m_{4\mu} < 1000$ GeV and in the reduced mass range (for PU 200) $118 < m_{4\mu} < 130$ GeV, for $|\eta| < 2.4$ and $2.4 < |\eta| < 2.8$.

35.9 fb^{-1}@ 13 TeV, Run-2 data (2016)	
Channel - 4μ	$\|\eta\| < 2.4$
ggH, $m_H = 125$ GeV	19.0 $\pm$ 0.1
ZZ background	8.5 $\pm$ 0.2
$S/\sqrt{B}$	6.5

Table 4.4: Number of signal and estimated background events from Run-2 data (2016), related to the actual geometrical configuration ($|\eta| < 2.4$).

Conclusions

The aim of this thesis is to investigate the $H \rightarrow ZZ^* \rightarrow 4\mu$ analysis in the upgrade scenario to verify the sensitivity of this channel and the potential benefits from the extension of the muon detector coverage up to 2.8 with the addition of the ME0 subdetector.
Starting from a study of the latest tuning of Loose Muon ID and isolation to obtain the optimal selection criteria and implement them in the analysis, a comparison between the two detector configurations (with and without the acceptance extension afforded by the ME0 subdetector) with two different pile-up scenarios (with an average pile-up of 0 and 200) has been performed.

Two important conclusions can be derived from these results.
First of all, a significant improvement in the selection efficiency is observed: the extended muon system coverage up to a pseudorapidity of 2.8 of the Phase-2 muon detector increases the signal acceptance by 17%.
Secondly, the upgraded detector maintains the performance of the current detector and the signal acceptance remains nearly immune at more challenging pile-up conditions expected at the HL-LHC, thanks to a robust muon reconstruction.
Thus, assuming an integrated luminosity of 3000 fb^{-1}, the Higgs boson properties will be measured with ever increasing precision. These results have been recently included in the muon detector Technical Design Report (TDR) [79].

The following urgent step concerns the inclusion of final states with electrons: in fact the $H \rightarrow ZZ^* \rightarrow 4l$ ($l = e, \mu$) will represent a benchmark for the proposed HGCAL upgrade.
Moreover, finilizing the Phase-2 detector design and the software algorithms needed by the analysis is important to ensure that the backgrounds will be maintained under control in the high contamination environment which will characterize the HL-LHC. In fact, the large statistics collected in almost ten years of HL-LHC will allow to perform the Higgs precision measurements exploring various production modes (gg fusion, VBF, $ZH, WH, t\bar{t}$) and indeed to search for new physics.

Bibliography

[1] D. Griffiths, *Introduction to elementary particles*, WILEY-VCH Verlag GmbH & Co. KGaA, 2004.

[2] S. Braibant, G. Giacomelli, M. Spurio, *Particles and fundamental interactions: an introduction to particle physics*, Springer, 2012.

[3] S. Weinberg, *The Making of the Standard Model*, Eur.Phys.J.C34:5-13, 2004, arXiv:hep-ph/0401010v1.

[4] I. J. Aitchinson, *An informal introduction to gauge field theories*, Cambridge University Press, 1982.

[5] A. Zee, *Quantum Field Theory in a Nutshell*, Cambridge University Press, 2010.

[6] C. Quigg, *Gauge Theories of the Strong, Weak, and Electromagnetic Interactions*, The Benjamin-Cummings Publishing Company, Inc., 1983.

[7] Taylor, J. C., *Gauge Theories of Weak Interactions*, Cambridge University Press, 1976.

[8] S. Coleman, *Aspect of symmetry – Selected Erice lectures*, Cambridge University Press, 1985.

[9] G. Guralnik, C. R. Hagen, T. W. B. Kibble, *Global Conservation Laws and Massless Particles*, Phys. Rev. Lett. 13 (20) 585–587, doi:10.1103/PhysRevLett.13.585, 1964.

[10] P. W. Higgs, *Broken Symmetries and the Masses of Gauge Bosons*, Phys. Rev. Lett. 13 (16) 508–509, doi: 10.1103/PhysRevLett.13.508, 1964.

[11] F. Englert and R. Brout, *Broken Symmetry and the Mass of Gauge Vector Mesons*, Phys. Rev. Lett. 13 (9) 321-23, doi:10.1103/PhysRevLett.13.321, 1964.

[12] G. S. Guralnik, C. R. Hagen and T. W. B. Kibble, *Global Conservation Laws and Massless Particles*, Physical Review Letters. 13 (20), 585–587, doi:10.1103/PhysRevLett.13.585.

[13] G. S. Guralnik, *The History of the Guralnik, Hagen and Kibble development of the Theory of Spontaneous Symmetry Breaking and Gauge Particles*, International Journal of Modern Physics A. 24 (14), 2601-2627, DOI:10.1142/S0217751X09045431.

[14] R. Brout, F. Englert, *Spontaneous Symmetry Breaking in Gauge Theories: A Historical Survey*, arXiv:hep-th/9802142, 1998.

[15] A. Datta, B. Mukhopadhyaya, A. Raychaudhuri, *Physics at the Large Hadron Collider*, Springer, 2009.

[16] LEP Higgs working group, *Higgs boson searches at LEP*, J. Phys., Conf. Ser. 110 042030, 2008.

[17] The Tevatron http://www.fnal.gov/pub/tevatron.

[18] A. Djouadi et al., *Electroweak symmetry breaking at the LHC*, arXiv:0901.2030 [hep-ph], 2009.

[19] C. Patrignani et al. (Particle Data Group), *Review of particle physics*, Chin. Phys. C, 40, 100001, 2016.

[20] The ATLAS Collaboration, *Observation of a New Particle in the Search for the Standard Model Higgs Boson with the ATLAS Detector at the LHC*, CERNPH-EP-2012-218, 2012.

[21] The CMS Collaboration, *Observation of a new boson at a mass of 125 GeV with the CMS experiment at the LHC*, CERN-PH-EP/2012-220, 2012.

[22] L. D. Landau, *On the angular momentum of a two-photon system*, Dokl. Akad. Nauk 60 (1948) 207.

[23] C. N. Yang, *Selection Rules for the Dematerialization of a Particle into Two Photons*, Phys. Rev. 77 (1950) 242, DOI:10.1103/PhysRev.77.242.

[24] *CERN* http://home.web.cern.ch.

[25] LHC Design Report, CERN 2004-003, 2004.

[26] Communication Group, *CERN: FAQ - LHC: the guide*, CERNBrochure-2008-001-Eng, 2008.

[27] The ATLAS Collaboration, *ATLAS Technical Proposal for a General-Purpose pp Experiment at the Large Hadron Collider at CERN*, CERN/LHCC 94-43, 1994.

[28] The CMS Collaboration, *CMS, the Compact Muon Solenoid : technical proposal*, CERN/LHCC 94-38, 1994.

[29] The ALICE Collaboration, *ALICE: Technical proposal for a large ion collider experiment at the CERN LHC*, CERN/LHCC 95-71, 1995.

[30] The LHCb Collaboration, *LHCb : Technical Proposal*, CERN/LHCC 98-004, 1998.

[31] The LHC TDR Editorial Board, *LHC Computing Grid - Technical Design Report*, CERN-LHCC-2005-024, 2005.

[32] CMS Collaboration, *CMS Compact Muon Solenoid – Letter of intent*, CERN/LHCC 92-3, LHCC/11, 1992.

[33] https://home.cern/about/experiments/cms

[34] The CMS Collaboration, *CMS Physics Technical Design Report, Volume I: Detector performance and software*, CERN/LHCC 2006-001, 2006.

[35] The CMS Collaboration, *CMS Physics Technical Design Report, Volume II: Physics Performance*, Nuclear and Particle Physics, Volume 34, Number 6, 2007.

[36] The CMS Collaboration, *The Magnet Project Technical Design Report*, CERN/LHCC 97-10, 1997.

[37] The CMS Collaboration, *The CMS tracker system project: Technical Design Report*, CERN/LHCC 98-6, 1998.

[38] The CMS Tracker Collaboration, Presentation by M. Krammer, *The Silicon Inner Tracker of CMS*, www.hephy.at/fileadmin/user_upload/.../UAE-CERN.pdf.

[39] The CMS Collaboration, *The Electromagnetic Calorimeter: Technical Design Report*, CERN/LHCC 97-33, 1997.

[40] A. Ghezzi, on behalf of the CMS Collaboration, *The CMS electromagnetic calorimeter calibration during Run I: progress achieved and expectations for Run II*, Journal of Physics: Conference Series 587, DOI:10.1088/1742-6596/587/1/012002, 2015.

[41] The CMS Collaboration, *HCAL Technical Design Report*, CERN/LHCC 97-31, 1997.

[42] P. Pooth, *The CMS Silicon Strip Tracker - Concept, Production and Commissioning*, Springer-Verlag New York Incorporated, 2010.

[43] The CMS Collaboration, *Muon Technical Design Report*, CERN/LHC 97-32, 1997.

[44] The CMS Collaboration, *The performance of the CMS muon detector in proton–proton collisions at* $\sqrt{s} = 7$ *TeV at the LHC*, CERN-PH-EP/2013-037, 2014.

[45] Laboratori Nazionali di Frascati, *THE CMS RPC GAS GAIN MONITORING SYSTEM: an Overview and Preliminary Results*, arXiv:0812.1108v1, 2008.

[46] The CMS Collaboration, *The TriDAS Project - Technical Design Report, Volume 1: The Trigger Systems*, CERN/LHCC 2000-38, 2000.

[47] The CMS Collaboration, *The CMS trigger system*, CERN-EP/2016-160, 2017.

[48] The CMS Collaboration, *TECHNICAL PROPOSAL FOR THE UPGRADE OF THE CMS DETECTOR THROUGH 2020*, CMS UG–TP–1

[49] K. Klein for the CMS Collaboration, *The Phase-1 Upgrade of the CMS Pixel Detector*, CMS CR-2016/036, 2016.

[50] F. Sauli, *The gas electron multiplier(GEM): Operating principles and applications*, Nuclear Instruments and Methods in Physics Research A-805 (2016) 2–24, 2015.

[51] The CMS Collaboration, *Technical Proposal for the Phase-II Upgrade of the Compact Muon Solenoid*, CERN/LHCC-2015-010 / LHCC-P-008.

[52] B. Baker et al., *Studies of the performances of the $H \to ZZ \to 4l$ analysis with the CMS Phase II detector upgrade*, CMS AN-2013/298, 2013

[53] A. M. Magnan on behalf of the CMS collaboration, *HGCAL: a High-Granularity Calorimeter for the endcaps of CMS at HL-LHC*, JInst 12 C01042, 2017. .

[54] T. Sjöstrand et al., *An introduction to PYTHIA 8.2*, *Computer Physics Communications* **191** (2015) 159, doi:10.1016/j.cpc.2015.01.024.

[55] S. Alioli, P. Nason, C. Oleari, and E. Re, *NLO vector-boson production matched with shower in POWHEG*, *JHEP* **07** (2008) 060, doi:10.1088/1126-6708/2008/07/060, arXiv:0805.4802.

[56] P. Nason, *A new method for combining NLO QCD with shower Monte Carlo algorithms*, *JHEP* **11** (2004) 040, doi:10.1088/1126-6708/2004/11/040, arXiv:hep-ph/0409146.

[57] S. Frixione, P. Nason, and C. Oleari, *Matching NLO QCD computations with parton shower simulations: the POWHEG method*, *JHEP* **11** (2007) 070, doi:10.1088/1126-6708/2007/11/070, arXiv:0709.2092.

[58] G. Luisoni, P. Nason, C. Oleari, and F. Tramontano, *$HW^{\pm}/HZ$ + 0 and 1 jet at NLO with the POWHEG BOX interfaced to GoSam and their merging within MiNLO*, *JHEP* **10** (2013) 1, doi:10.1007/JHEP10(2013)083, arXiv:1306.2542.

[59] https://twiki.cern.ch/twiki/bin/view/LHCPhysics/CERNYellowReportPage

[60] R. Ball et al., *Unbiased global determination of parton distributions and their uncertainties at NNLO and at LO*, *Nucl. Phys. B* **855** (2012), no. 2,153, doi:10.1016/j.nuclphysb.2011.09.024, arXiv:1107.2652.

[61] Y. Gao et al., *Spin determination of single-produced resonances at hadron colliders*, *Phys. Rev. D* **81** (2010) 075022, doi:10.1103/PhysRevD.81.075022, arXiv:1001.3396. [Erratum: doi:10.1103/PhysRevD.81.079905].

[62] S. Bolognesi et al., *On the spin and parity of a single-produced resonance at the LHC*, *Phys. Rev. D* **86** (2012) 095031, doi:10.1103/PhysRevD.86.095031, arXiv:1208.4018.

[63] CTEQ School 2014, *MadGraph5 aMC@NLO*, July 14, 2014.

[64] GEANT4 Collaboration, *Geant4 User's Guide for Application Developers*, Version: geant4 10.3, 2016.

[65] GEANT4 Collaboration, *GEANT4: a simulation toolkit*, *Nucl. Instrum. Meth. A* **506** (2003) 250, doi:10.1016/S0168-9002(03)01368-8.

[66] J. Allison et al., *Geant4 developments and applications*, *IEEE Trans. Nucl. Sci.* **53** (2006) 270, doi:10.1109/TNS2006.869826.

[67] https://twiki.cern.ch/twiki/bin/view/CMSPublic/WorkBookCMSSWFramework

[68] M. Stankevicius, K. Lassila-Perini, S. Malik et al., *Developing CMS software documentation system*, Journal of Physics - Conference Series 396 (2012) 062020.

[69] I. Antcheva, M. Ballintijn, B. Bellenot at al., *ROOT: A C++ framework for petabyte data storage, statistical analysis and visualization*, Comput. Phys. Comm. 180 (2009) 2499.

[70] A. K. Nayak, *Reconstruction of physics objects in the CMS detector*, arXiv:1310.7408, 2013.

[71] CMS Collaboration, *Particle-flow event reconstruction in CMS and performance for jets, taus, and* E_T^{miss}, CMS-PAS-PFT-09-001, 2009.

[72] CMS Collaboration, *Commissioning of the particle-flow event with the first LHC collisions recorded in the CMS detector*, CMS-PAS-PFT-10-001, 2010.

[73] CMS Collaboration, *Commissioning of the Particle-Flow Reconstruction in Minimum-Bias and Jet Events from pp Collisions at 7 TeV*, CMS-PAS-PFT-10-002, 2010.

[74] T. Speer, R. Frühwirth, *A Gaussian-Sum Filter for Vertex Reconstruction*, CERNCMS- NOTE-2005-005, 2005.

[75] CMS Collaboration, *Performance of CMS muon reconstruction in pp collision events* $\sqrt{s} = 7$ *TeV*, J. Instrum. 7 (2012) P10002, arXiv:1206.4071.

[76] M. Cacciari, G. P. Salam, and G. Soyez, *The anti-kt jet clustering algorithm*, JHEP 04 (2008) 063, arXiv:0802.1189.

[77] The CMS Collaboration, *Measurements of properties of the Higgs boson and search for an additional resonance in the four-lepton final state at* $\sqrt{s} = 13$ *TeV*, CMS PAS HIG-16-033, 2016.

[78] The CMS Collaboration, *Measurements of properties of the Higgs boson in the four-lepton final state at* $\sqrt{s} = 13$ *TeV*, CMS PAS HIG-16-041, 2017.

[79] The CMS Collaboration, *The Phase-2 Upgrade of the CMS Muon Detectors - Technical Design Report*, CMS-TDR-17-003, 2017.